E1C

Light cone

Internal Report
DESY F35D–97–01
January 1997

Charm and Charm-Strange Hadron Production in *ep* Collisions at HERA as Probes of Confinement

by

R. J. Teuscher

5

Charm and Charm-Strange Hadron Production in *ep* Collisions at HERA as Probes of Confinement

by

Richard John Teuscher

A thesis submitted in conformity with the requirements
for the degree of Doctor of Philosophy in the
University of Toronto

Department of Physics
University of Toronto

Abstract

This thesis presents an experimental investigation of the dynamics of strange and charmed particle production in *ep* collisions. The first observation, in *ep* collisions, of the inclusive production of the $D_s^{\pm}$, the $D^{\pm}$, the D^0, and the $\Lambda_c^{\pm}$ is presented. These signals are used to measure the asymmetry in the production rate of D^0 and $\overline{D}^0$; this asymmetry is found to be consistent with the prediction from Monte Carlo simulation using LUND string fragmentation. These signals are further used to measure the $D_s^{\pm}$ to D^0 production ratio and also the ratio for $D^{*\pm}$ to D^0 production. The signals were observed in a data sample collected with the ZEUS detector in 1994. The corresponding HERA luminosity is 2.875 ± 0.043 pb^{-1}.

The $D_s^{\pm}$ is reconstructed via the decay channel $D_s^{\pm} \rightarrow \phi\pi^{\pm}$, and the cross section for $ep \rightarrow D_s^{\pm} X$ is measured to be 11.5 ± 4.0 (stat) ± 3.4 (syst) nb. The kinematic range covered is for $p_T(D_s) > 3.0$ GeV, a hadronic centre-of-mass energy $100<W<300$ GeV, and a pseudorapidity $-1.5 < \eta(D_s) < 1.0$. The D^0 is reconstructed via the decay channels $D^0 \rightarrow K^-\pi^+$ and $\overline{D}^0 \rightarrow K^+\pi^-$, and the $D^0/\overline{D}^0$ asymmetry is measured to be -0.3 ± 10 %. The cross section for the process $ep \rightarrow D^0 X$ is measured to be 31.9 ± 5.0 (stat) ± 5.4 (syst) nb. In this case the kinematic range covered is $p_T(D^0) > 3.0$ GeV, $100<W<300$ GeV, and $-1.5 < \eta(D^0) < 1.0$. By comparing the cross-section ratio $\sigma(ep \rightarrow D_s^{\pm} X)/\sigma(ep \rightarrow D^0 X)$ to the ratio calculated from a Monte Carlo model, the strangeness suppression factor γ_s is measured to be 0.48 ± 0.18 (stat) ± 0.12 (syst). This value is consistent with the strangeness suppression measured in e^+e^- experiments. The cross-sections for D^0 and $D^{*\pm}$ production for $Q^2 < 4$ GeV^2 are used to calculate a vector-to-pseudoscalar ratio P_V of 0.86 ± 0.20 (stat) ± 0.11 (syst). This measurement agrees with the prediction from the ratio of possible spin states.

Kurzfassung

Diese Doktorarbeit zeigt eine experimentelle Untersuchung der Dynamik der strange und charm Teilchen-Produktion in *ep* Kollisionen. Die erste Beobachtung, in *ep* Kollisionen, der inklusiven Produktion vom $D_s^{\pm}$, dem $D^{\pm}$, dem D^0, und dem $\Lambda_c^{\pm}$ wird gezeigt. Diese Signale werden benutzt um die Asymmetrie in der Produktionsrate von D^0 und $\overline{D}^0$ zu measen; diese Asymmetrie stimmt mit der Vorhersage von der Monte Carlo Simulation der LUND String- Fragmentation- Anwendung über ein. Weiter werden diese Signale für die Messung des $D_s^{\pm}$ zum D^0 Produktionsverhältnis und ebenfalls für die Messung des Verhältnisses für $D^{*\pm}$- zur D^0- Produktion benutzt. Die Signale sind in einer Datennahme mit dem ZEUS Detektor im Jahre 1994 gesammelt worden. Die übereinstimmende HERA Luminosität ist 2.875 ± 0.043 pb^{-1}.

Das $D_s^{\pm}$ ist im Zerfallskanal $D_s^{\pm} \rightarrow \phi\pi^{\pm}$ rekonstruiert und der Wirkungsquerschnitt für $ep \rightarrow D_s^{\pm} X$ ist zu 11.5 ± 4.0 (stat) ± 3.4 (syst) nb bestimmt worden. Das kinematische Bereich ist $p_T(D_s) > 3.0$ GeV, eine hadronische Schwerpunktsenergie $100<W<300$ GeV und eine Pseudorapidität $-1.5 < \eta(D_s) < 1.0$. Das D^0 ist in den Zerfallskanälen $D^0 \rightarrow K^-\pi^+$ und $\overline{D}^0 \rightarrow K^+\pi^-$ rekonstruiert, und die $D^0/\overline{D}^0$ Asymmetrie ist zu -0.3 ± 10 % bestimmt worden. Die Wirkungsquerschnitte für $ep \rightarrow D^0 X$ ist zu 31.9 ± 5.0 (stat) ± 5.4 (syst) nb bestimmt. In diesem Fall ist das kinematische Bereich $p_T(D^0) > 3.0$ GeV, $100<W<300$ GeV, und $-1.5 < \eta(D^0) < 1.0$. Durch Vergleich des Wirkungsquerschnitt-Verhältnisses $\sigma(ep \rightarrow D_s^{\pm} X)/\sigma(ep \rightarrow D^0 X)$ zum Verhältnis, von einem Monte Carlo Modell kalkuliert, wurde die Strangeness-Unterdrückungsfaktor γ_s zu 0.48 ± 0.18 (stat) ± 0.12 (syst) bestimmt. Dieser Wert stimmt mit der Strangeness-Unterdrückung die in e^+e^- Experimenten gemessen worden ist, überein. Der Wirkungsquerschnitt für D^0 und $D^{*\pm}$ Produktion für $Q^2 < 4$ GeV^2 werden benutzt um eine Vektor- und Pseudoskalar- Häufigkeit P_V von 0.86 ± 0.20 (stat) ± 0.11 (syst) zu kalkulieren. Diese Messung stimmt mit der Vorhersage von der Häufigkeit des möglichen Spin-Zustandes überein.

Acknowledgments

First, I would like to acknowledge my supervisor, Bob Orr, whom I have known since 1989. I will remember his leadership, encouragement, and our interesting discussions in physics and other fields. I would also like to acknowledge John F. Martin, who led the Canadian group at DESY.

Much of my time since 1989 has been spent with the ZEUS Third Level Trigger group, which provided an excellent training. I would like to thank the members: Bob Orr, David Bailey, Sampa Bhadra, Dinu Bandyopadhyay, Gerd Hartner, Mike Crombie, Frank Chlebana, Frédéric Bénard, Cortney Sampson, Stefan Polenz, Kyung Kwang Joo, David Simmons, and Peter Fagerstroem.

I would like to thank Giuseppe Iacobucci, for his leadership of the ZEUS heavy flavour physics working group, and for his helpful advice for my analysis. Thanks also go to Leonid Gladilin, for his second analysis, and to the Weizmann group for providing me with Monte Carlo. Gerd Hartner and Garry Levman gave helpful advice on HEP throughout my time at Toronto.

Also, "vielen Dank" to the Canadian group who made life at DESY enjoyable: Miloš , Wai, Cortney, Mohsen, Rainer, Laurel, Pat, Marc, Michael, Peter, Mike, Frédéric, Mike, Frank, Burk, Larry, David, Dave, Jit Ning, Jutta, Stefan, and Joo.

I would like to acknowledge the Canadian taxpayer, who supported me through the Natural Sciences and Engineering Research Council and the University of Toronto. Thanks also to Winnie Kam, the HEP secretary, and Marianne Khurana, the department secretary, for slicing through red tape.

My parents and family deserve an award for their encouragement and support.

Ik draag dit proefschrift op aan Martine, met veel dank voor je liefde en aanmoediging.

Contributions to the ZEUS Experiment

In the summer of 1990 I started to work on the ZEUS experiment, as a member of the Third Level Trigger Group. During this summer, I worked on the first translation of the offline ZEUS reconstruction software to the UNIX system. The results of this work concluded that the CPU time required by the software was far in excess of what could be used online. In order to develop further trigger strategies for the TLT, we performed an extensive Monte Carlo study of background events.

In the fall of 1991 I took up residence at DESY. During this time, I worked with the TLT group in desigining and implementing our online software for background rejection, and communicating the results in trigger meetings. I wrote a Monte Carlo simulation of cosmic muons, in preparation for the initial ZEUS cosmic runs in 1991. As well, I developed software to fit a vertex to reconstructed tracks in the CTD.

During the first data taking in 1992, I acted as the "code manager" for the TLT software, and as an "online expert". I also worked on the first ZEUS physics publication, "A Measurement of $\sigma_{TOT}(\gamma p)$ at $\sqrt{s}$ = 210 GeV", published in Physics Letters B 293 (1992) 465.

In 1993, I acted as the coordinator for the TLT physics filters. This included writing physics filter algorithms for the soft photoproduction and DIS physics groups. I also worked on the interface of the offline tracking package to the online system.

I became active in the heavy flavour physics group in 1994, by developing tools for particle identification using the dE/dx information of the CTD. I exploited this to obtain the first inclusive observations of the $D_s^{\pm}$, the $D^{\pm}$, the D^0, and the $\Lambda_c^{\pm}$ in ep collisions. These results were presented at the International Europhysics Conference on HEP in Brussels, August 1995, and at the Canadian Association of Physicists (CAP) conference in Ottawa, June 1996. I also performed the first measurement of strangeness suppression in ep collisions using charmed mesons, and the first measurement of the vector-to-pseudoscalar ratio in ep collisions.

Contents

List of Figures

List of Tables

Chapter 1
Introduction

"There are therefore Agents in Nature able to make the Particles of Bodies stick together by very strong Attractions. And it is the Business of experimental Philosophy to find them out." (Isaac Newton, *Opticks*, 1704)

Nearly three hundred years have passed since Newton's challenge, and we have the *Standard Model*, an excellent, if incomplete, theory of what these particles are and what causes them to stick together. Down to the smallest distance scales we can reach experimentally, about 10^{-18} m, the 'Particles of Bodies' are pointlike objects with half-integral spin ($\frac{\hbar}{2}, \frac{3\hbar}{2}, \ldots$) (*fermions*), while the 'Agents of Nature' are similar objects but with integral spin ($0, \hbar, 2\hbar, \ldots$)[1] (*bosons*). The 'Attractions' are four forces, listed in Table 1-1. The strong interaction is the most powerful of the forces, and is responsible for binding protons and neutrons together. The range of the strong interaction is confined to distances of about 10^{-15} m. The electromagnetic interaction is responsible for binding atoms and molecules, and is the most familiar force on the human scale. The weak nuclear interaction governs radioactive decay and initiates the nuclear fusion process in the sun. Gravity is responsible for the attraction of planetary objects and for large scale structures. The Standard Model includes the first three forces and ignores gravity, due to its negligible strength at the energy scales currently reachable.

The fundamental matter particles may be grouped into three generations or families, based on their electric charges and susceptibility to the strong force, as shown in Figure 1-1. Particles which experience the strong force are referred to as *hadrons* (from *hadros*, Greek for strong or stout), those which do not experience that force as *leptons*. Leptons are believed to be fundamental particles, while hadrons are

1. Henceforth units are used such that $\hbar = c = 1$.

Force	Boson Name	Symbol	Charge	Spin	Mass (GeV)	Coupling
Strong	Gluon	g	0	1	0	~1 large r <1 small r
Electromagnetic	Photon	γ	0	1	0	1/137
Weak	W-boson	$W^{\pm}$	± 1	1	~80	10^{-5}
	Z-boson	Z^0	0	1	~91	
Gravitational	Graviton	G	0	2	0	10^{-38}

Table 1-1 *Fundamental forces.*

bound states of *quarks*, which are fermions having fractional charge. The known bound states are comprised either of three quarks qqq (*baryons*) or a quark and antiquark pair $q\bar{q}$ (*mesons*). Free quarks are not observed in nature, a property referred to as *confinement*.

The analysis in this thesis explores some of the properties of quark confinement, by studying hadron production in high energy electron-proton (ep) collisions. The results of this study test models for hadron structure, as evident from the dynamics of the initial electron-proton collisions, and test models for particle production in the final state. To sift through the background from light quarks (up, down, strange), the massive charm quarks are used as probes.

Chapter 1 of this thesis gives an introduction to Quantum Chromodynamics (QCD), the theory of the strong interaction. QCD-inspired models for hadron production are then presented, along with methods to probe them in ep collisions via charm production. Chapter 2 describes the particle accelerator and detector used in this analysis, while Chapter 3 details the trigger and data acquisition system. General event characteristics and the tools for their reconstruction are given in Chapter 4. In Chapter 5, the observations are presented of the $D_s^{\pm}$ charm-strange meson, the D^0 meson, the $D^{\pm}$ meson, and the $\Lambda_c^{\pm}$ charmed-baryon. In Chapter 6, the charm hadron signals are used to extract hadronization model parameters.

$$\begin{pmatrix} up, charm, top \\ down, strange, bottom \end{pmatrix} = \begin{pmatrix} u^{2/3} \\ d^{-1/3} \end{pmatrix}, \begin{pmatrix} c^{2/3} \\ s^{-1/3} \end{pmatrix}, \begin{pmatrix} t^{2/3} \\ b^{-1/3} \end{pmatrix}$$

$$\begin{pmatrix} electron, muon, tau \\ neutrino \end{pmatrix} = \begin{pmatrix} e^{-1} \\ \nu_e \end{pmatrix}, \begin{pmatrix} \mu^{-1} \\ \nu_\mu \end{pmatrix}, \begin{pmatrix} \tau^{-1} \\ \nu_\tau \end{pmatrix}$$

Figure 1-1 *Fundamental particles.*

1.1 Forces and Gauge Theories

The action of each force is represented by the transmission of a *virtual gauge boson*, shown in Figure 1-2. The word virtual refers to the fact that these particles are *off mass-shell*, meaning that the four-momentum-squared of the particle is not equal to its rest-mass squared ($p^2 \neq m^2$). This is possible for a short time interval according to the Heisenberg Uncertainty Principle.

The carrier of the electromagnetic interaction is the massless, spin-1 photon γ. Because it is massless, the electromagnetic force is infinite in range. The weak interaction, however, is governed by the exchange of the massive bosons $W^{\pm}$ and Z, and has a limited range of about 10^{-18} m. The mediators of the strong interaction are the gluons g. The strong interaction is also in principle infinite in range; however it is constrained to the 1-fm scale by the confinement principle, described in Section 1.2.2. The spin-2 graviton is predicted to be the carrier of the gravitational force, but has yet to be observed.

Each force is formulated in terms of a *gauge theory*. The gauge principle is a recognition that the Lagrangian[1] of a theory remains invariant under a symmetry operation. Consider the Dirac Lagrangian:

$$\mathcal{L} = i\bar{\Psi}\gamma^{\mu}\partial_{\mu}\Psi - m\bar{\Psi}\Psi \qquad (1\text{-}1)$$

which describes a free spin-1/2 particle, with *spinor* wavefunction $\psi = (\Psi_1\Psi_2\Psi_3\Psi_4)$ and mass m. The terms γ^{μ} are the gamma matrices [1], and the

1. A Lagrangian refers to an equation giving the rules governing the particles and their interactions in a given field theory. Alternately, it determines the Feynman diagrams of the theory.

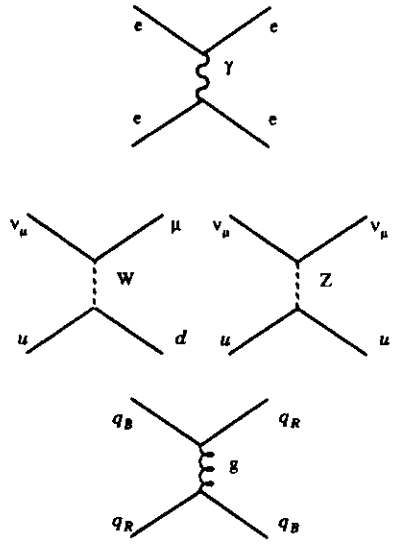

Figure 1-2 *Feynman diagrams for the Standard Model interactions.*

derivative operator in four spacetime dimensions is $\partial_{\mu} \equiv \partial / (\partial x_{\mu})$. This Lagrangian is unchanged by a change in phase, by an amount θ, of the wavefunction:

$$\Psi(x) \rightarrow exp(i\theta)\Psi(x) \qquad (1\text{-}2)$$

which is referred to as a *global gauge transformation*, since the same transformation is applied to all spacetime points x^{μ}. However, if one makes this transformation a function of x^{μ}:

$$\Psi(x) \rightarrow exp(i\theta(x))\Psi(x) \qquad (1\text{-}3)$$

the invariance is lost, as the Lagrangian becomes:

$$\mathcal{L} \rightarrow \mathcal{L} - (\partial_{\mu}\theta)\bar{\Psi}\gamma^{\mu}\Psi \qquad (1\text{-}4)$$

To restore the symmetry it becomes necessary to add a term to the Lagrangian of the form $(\bar{\Psi}\gamma^{\mu}\Psi)A_{\mu}$, which transforms as:

$$A_{\mu} \rightarrow A_{\mu} + \partial_{\mu}\theta \tag{1-5}$$

where a vector field $A(x)$ has been introduced. Classically, this field corresponds to a force, and quantum-mechanically to a photon. Thus, local gauge invariance of the Dirac Lagrangian requires the existence of the photon, the carrier of the electromagnetic force. The phase factor $\theta(x)$ is said to be the generator of the symmetry group U(1), which is the group of unitary transformations in one dimension. The U(1) gauge theory of electromagnetic interactions is referred to as Quantum Electrodynamics (QED).

1.2 Quantum Chromodynamics (QCD)

Strong interactions are described by the local gauge transformations in which the gauge group is SU(3). The SU(3) symmetry is a result of three internal quark degrees of freedom which do not exist amongst the leptons. These degrees of freedom are referred to as *colour charge*, and are arbitrarily given the names red (R), green (G), and blue (B). All observed hadrons consist of colour singlet combinations of (RGB), $(\bar{R}\bar{G}\bar{B})$, and $(R\bar{R}, G\bar{G}, B\bar{B})$. SU(3) transformations are represented by the group of unitary 3×3 matrices λ_i [2]. Local SU(3) gauge invariance requires the introduction of eight massless bosons, the gluons, which carry pairs of colour labels (i.e. $R\bar{G}, B\bar{R}, \ldots$) The Lagrangian density for QCD is [3]:

$$\mathcal{L}_{QCD} = \bar{\Psi}(i\gamma^{\mu}\partial_{\mu} - m)\Psi - \frac{1}{2}g\sum_i(\bar{\Psi}\gamma^{\mu}\lambda_i\Psi)G^i_{\mu} - \frac{1}{4}\sum_i G^i_{\mu\nu}G^{\mu\nu}_i \tag{1-6}$$

A schematic for each of the three terms in the Lagrangian is given in Figure 1-3. The first term represents the propagation of a quark Ψ with mass m. The second term describes the interaction of a quark field with the eight gluon field potentials G^i_{μ} with coupling strength g, which is the probability that a quark or gluon emits a gluon. The third term in the Lagrangian represents the gluon-gluon interactions:

$$G^i_{\mu\nu} \equiv \partial_{\mu}G^i_{\nu} - \partial_{\nu}G^i_{\mu} - g\sum_{j,k} f_{ijk}G^j_{\mu}G^k_{\nu} \tag{1-7}$$

where f_{ijk} are structure constants. A significant difference between QCD and QED is that the gluons, unlike the photon, themselves carry colour charge, and hence can couple to each other as well as to quarks. This is reflected in the third term in Equation (1-7).

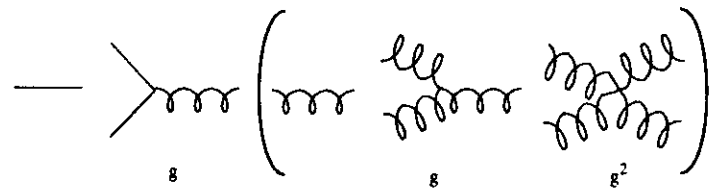

Figure 1-3 *Feynman diagrams corresponding to the QCD Lagrangian density.*

1.2.1 Renormalization

A difficulty in applying quantum field theories such as QCD is that they predict the values of some amplitudes to be infinite [3]. For example, the coupling constant of QCD is defined to be:

$$\alpha_s = \frac{g^2}{4\pi} \tag{1-8}$$

The Feynman diagram for the quark-gluon coupling is shown in Figure 1-3, and involves the gluon propagator term:

$$\frac{-ig_{\mu\nu}}{q^2} \tag{1-9}$$

where q is the gluon four-vector. However, higher order corrections must be added to this coupling, in terms of order g, g^2, and so on. These corrections must be integrated over all momenta, resulting in a logarithmic divergence of the coupling strength. The prescription is to redefine the effective coupling in terms of the scale at which it is measured:

$$\alpha_s(q^2) \equiv \frac{g^2_{eff}}{4\pi} = \alpha_s^0\left\{1 - \frac{\alpha_s^0 b_0}{4\pi}\log\left(\frac{-q^2}{\mu^2}\right) + \left[\frac{\alpha_s^0 b_0}{4\pi}\log\left(\frac{-q^2}{\mu^2}\right)\right]^2 - \ldots\right\} \tag{1-10}$$

where μ is an arbitrary normalization point (the value of q^2 at which $\alpha_s = \alpha_s^0$), and the constant

$$b_0 = \frac{11}{3}N_c - \frac{2}{3}N_f \tag{1-11}$$

where N_c is the number of colours (3) and N_f is the number of quark flavours (6). Equation (1-10) may be expressed as:

$$\alpha_s(q^2) = \frac{\alpha_s^0}{\left\{1 + \frac{\alpha_s^0 b_0}{4\pi}\log\left(\frac{-q^2}{\mu^2}\right)\right\}} = \frac{1}{\frac{b_0}{4\pi}\log\left(\frac{Q^2}{\Lambda^2}\right)} \tag{1-12}$$

where $Q^2 \equiv -q^2$ and:

$$\Lambda^2 = \mu^2 exp\left(\frac{-4\pi}{\alpha_s^0 b_0}\right). \tag{1-13}$$

The term Λ is introduced as a cutoff in Q^2, since $\alpha_s \to \infty$ as $Q^2 \to \Lambda^2$. This is referred to as the 'Landau pole'. When one probes short distances, however, such that $Q^2 \gg \Lambda^2$, the coupling constant tends to zero, a property referred to as *asymptotic freedom*. This property allows for the application of perturbation theory to QCD at high Q^2. Much of the evidence for the validity of QCD is obtained by measurements at such scales.

1.2.2 Bound States in QCD

The problem remains of how to perform calculations in QCD at large distances, the order the size of hadrons, where the coupling constant becomes large and perturbation theory breaks down. To understand the form of the potential binding a $q\bar{q}$ pair, an analogy is made with the Coulomb potential of QED. The short-distance behaviour of QED is dominated by single-photon exchange, and the same is true for QCD, with a gluon replacing the photon. In this approximation, since both the gluon and the photon are massless spin-1 particles, QCD and QED are equivalent, if one replaces the coupling constant α of QED by α_s, and includes additional *colour factors* resulting from the extra gluon degrees of freedom [2]. From the Coulomb potential:

$$V(R) = -\frac{\alpha(R)}{R} \tag{1-14}$$

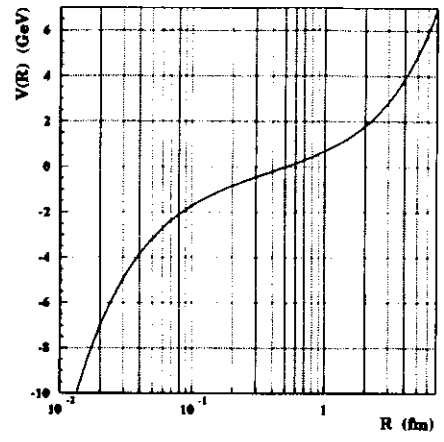

Figure 1-4 *The QCD Potential. This potential is modelled as a sum of a Coulomb-like term for distances (R) smaller than 1 fm and a term linear in R for larger distances.*

the QCD potential for small separations is:

$$V_{QCD}(R)|_{R\to 0} = -\frac{4}{3}\frac{\alpha_s(R)}{R} = -\frac{4}{3}\frac{2\pi}{b_0 R\log\left(\frac{1}{\Lambda R}\right)} \tag{1-15}$$

where 4/3 is the colour factor. At large distances, however, the expression for the coupling constant is no longer valid. Yet one requires a term describing a confining force; the simplest is a linear potential:

$$V_{QCD}(R)|_{R\to\infty} = \kappa R \tag{1-16}$$

where κ is a constant (except at very small distances, in which both α_s and κ will vary). If we combine the two potentials we have the form shown in Figure 1-4.

Thus, unlike QED, the QCD potential at large distances increases without limit, and the force binding a $q\bar{q}$ pair is constant and independent of distance.

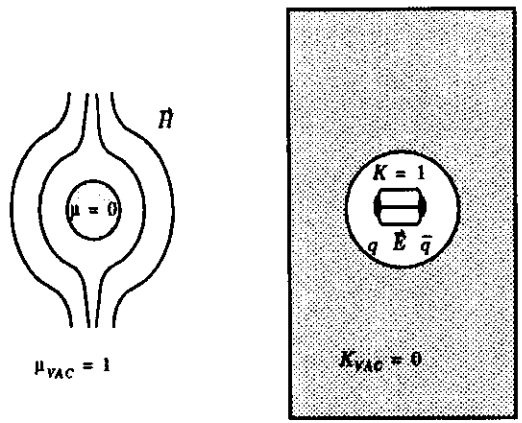

Figure 1-5 *Quark confinement in QCD in analogy with superconductivity in QED. Figure reproduced from [4].*

1.2.3 A Model for Confinement: The QCD Vacuum

While we have a description of the confining potential, we do not have a model for its origin. One explanation for confinement is that the physical vacuum of QCD, the lowest energy state, is opaque to colour [5]. It behaves as a medium which resists the penetration of the colour field, just as a superconductor blocks the penetration of a magnetic field. The energy required to drive a quark through this vacuum is about 1 GeV/fm. However, this is sufficient energy to create more particles and antiparticles, such as light pions. So the quark cannot escape.

The analogy between QCD and QED superconductivity is developed in Figure 1-5. A perfect QED superconductor has zero magnetic permittivity μ and expels an applied magnetic field $\vec{H}$ to the outside vacuum, which has permittivity $\mu_{VAC} = 1$. In the case of QCD, however, the situation is reversed. The chromoelectric field $\vec{E}$, originating from a quark-antiquark pair is excluded from the vacuum, with susceptibility $K_{VAC} = 0$. The field $\vec{E}$ is confined to a region with susceptibility

QED Superconductivity	QCD Vacuum as Perfect Colour Dielectric
$\vec{H}$	$\vec{E}$
$\mu_{inside} = 0$	$K_{vacuum} = 0$
$\mu_{vacuum} = 1$	$K_{inside} = 1$
superconductor inside	superconductor outside

Table 1-2 *QED superconductivity compared to the QCD vacuum.*

$K = 1$, having a volume the size of a hadron. The comparison is summarized in Table 1-2.

Perhaps one way to test the QCD superconductor analogy is to try to "heat up" the vacuum (see Section 1.5.4).

1.3 From Partons to Hadrons or How do you make a proton?

The formation of colour singlet hadrons from coloured *partons*, quarks and gluons, is called *fragmentation* or *hadronization*[1]. In Figure 1-6, a schematic is given for hadronization in *ep* collisions. The transformation from partons to hadrons can be divided into four steps [6]:

The first step is a hard process, meaning that it occurs at a scale $Q^2 \gg \Lambda^2$. In this case the process is $\gamma g \rightarrow q\bar{q}$, in which a photon, emitted from the incoming electron, interacts with a gluon from the proton, to produce a $q\bar{q}$ pair. This interaction is perturbatively calculable, and may also include corrections for initial state QED radiation. In a typical high energy collision, the struck parton is knocked off mass-shell (i.e. $q^2_{parton} \neq m^2_{parton}$).

The second step is a process in which the partons return to mass shell through QCD radiation. This process is modelled in terms of *parton showers*, which are branchings of the form $q \rightarrow qg$, $g \rightarrow gg$, and $g \rightarrow q\bar{q}$. These are a good approximation to the true process, in the limit that the partons are collinear, and are calcu-

1. Some authors define hadronization as the combination of fragmentation and the subsequent decay of unstable particles.

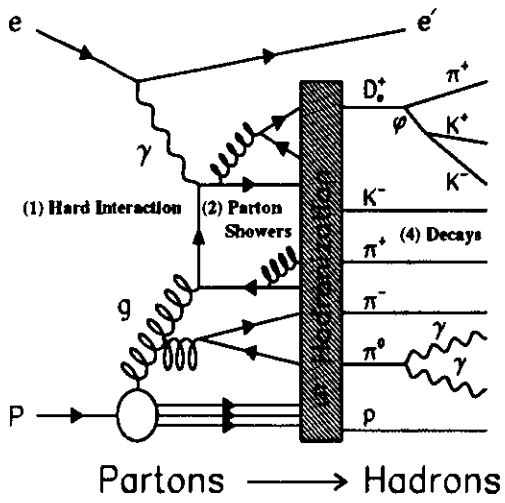

Figure 1-6 *A schematic representation of the four stages of fragmentation in ep collisions.*

lable in perturbative QCD. The perturbative calculations are made to leading-logarithm order (*leading log approximation* or LLA) in terms of an evolution parameter:

$$t = ln(Q^2/\Lambda^2) \tag{1-17}$$

The evolution proceeds towards smaller virtualities until a cutoff scale is reached, typically 1 GeV, at which point perturbation theory breaks down.

The third step is a non-perturbative hadronization phase, in which coloured partons are collected into colourless hadrons. At this stage we resort to phenomenological models, typically based on string or cluster fragmentation (see below).

The final step is a process of secondary decays, since many of the produced hadrons are unstable. This step is also non-perturbative, but can be calculated by using experimental measurements of branching ratios, e.g. $BR(D_s^{\pm} \rightarrow \phi\pi^{\pm})$.

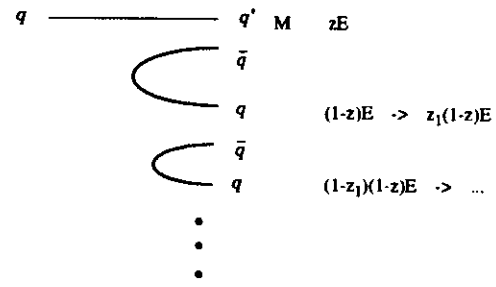

Figure 1-7 *Hadronization in the Independent Jet Model. The fragmenting quark* q *initiates a cascade.*

There are three important models used to describe fragmentation: *independent jet fragmentation*, the *cluster* model, and the *string* model.

1.3.1 Independent Jet Fragmentation

The independent jet (IJ) model was introduced by Field and Feynman in 1978 to explain quark *jet* production in e^+e^- collisions, in which high-energy hadrons are produced in the direction of the primary quarks from the process $e^+e^- \rightarrow q\bar{q}$. Later it was extended to the gluon jets from the reaction $e^+e^- \rightarrow q\bar{q}g$, and also to baryon production.

In the IJ framework, each parton is assumed to fragment independently of the others. As depicted in Figure 1-7, this develops as $q \rightarrow q' + meson\ cascade$. The fragmenting quark q combines with an antiquark $\bar{q}$ from a $q\bar{q}$ pair created from the vacuum to form a meson M with energy fraction:

$$z = \frac{E_M}{E_q} \tag{1-18}$$

The remaining quark has energy fraction $(1-z)$. It is fragmented in the same way, until the remaining energy falls below a cutoff. To describe meson production in this model, one needs [7]:

(i) The probability distribution in z. This is described by a fragmentation function $D(z)$ (see Section 1.5.2).

(ii) The width of the transverse momentum distribution of the hadrons. This arises from the relative transverse momenta of the created $q\bar{q}$ pairs, and is taken to be a Gaussian distribution with $\sigma \sim 300\text{MeV}$.

(iii) The relative probabilities for producing different quark flavours $(u:d:s:c:b)$ when choosing the subsequent quarks. This is set to be (1.0 :1.0 :γ_s:0:0), where γ_s is a free parameter (see Section 1.4).

(iv) The ratio of vector V to pseudoscalar P meson production. This is based on spin counting, and taken to be $V/(V+P) = 3/4$.

Baryon production is added by allowing for the production of *diquarks*, which are intermediate coloured states of two quarks (qq) or two anti-quarks $(\overline{qq})$. Baryon production follows the process $q \rightarrow (\overline{qq}) + baryon$. In addition, gluon jets are treated as a $q\bar{q}$ pair [7][8].

The independent jet model is quite successful in describing broad features of two-jet and three-jet final states in e^+e^- annihilation. One weakness is that the fragmentation of a parton is made dependant on its energy, as opposed to its virtuality. Since the parton is assumed to remain on mass shell, energy and momentum conservation are not obeyed, and one must correct these by rescaling momenta after hadronization. Furthermore, since each jet is treated independently, there are two unused quarks at the end of this process, and so colour and flavour conservation are forced at the end.

1.3.2 The Cluster Model

The cluster model is based on the idea of the *preconfinement* of colour [8]. In this framework, fragmentation is treated as closely as possible as a quark-gluon shower, in analogy with an electromagnetic shower. This shower is terminated when parton virtualities decrease to a cutoff of order 1 GeV. At this point, colourless clusters are formed, a 'preconfinement' of colour. The decay of the clusters is governed entirely by phase space.

An example of charm production and fragmentation in the cluster model is given in Figure 1-8. Following the initial hard interaction $\gamma p \rightarrow c\bar{c}$, the produced partons first branch and then form local clusters, shown in the schematic as dotted lines. Typically each cluster is made to decay into a pair of hadrons. Remarkably, this model can account for fragmentation functions, p_T distributions, and quark flavour production. The cascade model is implemented in the Monte Carlo generator HERWIG [8][9] .

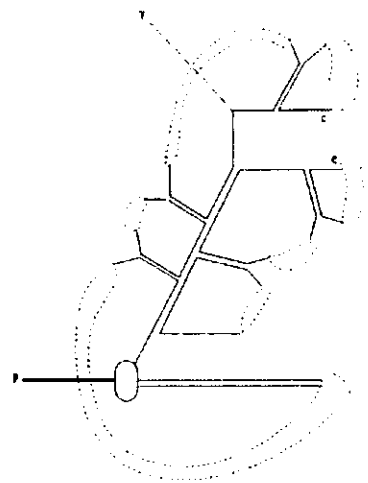

Figure 1-8 *A schematic of the QCD cluster model as implemented in HERWIG. The branchings represent quark-gluon showers, while the "bubbles" represent preconfinement of colour [10].*

1.3.3 The String Model

The string model is inspired by the superconductor analogy to confinement, described in Section 1.2.3. In a QED superconductor, magnetic flux lines are confined to certain regions of a superconductor; this is referred to as the Meissner effect. In analogy to this, the chromoelectric field between a separating $q\bar{q}$ pair is channeled into a flux tube, shown in Figure 1-9. The stored energy of the flux tube is proportional to the quarks' separation distance, as in Equation (1-16). Fragmentation proceeds via successive string breaking. The separating quarks lose energy to the colour field between them, and the string may break apart, forming a new $q\bar{q}'$ pair. This results in two new colour singlets. If the invariant mass of either string is sufficient, the process continues, until only on-shell hadrons remain. The string fragmentation model is implemented in the LUND [11] program.

To generate quark-antiquark pairs along the string, the LUND model makes the analogy with quantum mechanical tunneling through a barrier. Physically, the barrier is the difference between the negative energy level of the $q\bar{q}$ pair before it is

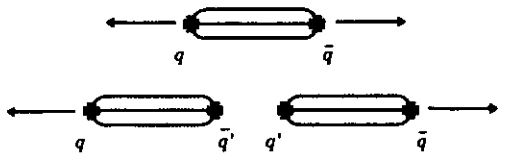

Figure 1-9 *Chromoelectric field lines and string breaking. The string between the separating quarks breaks, resulting in a new $q\bar{q}$ pair.*

created and the positive energy level of the $q\bar{q}$ pair after it is created. The pair forms at the same point in spacetime, so as to obey local flavour conservation, and then the quarks tunnel out of the vacuum. The probability for this is proportional to:

$$exp\left(-\frac{\pi m_\perp^2}{\kappa}\right) = exp\left(-\frac{\pi m_q^2}{\kappa}\right) exp\left(-\frac{\pi p_T^2}{\kappa}\right) \tag{1-19}$$

where m_q is the mass of the created quarks, having transverse momentum p_T, and $m_\perp^2 = m_q^2 + p_T^2$ is the transverse mass of the pair. In this equation κ is the string tension. Because the p_T and mass are factorized in this equation, this model predicts that the transverse momentum spectrum for $q\bar{q}$ pairs is flavour independent. It also accommodates the suppression of heavy quark production through the quark masses (see Section 1.4).

There are several ways to estimate the value of the string tension κ [12]. One is to relate it to the size of a hadron, typically ~1 fm (~ 5 GeV^{-1}) measured from electron-nucleon scattering. A typical hadron mass is of order 1 GeV, so the linear energy density is:

$$\kappa \approx 1 \text{ GeV/fm} \approx \frac{1}{5} \text{ GeV}^2 \tag{1-20}$$

This is equivalent to a stored energy of about 16 tons/m.

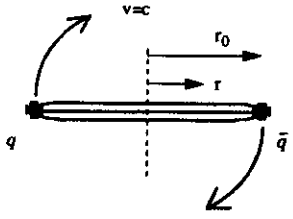

Figure 1-10 *A schematic representation of a meson in the string model. The curved arrows represent the angular rotation of the system [12].*

The string model is further supported by the observation that hadrons lie on *Regge trajectories*. Hadrons are found to obey a simple spin (J) mass (M) relation:

$$J = \alpha_0 + \alpha' M^2 \tag{1-21}$$

with slope $\alpha' \approx 1 GeV^{-2}$, and intercept α_0, which varies for different groups of hadrons. One can relate the Regge slope to the string tension, as follows: one pictures a meson, shown in Figure 1-10, as consisting of two massless quarks connected by a string with energy density κ and length $2r_0$. The angular momentum of the meson will be equal to the angular momentum of the string. If we assume that the ends of the tube rotate at close to the speed of light ($v = c$), then the velocity at a radial distance r from the centre is:.

$$\frac{v}{c} = \frac{r}{r_0} \tag{1-22}$$

The relativistic mass of the system is then:

$$E = Mc^2 = 2\int_0^{r_0} \frac{\kappa dr}{\sqrt{1 - v^2/c^2}} = \kappa r_0 \pi \tag{1-23}$$

and its orbital angular momentum is given by:

$$J = 2\int_0^{r_0} \frac{\kappa r v\, dr}{\sqrt{1 - v^2/c^2}} = \frac{\kappa r_0^2 \pi}{2}. \tag{1-24}$$

Comparing Equations (1-23) and (1-24) we find that:

$$J = \frac{(\kappa r_0 \pi)^2}{2\pi\kappa} = \alpha' E^2 \tag{1-25}$$

where:

$$\alpha' = \frac{1}{2\pi\kappa}. \tag{1-26}$$

The experimental value of $\alpha' = 0.93\ \mathrm{GeV}^{-2}$ gives $\kappa \approx 0.2\ \mathrm{GeV}^2$, in agreement with the rough estimate in Equation (1-20).

To include the possibility of gluon jets, the string model represents them as a kink in the string. The string model yields a good description of the angular distribution of hadrons in 3-jet events in e^+e^- collisions.

The vector-to-pseudoscalar ratio in the string model is 0.75 for mesons containing a c quark or heavier quark, 0.60 for mesons with an s quark and a u or d quark, and 0.50 for mesons comprised of only u and d quarks. The suppression of light vector mesons is explained by tunnelling: the quark spin-spin interaction spreads the wave function of the lighter vector mesons, and reduces the overlap of the $q\bar{q}$ pair.

1.4 Hadronization and Strangeness Suppression

In all of these hadronization models, the relative abundance, compared to up and down quarks, with which strange quarks are produced is referred to as the *strangeness suppression factor*:

$$\gamma_s = \frac{s}{u} \tag{1-27}$$

Here s refers to the number of strange quarks produced and u the number of up quarks produced. If $\gamma_s = 1$ there is no strangeness suppression, while if $\gamma_s = 0$ there

Comparison	γ_s	Experiment
$K^0:\pi^\pm$	$0.35 \pm 0.02 \pm 0.02$	TASSO [14]
$K^0:\pi^\pm$	$0.27 \pm 0.03 \pm 0.05$	JADE [15]
$\phi:K^{*0}$	$0.37 \pm 0.15 \pm 0.08$	TPC [16]
$K^{*}:\rho$	$0.32 \pm 0.09 \pm 0.05$	TPC [16]
$K^0:\pi^0, K^0:\rho$	0.34 ± 0.02	HRS [17]
Average	0.33 ± 0.02	

Table 1-3 *Measurements of strangeness suppression in e^+e^- collisions.*

is a complete suppression of strangeness. Sometimes strangeness suppression is defined in terms of both up and down quarks, as [13]:

$$\lambda_s = \frac{2\langle n_{s\bar{s}}\rangle}{\langle n_{u\bar{u}}\rangle + \langle n_{d\bar{d}}\rangle} \tag{1-28}$$

where $\langle n_{u\bar{u}}\rangle$, $\langle n_{d\bar{d}}\rangle$ and $\langle n_{s\bar{s}}\rangle$ are the mean yields of u, d, and s quarks and antiquarks in an experiment.

The different quark masses input to Equation (1-19) account for the different flavour production ratios. If one uses the *current-quark*[1] masses ($m_u \sim 5$ MeV, $m_d \sim 9$ MeV, $m_s \sim 170$ MeV) one obtains $u : d : s \sim 1.0 : 1.0 : 0.63$. However, if one assumes *constituent-quark*[2] masses ($m_u \sim 340$ MeV, $m_d \sim 360$ MeV, $m_s \sim 540$ MeV) the ratios become:

$$u : d : s \sim 1.0 : 0.8 : 0.06. \tag{1-29}$$

Charm production from fragmentation is negligible in this model, $O(10^{-11})$. Since there is some uncertainty in the assignment of quark masses for hadronization, these models leave the suppression of $s\bar{s}$ production as a free parameter to be determined by experiment. The default LUND parameters are:

$$u : d : s = 1.0 : 1.0 : \gamma_s \tag{1-30}$$

1. The masses observed when a hadron is probed by the electroweak interaction.
2. Based on hadron masses, $m_{constit} = m_{current} + \Lambda$. For example, the proton, made up of uud quarks has $m_p \approx 2m_u + m_d$ [3].

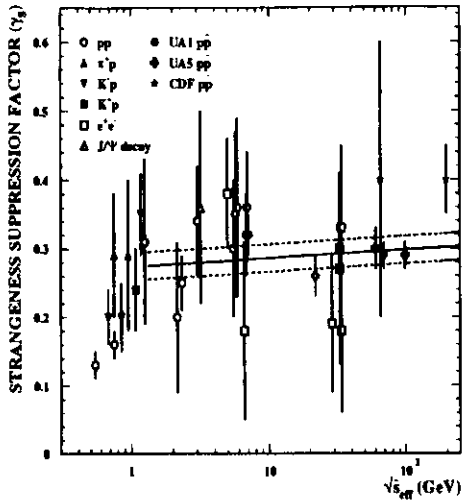

Figure 1-11 *Measurements of strangeness suppression from various particle interactions. The horizontal axis gives the effective centre-of-mass energy for each experiment [25].*

where $\gamma_s = 0.3$. Table 1-3 lists experimental measurements from e^+e^- collisions which have been used to tune the value of γ_s. For example, a measurement of the production ratio $K^0{:}\pi^\pm$ is a function of the ratio $d\bar{s}{:}d\bar{u}$.

Recent measurements of $K^{*\pm}$ and ρ^0 production in e^+e^- collisions [18] find better agreement between data and Monte Carlo using $\gamma_s = 0.23$. A lower value for γ_s has also been reported by several deep inelastic scattering (see Section 4.1) experiments [20][21][22][23], which favour $\gamma_s = 0.2$. These measurements include a ZEUS study [22] of K^0 meson and Λ (uds) baryon production. In the ZEUS measurement, the production rates, transverse momentum, and angular distributions of K^0's and Λ's were determined. A comparison was then made to two Monte Carlo predictions, the first using $\gamma_s = 0.3$ and the second $\gamma_s = 0.2$. Although the data tended to favour $\gamma_s = 0.2$, neither value was ruled out. There is also one recent result indicating a higher value of γ_s in $\nu_\mu Ne$ interactions [24]. A new study of b-mesons in $p\bar{p}$ collisions reports $\gamma_s = 0.34 \pm 0.10$ (stat) ± 0.03 (syst) [19].

As shown in Figure 1-11, there is evidence that γ_s is dependent upon the energy scale at which it is measured [25]. This figure shows a comparison of the measurements of γ_s in pp, $p\bar{p}$, π^-p, K^-p, K^+p, and e^+e^- collisions [26][27][28] according to the effective centre-of mass energy of the hard collision:

$$\hat{s}_{eff} = s\langle x_1\rangle\langle x_2\rangle \tag{1-31}$$

where $\langle x_1\rangle$ and $\langle x_2\rangle$ are the average momentum fractions of the beam valence quark (lepton) and target valence quark (lepton). To convert the centre-of-mass energy squared s to $\hat{s}_{eff}$ for different beams and targets, one uses: $\sqrt{\hat{s}_{eff}(pp)} = \sqrt{\hat{s}_{eff}(p\bar{p})} = 0.11\sqrt{s}$ and $\sqrt{\hat{s}_{eff}(\pi p)} = 0.15\sqrt{s}$.

A fit has been performed by the authors of [25] for $\sqrt{\hat{s}_{eff}} > 1$ GeV, to avoid threshold effects, to the function:

$$\gamma_s = a + b \cdot ln\,(\sqrt{\hat{s}_{eff}}) \tag{1-32}$$

giving $a = 0.274 \pm 0.020$ and $b = 0.0053 \pm 0.0059$. This increase in γ_s may be explained by a rise in gluon radiation with energy. The increased number of gluons subsequently split into $s\bar{s}$ pairs.

As detailed in Section 1.5.3, a measurement of charmed and charm-strange mesons provides a new method for determining γ_s.

1.5 Probing Hadronization with Heavy Quarks

Unlike light quarks (u, d, s), which are copiously produced in the fragmentation process, heavy quarks (c, b, t) originate primarily from initial-state interactions. By studying the production of resonances containing one or more heavy quarks, one can sift through the light-quark 'noise' and study the first collision of partons.

1.5.1 The Hadronization of Charm Quarks

Charm production in ep collisions, illustrated in Figure 1-12, is given by [29]:

$$e + p \rightarrow e' + c + \bar{c} + X \tag{1-33}$$

The electron emits a photon γ, which interacts with a gluon g from the proton. This process is referred to as *boson-gluon fusion*. The fusion produces a quark-antiquark pair, in this case a $c\bar{c}$ pair. The subsequent production of hadrons can be described in terms of the 'Dual Parton Model' [30], in the framework of the string model. Hadronization develops along two strings: a "mesonic" string stretched between the

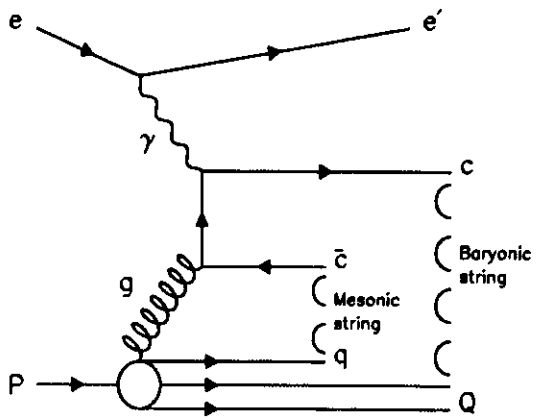

Figure 1-12 *A schematic of charm hadron production in the Dual Parton Model.*

anti-charm quark and a target quark, and a "baryonic" string stretched between the charm quark and the target diquark. Unlike hadronization in e^+e^-, a fragmentation string cannot be stretched between the $c\bar{c}$ pair, as this would lead to a colour non-singlet in the final state, due to the colour of the exchanged gluon. Thus, to form colourless hadrons, the c quark fragments with the diquark (Q), and the $\bar{c}$ quark with the remaining quark (q).

This fragmentation model makes definite predictions. For example, it predicts an observable asymmetry for the production of charm-anti-charm hadrons:

$$A_{c\bar{c}} = \frac{N(c) - N(\bar{c})}{N(c) + N(\bar{c})}. \qquad (1\text{-}34)$$

where $N(c)$ is the number of mesons produced containing a charm quark, and $N(\bar{c})$ is the number containing an anti-charm quark. This asymmetry arises because the c quark can easily find a remnant diquark, leading to a state with a charmed baryon and a $\bar{D}$ meson. The c quark has a higher probability of finding a remnant diquark with which to hadronize than a $\bar{c}$ quark does of finding an anti-diquark. This would lead to $\bar{D}\Lambda_c$ correlations at low energies (near $c\bar{c}$ threshold).

Decay mode	E-687	(LUND E-687)	E-691
$D^+ \to K^-\pi^+\pi^+$	$-3.8 \pm 0.9\%$	$-12.7 \pm 0.9\%$	$-2.0 \pm 1.5\%$
$D^{*+} \to \pi^+ (D^0 \to K^-\pi^+)$	$-6.4 \pm 1.5\%$	$-10.8 \pm 0.9\%$	$-7.0 \pm 3.5\%$
$D^{*+} \to \pi^+ (D^0 \to K^-\pi^+\pi^-\pi^+)$	$-4.0 \pm 1.7\%$	$-11.5 \pm 1.0\%$	$-10.3 \pm 2.8\%$
$D^0 \to K^-\pi^+$ *(no tag)*	$-2.0 \pm 1.5\%$	$-3.6 \pm 0.6\%$	$-3.8 \pm 1.5\%$
$D^0 \to K^-\pi^+\pi^-\pi^+$ *(no tag)*	$-1.9 \pm 1.5\%$	$-6.9 \pm 0.7\%$	
$D_s^+ \to K^+K^-\pi^+$	$2.5 \pm 5.2\%$	$4.8 \pm 0.1\%$	$4.2 \pm 6.8\%$
$\Lambda_c^+ \to pK^-\pi^+$	$3.5 \pm 7.6\%$	$17.4 \pm 1.6\%$	$11.7 \pm 8.4\%$

Table 1-4 *Observed and predicted asymmetries ($A_{c\bar{c}}$) in charm production.*

Previous charmed meson asymmetry measurements from experiment E-687 and E-691 are summarized in Table 1-4, from [31]. In addition, the LUND model prediction for E-687 is given. In most cases, the model predicts a higher asymmetry than observed. One notes that there is a predicted excess of D_s^+ over D_s^-. This is due to phase space limitations in the mesonic string for D_s^- K X production [32]. This overrides the asymmetry described for $\bar{D}/D$.

The analysis in this thesis measures the $D^0/\bar{D}^0$ asymmetry in ep collisions (Section 6.1).

1.5.2 Heavy Quark Fragmentation Functions

Quark antiquark pairs are more likely to combine into a meson when they both propagate at a comparable velocity. When the fragmenting parton is a heavy quark, it needs to lose only a small percentage of its energy to generate light quark pairs having similar velocity. If the heavy quark combines with one of these light quarks, the resulting hadron will carry a sizable fraction of the initial energy.

Fragmentation in this model is described by the Peterson function, $D(z)$. For the transition $Q \to M + q$ from heavy quark Q with momentum P to heavy meson M with momentum zP and quark q with momentum $(1\text{-}z)P$, the energy transfer is:

$$\Delta E = E_Q - E_M - E_q = [m_Q^2 + P^2]^{1/2} - [m_M^2 + z^2P^2]^{1/2} - [m_q^2 + (1-z)^2P^2]^{1/2} \qquad (1\text{-}35)$$

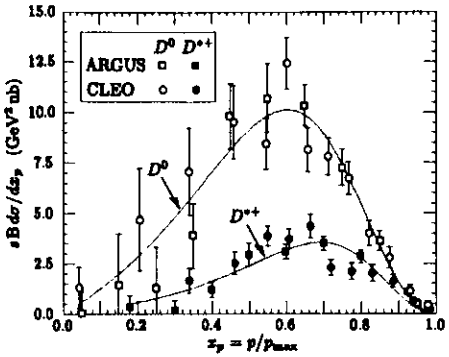

Figure 1-13 *The fragmentation spectrum for charmed mesons. Reproduced from [33].*

Here E_i and m_i refer to the energy and mass of the corresponding quark or meson, and $m_M \approx m_Q$ is assumed. The expression for ΔE simplifies to:

$$\Delta E \propto 1 - z^{-1} - \varepsilon (1-z)^{-1} \tag{1-36}$$

where $\varepsilon \sim (m_q/m_Q)^2$. The transition probability is taken to be: $D(z) \propto z^{-1}\Delta E^{-2}$, where the factor z accounts for longitudinal phase space. This gives:

$$D(z) = \frac{N}{z\left[1 - z^{-1} - \varepsilon(1-z)^{-1}\right]^2} \tag{1-37}$$

with N being a normalization factor. Equation (1-37) is referred to as the Peterson function [34], and has been used to fit a variety of spectra. Results for D^* and D^0 production in $e^+e^- \to q\bar{q}$ are depicted in Figure 1-13 [35][36]. In this plot, the fragmentation variable used is $x_p = p_D/p_{max}$, where p_D is the D-meson momentum. The quantity p_{max} is one-half the centre-of-mass energy of the collision, which is the maximum energy available to each quark or antiquark.

1.5.3 Probing Strangeness Suppression with Charmed Mesons

In this thesis, γ_s is measured with a new method. This method requires the measurement of the production cross-sections of charmed and charm-strange mesons. The interpretation of their cross-sections relies in part on a Monte Carlo model of ep scattering (PYTHIA, see Section 4.2), which uses the string model for hadronization. If one varies the value of the strangeness suppression parameter in the string model from $\gamma_s = 0.0$ to $\gamma_s = 1.0$, and then calculates the resulting production ratio of:

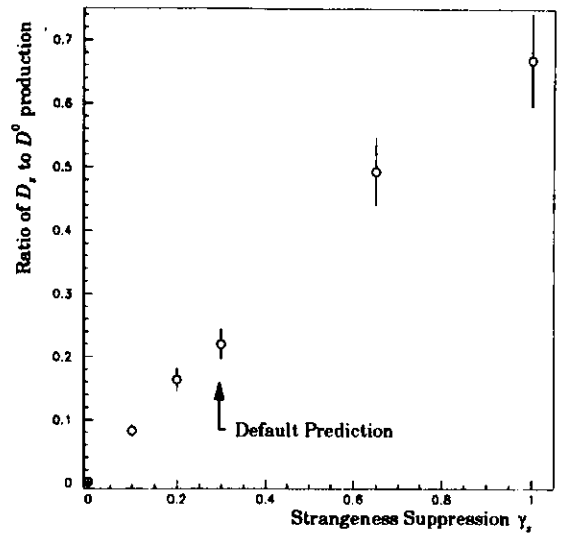

Figure 1-14 *The predicted ratio of D_s to D^0 production as a function of the strangeness suppression factor.*

$$\frac{\sigma(ep \to D_s^+ X)}{\sigma(ep \to D^0 X)} = \frac{c\bar{s}}{c\bar{u}} \tag{1-38}$$

(where both particle and anti-particle are implied), one obtains the values plotted in Figure 1-14. For $\gamma_s = 0$ the model predicts almost zero D_s production compared to the D^0, while for $\gamma_s = 1$ the ratio is 0.669 ± 0.073, where the uncertainty is due to limited statistics. The assumption made in this prediction is that the rate of charm quarks hadronizing into D_s mesons is determined by γ_s. This is not an unreasonable assumption, as the probability that a charm quark picks up a strange quark from

the colour field should be given by γ_s. However, there may still be other dynamics which are not included in the string model [37]. There is also an uncertainty in the branching ratio of the decay mode used to reconstruct the D_s (see Section 5.5).

From the Monte Carlo results using the default value of $\gamma_s = 0.3$, the predicted ratio is:

$$\frac{\sigma(ep \to D_s^{\pm} X)}{\sigma(ep \to D^0 X)} = 0.220 \pm 0.024 \qquad (1\text{-}39)$$

The standard measurement of this ratio was made in the fixed-target photoproduction experiment at NA14/2 [32]. In this experiment, the reaction studied was $\gamma N \to c\bar{c}X$ at $E_\gamma = 100$ GeV. They chose to express the ratio as:

$$\frac{\sigma(\gamma N \to D_s^{\pm} X)}{\sigma(\gamma N \to D^0 X) + \sigma(\gamma N \to D^{\pm} X)} \qquad (1\text{-}40)$$

which represents the quantity $c\bar{s}/(c\bar{u} + c\bar{d})$. They determined it to be $0.17 \pm 0.07 \pm 0.03$.

To make a direct comparison of the NA14/2 measurement to those made in ep collisions, one would need to know the ratio of $D^{\pm}/D^0$ production, which introduces an additional uncertainty. Values for this ratio range from a measurement of $0.33 \pm 0.09 \pm 0.04$ [32] to a prediction of 0.43, based on the counting of polarization states and the measured branching ratios [38].

Alternately, one may derive the ratio from the NA14/2 measurements of $\sigma(D_s^{\pm})/\sigma(D^{\pm})$ and $\sigma(D^{\pm})/\sigma(D^0)$, which results in a ratio of:

$$\frac{\sigma(\gamma N \to D_s^{\pm} X)}{\sigma(\gamma N \to D^0 X)} = 0.22 \pm 0.07 \pm 0.04 \qquad (1\text{-}41)$$

This is in agreement with the model prediction for ep collisions using $\gamma_s = 0.3$.

1.5.4 Deconfinement

If the QCD vacuum is similar to a superconductor, then it is predicted that its confinement properties will change at high temperature/energy densities. From nonperturbative simulations, at a critical temperature of the scale of $kT \sim \Lambda \sim 200$ MeV, the vacuum is found to undergo a phase transition and become transparent to colour. Quarks and gluons are no longer bound inside hadrons but

are free. This state is referred to as a *Quark Gluon Plasma* (QGP), described as a free gas of quarks and gluons. Such a state of matter could have existed at the time of the early universe (when it was about 10^{-5}s old).

In high energy collisions, one of the experimental signatures of quark gluon plasma formation is a change in the production rate of strange quarks. For example, heavy-ion experiments [39] search for an increase in the production rate of hadrons containing strange quarks. These experiments attempt to produce a QGP by generating a region of high temperature and mass density, by colliding heavy ions, such as Pb ions, with energy of order 200 GeV/nucleon. If a QGP is formed, it is expected to possess a high density of u and d quarks from the initial hadrons. As a result of the exclusion principle, the energy level to which their u and d quark states are occupied is raised beyond the mass of the s quark (~120 MeV). This is one of the reasons for a relative increase in the production rate of s quarks. In addition, the large number of energetic gluons in the QGP would generate $s\bar{s}$ pairs through the gluon--gluon fusion process $g + g \to s + \bar{s}$. If the strange quarks survive to form hadrons, this should further enhance the production of strange hadrons.

Charm quarks will also be produced in a QGP [40]. However, it is likely that they will be separated by lighter u, d and s quarks [41]. Therefore, one would predict a suppression in the production of bound states of $c\bar{c}$ pairs, such as the J/ψ. Instead, a higher rate of mesons with a single charm-quark, the D-mesons, would be expected. In particular, the rate of charm-strange mesons, the D_s, might be enhanced.

While it is not expected that ep collisions at HERA will produce a quark-gluon plasma, it is nevertheless an interesting measurement to check the production rate of charm mesons, and particularly the production rate of charm-strange mesons.

Chapter 2

The Accelerator and Detector

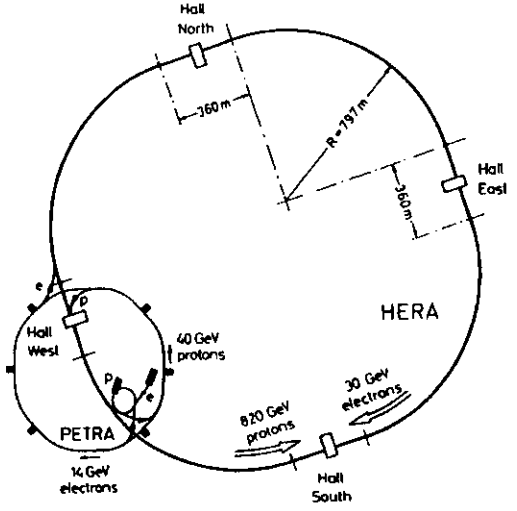

Figure 2-1 *Layout of the HERA accelerator.*

2.1 The HERA Accelerator

The Hadron-Elektron-Ring-Anlage HERA, at the Deutsches Elektronen-Synchrotron DESY, in Hamburg, Germany is the world's first and only electron-proton collider. As shown in Figure 2-1, HERA consists of two separate accelerators, one

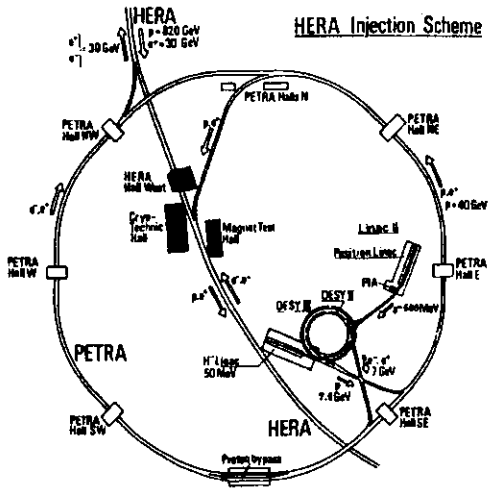

Figure 2-2 *The HERA Injection System.*

storing electrons or positrons, and a second for protons. They are located 10 to 25 m underground in a tunnel 6.3 km in circumference, and are designed to collide 30 GeV electrons with 820 GeV protons at two locations, used by the ZEUS and H1 experiments. In addition, two fixed-target experiments (HERMES and HERA-B) make use of the electron and proton beams. In 1994, HERA collided beams of 820.0 GeV protons with 27.52 GeV positrons, corresponding to a centre-of-mass energy of 300.4 GeV. The centre-of-mass energy for colliding beams of energy E_e and E_p is given by:

$$\sqrt{s} \approx \sqrt{4E_eE_p} \tag{2-1}$$

For comparison, an electron beam scattering off a fixed-target gives:

$$\sqrt{s} \approx \sqrt{2E_em_p} \tag{2-2}$$

where m_p is the nucleon mass. Thus for a fixed-target experiment to reach the HERA centre-of-mass energy would require an incoming lepton beam of energy $\approx$ 450 TeV.

The HERA injection system is shown in Figure 2-2. Electrons are extracted

from a high voltage cathode and brought to 500 MeV with the linear accelerator, LINAC II. In the PIA storage ring the electrons are accumulated into a single bunch and transported to the DESY II synchrotron, where they are accelerated to 7 GeV. Each bunch is transferred to PETRA until it is filled with 70 bunches, and then the bunches are accelerated to 12 GeV. Finally, the bunches are transferred to HERA and brought to 27.52 GeV.

Protons are accelerated as negatively-charged hydrogen ions in a 50 MeV linac. Upon entering DESY III, a proton synchrotron, the protons are stripped of their electrons. The protons are accelerated to 7.5 GeV and injected into PETRA, where they are brought to 40 GeV. Then they are injected into HERA and accelerated to 820 GeV.

HERA is designed to contain 210 bunches of protons and 210 bunches of electrons. In 1994, it operated with 153 *ep* bunches, with typical currents of 20-33 mA (positrons) and 30-55 mA (protons). The remaining bunches contained 17 unpaired *p* bunches, 15 unpaired e^+ bunches, and 24 empty bunches, used for background estimation. Each bunch was separated by 28.8 m, corresponding to 96 ns, since the particles travel close to the speed of light.

A crucial parameter describing a colliding-beam facility is its luminosity, $\mathcal{L}$. The observed event rate R of a process with cross-section σ is related to the luminosity by:

$$R = \mathcal{L} \cdot \sigma \tag{2-3}$$

From the machine parameters, the luminosity is determined by:

$$\mathcal{L} = \frac{f k N_e N_p}{2\pi \sqrt{\sigma_{x_e}^2 + \sigma_{x_p}^2} \sqrt{\sigma_{y_e}^2 + \sigma_{y_p}^2}} \tag{2-4}$$

where f is the revolution frequency (47.3 kHz for HERA), k is the number of colliding bunches, N_e and N_p are the number of electrons and protons per bunch, and σ_x, σ_y are the horizontal and vertical RMS dimensions of the electron and proton beams. The HERA design luminosity is $1.6 \times 10^{31} \text{cm}^{-2}\text{s}^{-1}$.

The integrated luminosity delivered by HERA in 1992, 1993, and 1994 is plotted in Figure 2-3 (a), as a function of time in days. One notes the large increase in luminosity of 1994 over 1992 and 1993. The usable ZEUS luminosity, referred to as the *on-tape* luminosity, is shown in Figure 2-3 (b), as well as the luminosity collected on a daily basis, which approached 0.1 pb^{-1} / day near the end of running. A break-

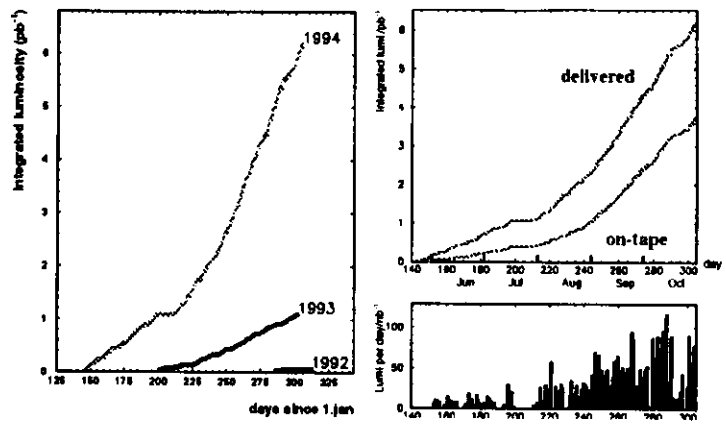

(a) HERA Luminosity *(b) ZEUS On-Tape 1994*

Figure 2-3 *Luminosity delivered by HERA in 1992, 1993 and 1994, and the 1994 ZEUS luminosity stored on tape.*

Type of run	Integrated Luminosity (pb^{-1})
HERA Delivered e^+ and e^-.	6.186 ± 0.093
ZEUS on-tape e^+ and e^-.	3.712 ± 0.056
Apply EVTAKE.	3.301 ± 0.048
Select e^+ runs.	3.022 ± 045
Select nominal vertex.	2.989 ± 0.045

Table 2-1 *The 1994 luminosity.*

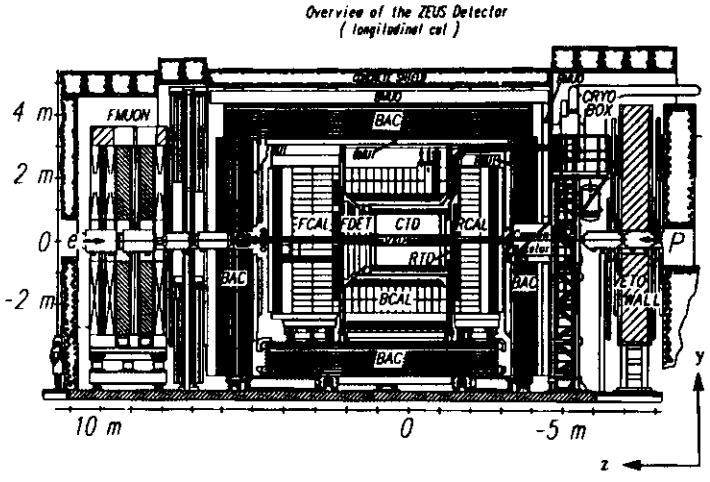

Figure 2-4 *A cross-section of the ZEUS detector along the beam axis.*

down of the 1994 luminosity is given in Table 2-1, including the amount delivered by HERA and recorded by ZEUS. Offline, some runs are rejected due to faulty detector conditions, by a software routine referred to as EVTAKE. For the analysis in this thesis, to ensure stable trigger conditions, only positron runs are selected. Finally, two special runs taken with a shifted z-vertex are removed. The resulting luminosity is 2.989 ± 0.045 pb^{-1}.

2.2 The ZEUS Detector

The layout of the detector is shown in Figure 2-4 and Figure 2-5 [43]. The essential components are a vertex detector (VXD), a central tracking detector (CTD) and transition radiation detector (TRD) (not shown), and forward and rear planar drift chambers (FTD, RTD). The FTD and TRD comprise the forward detectors (FDET). The inner detectors are surrounded by a thin magnetic solenoid coil, a calorimeter divided into forward (FCAL), rear (RCAL) and barrel (BCAL) sections, a backing calorimeter (BAC), barrel and rear muon detectors (BMU, RMU), and a forward muon spectrometer (FMU). In addition to the main detector, there are rear photon and electron taggers (LUMI) for luminosity measurement and electron tagging, as well as forward detectors for elastically-scattered protons (LPS), and neutrons (FNC) (not shown).

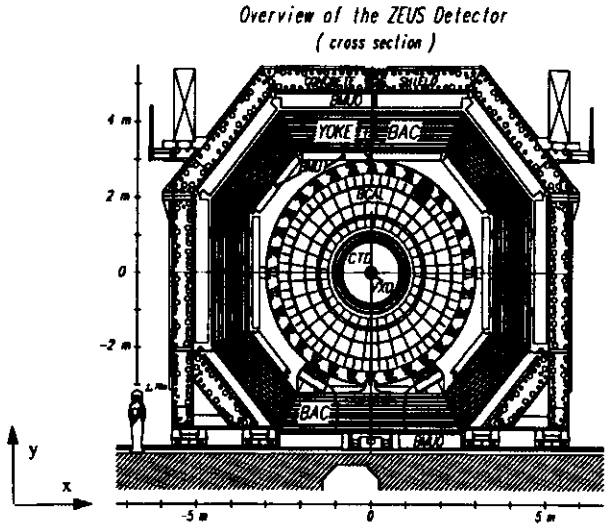

Figure 2-5 *A cross-section of the ZEUS detector in the xy plane.*

The ZEUS coordinates are defined with reference to the proton beam. In Figure 2-4, the proton beam enters from the right, along the negative z-axis. The electron beam enters from the left, along the positive z-axis. The interaction point of the two beams defines the point $z = 0$.

2.2.1 The Central Tracking Detectors

Charged particles are detected by the inner tracking chambers, which are in a 1.43 T magnetic field, generated by the superconducting coil. The detector closest to the beampipe is the VXD, composed of 120 radial cells, each having 12 sense wires of gold-plated tungsten. The active length of the wires is 1.59 m. The chamber walls are composed of carbon fibre/epoxy composite, with an inner radius of 9.9 cm and outer radius of 15.9 cm, and a total thickness of 1 X_0. The polar angular acceptance is from 8.6° to 165°. The VXD is filled with dimethyl ether (DME), used as a drift

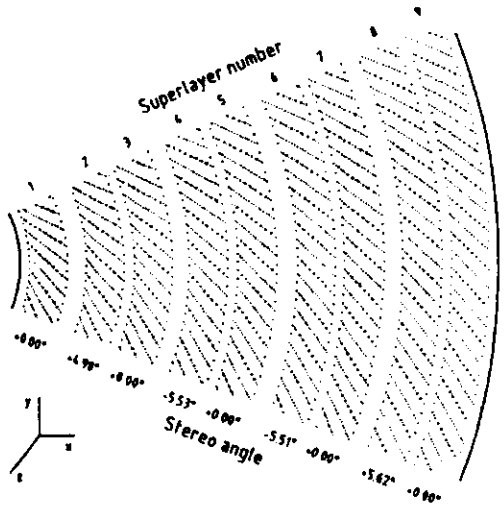

Figure 2-6 *A Segment of the CTD. Sense wires are drawn as groups of eight large points in each superlayer.*

gas due to its slow drift time for ionization electrons, about 15 μm/ns. The slow drift time leads to an improved spatial resolution, which in 1994 was 50 μ in the centre region of a cell and 150 μ near the edges.

Surrounding the VXD is the CTD [44], of which a 45° segment in azimuth is shown in Figure 2-6. The CTD has an outer radius of 85 cm and an overall length of 240 cm. The polar angular coverage is from 15° to 164°. The CTD consists of 72 cylindrical layers, organized into 9 superlayers. Five of the superlayers (1, 3, 5, 7, 9) have their wires parallel to the beam line, and are referred to as axial layers. The remaining four superlayers have wires tilted at approximately ±5°. These provide stereo information to assist in the three-dimensional track reconstruction. There are 4608 sense wires in total. The *Lorentz angle*, the difference in drift angle of ionization electrons with and without an external magnetic field, is designed to be 45° for a field of 1.8 T. Drift distances are measured along an axis perpendicular to a radial line from the centre of the chamber. To resolve left-right hit ambiguities, the planes of wires are oriented at 45° with respect to this line. With the lower-than-design value of the magnetic field of 1.43 T from the superconducting coil, the Lorentz angle in 1994 was 39°. This smaller angle introduces a slight asymmetry in the number of measured hits between positively- and negatively-charged tracks (see Section 6.1).

The chamber is instrumented with a readout system of 100 MHz Flash Analogue to Digital Converters (FADC). These provide a drift time and pulse height from the signals from each wire, giving a design precision in (r, φ) of 100 to 200 μm and design dE/dx (see Section 4.5.1) accuracy of about 6%. In addition, wires in superlayer one and alternate wires in superlayers three and five have a *z-by-timing* readout. This allows for the z-coordinate of a hit to be determined by comparing the difference in arrival times of signals from each end of the chamber. This gives a design precision of 3 cm on the z-coordinate.

In 1994, the CTD working gas was a mixture of Ar (85%), CO_2 (8%) and ethane (7%), bubbled through ethanol. The single hit-efficiency was around 95%, while the single hit resolution was 260μ. For isolated tracks, the tracking efficiency was better than 98%, while for multi-track events it was at least 95%. The momentum resolution for full-length tracks was:

$$\frac{\sigma(p_T)}{p_T} \equiv 0.005 p_T(GeV) \oplus 0.016 \qquad (2\text{-}5)$$

The resolution is a function of the track reconstructed transverse momentum, defined as $p_T = p\sin(\theta)$, where p is the track momentum and θ is the track polar angle (see Section 4.1). The term $\oplus$ means that the error is added in quadrature. Combined data from both chambers in 1994 gave a vertex resolution of 1.4 cm in z and 0.1 cm in the r, φ plane (see Section 4.4.2 for vertex reconstruction).

2.2.2 Calorimetry

Calorimeters are designed to measure the energy of incident charged and neutral particles by absorbing a particle's energy and generating a signal proportional to the energy. In homogeneous calorimeters, such as a lead-glass calorimeter, the absorber also functions as a signal generator. In sampling calorimeters, layers of active material between the absorber layers sample a particle's energy loss.

The energy loss of electrons above 100 MeV occurs primarily through bremsstrahlung (see Section 2.2.4). The majority of the radiated photons with energy above 10 MeV will produce e^+e^- pairs. These pairs radiate more photons, which can lead to an electromagnetic shower. The shower develops until the particles

reach a critical energy, below which electrons lose energy by ionization and excitation, and photons undergo Compton scattering.

The longitudinal depth of an electromagnetic shower is characterized by its radiation length, X_0, which is the average distance in a material in which an incident particle energy decreases to $1/e$ (63%) of its initial value. Containment of 98% of the electromagnetic shower from scattered electrons at HERA energies is achieved within a depth of 25 X_0. In the longitudinal spread of the shower, 95% of the energy is contained within a circle of radius two Moliere radii, ρ_M, which is about 2 cm in uranium.

Hadrons lose energy in a material by ionization, if charged, and through interactions with the nucleii of the material. Struck nucleons may collide with other nucleons in the material, resulting in a hadronic shower. The dimension of a hadronic shower is characterized by the nuclear interaction length, λ. About 95% of the energy of a hadronic shower energy is contained within a depth of $0.2 ln E + 2.5 E^{0.13} + 0.7$ interactions lengths and a circle of radius of 1λ [45]. Hadronic showers have three processes of energy loss: an electromagnetic component, primarily from the decay $\pi^0 \rightarrow \gamma\gamma$, an ionization component from charged secondaries, and a component from nuclear breakups. Fluctuations in these interactions lead to varying calorimeter responses to a hadronic shower and worsen the energy resolution. Typical hadronic calorimeters use iron or lead, which results in a relatively poor resolution of $\sigma(E)/E \approx 60\%/\sqrt{E}$. One solution to this problem is to design a calorimeter to be *compensating*, such that it has an equal response to electrons (e) and hadrons (h), that is: $e/h = 1$.

2.2.2.1 The ZEUS Calorimeter

ZEUS uses a sampling calorimeter, constructed of towers of alternating layers of depleted uranium (U^{238} or DU) plates clad in stainless steel and plastic scintillator tiles. A module of towers from FCAL is depicted in Figure 2-7. The uranium plates are 3.3 mm thick, while the scintillators are 2.6 mm thick. Each tower is segmented into an electromagnetic (EMC) section, about 25 X_0 for electrons or 1λ for hadrons, and two (one in RCAL) hadronic (HAC) sections, each 3λ deep. The EMC section is divided into cells, four 5 x 20 cm^2 cells in FCAL and BCAL towers and two 10 x 20 cm^2 cells in RCAL towers. On either side of the cells are wavelength shifter bars, which absorb and re-emit scintillator light and guide it to photomultiplier tubes (PMT's), one pair for each cell. Twenty-three modules comprise FCAL and RCAL, while 32 wedge-shaped modules make up BCAL. The FCAL covers the polar

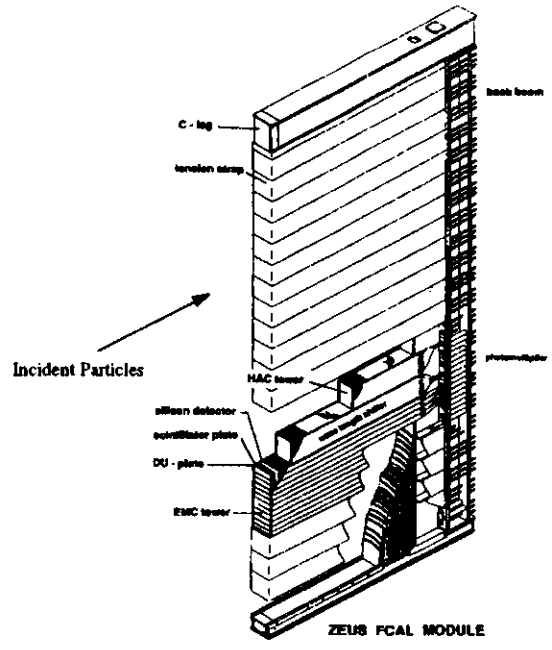

Figure 2-7 *A Module of the FCAL. The cutaway shows the alternating layers of depleted uranium and plastic scintillator, and the wavelength shifters along the sides.*

angular region $2.2° < \theta < 39.9°$, the BCAL $36.7° < \theta < 129.1°$, and the RCAL $128.1° < \theta < 176.5°$, giving a coverage of 99.8% in the forward hemisphere and 99.5% in the rear.

Compensation is achieved in the ZEUS calorimeter by improving the response to hadronic showers in the active layers. Neutrons from a hadronic shower will undergo elastic collisions with free protons in the scintillator. The scintillator response to the resulting ionizing protons can be tuned by varying the layer thickness. Furthermore, low-energy neutrons can cause the U^{238} to fission, releasing 7.4

MeV gamma rays and neutrons. The fission neutrons in turn scatter elastically off protons in the scintillator, which add to the shower signal.

In test beams, the energy resolution of the calorimeter was measured to be $\sigma(E)/E = 35\%/\sqrt{E} \oplus 2\%$ for hadrons, while for electrons it was measured to be $\sigma(E)/E = 18\%/\sqrt{E} \oplus 1\%$, where $\oplus$ refers to addition in quadrature.

The calibration of the calorimeter is monitored by the uranium noise (UNO) or radioactivity signal, charge injection into the electronics readout, laser light injection into the PMT's, and ^{60}Co source scans. Variations in the UNO signal over time periods less than a day are below 0.5%. Variations in the calibration over several days are about 3%, and are due to changes in PMT gains. These variations are corrected by scaling the measured UNO signal to the nominal UNO signal.

2.2.3 The Small Rear Track Detector

Covering the inner ring of towers of the RCAL at z = -148 cm is the small rear track detector (SRTD). It consists of an array of scintillator strips, each 10 mm wide, in one horizontal layer and one vertical layer. It covers an area of 68 x 68 cm^2, and serves as a presampler for scattered electrons to correct for energy loss in dead material between the interaction region and the rear calorimeter. Electrons passing through this dead material may initiate an electromagnetic shower, which is not detected by the RCAL. In addition, the SRTD provides a timing signal used in the trigger to separate ep collisions from background events.

2.2.4 The Luminosity Monitor

Fast luminosity monitoring is achieved through a measurement of the bremsstrahlung process $ep \rightarrow e'p\gamma$. These are photons which are emitted at very small angles with respect to the direction of the incoming electron. The cross section for the bremsstrahlung process is large and can be calculated accurately. The cross-section is given by the Bethe-Heitler formula:

$$\frac{d\sigma}{dk} = 4\alpha r_e^2 \frac{E'}{kE}\left(\frac{E}{E'} + \frac{E'}{E} - \frac{2}{3}\right)\left(ln\frac{4E_pEE'}{m_pm_ek} - \frac{1}{2}\right) \qquad (2\text{-}6)$$

where k is the photon energy, E and E' are the initial and scattered electron energies, E_p is the proton energy, m_e, m_p are the electron and proton masses respectively, α is the fine structure constant, and r_e is the classical radius of the electron. To calculate the luminosity of ep collisions using this formula, a background contribution must be subtracted. This background arises from the interaction of electrons

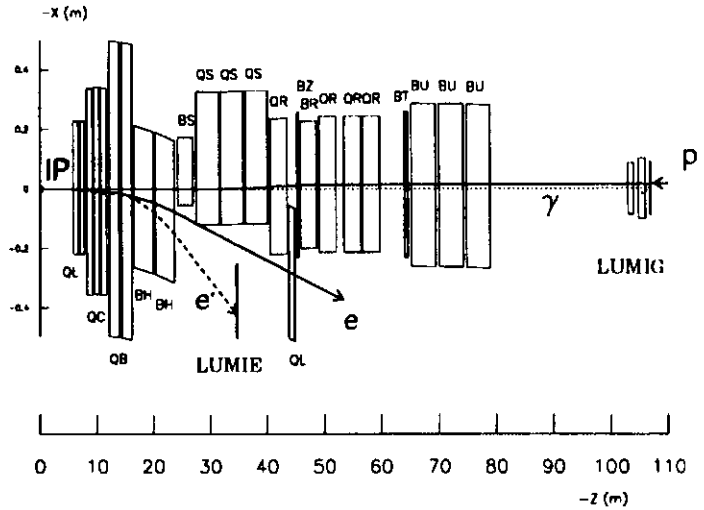

Figure 2-8 *A schematic of the ZEUS luminosity detector. Figure reproduced from [56].*

with the residual gas in the beam line. To determine the rate of this background, measurements are taken with electron pilot bunches, which are electron bunches that collide with an empty proton bunch in the interaction region.

The general layout of the detection scheme is shown in Figure 2-8. The luminosity monitor consists of the photon detector (LUMIG) close to the proton beam pipe at a distance of 107 m from the ZEUS interaction region, and an electron detector (LUMIE) near the electron beam at a distance of 35 m. Both devices are constructed from 5.7 cm thick lead plates interleaved with 2.8 mm scintillators. The LUMIG is 18 x 18 cm^2 with a depth of 22 X_0, while the LUMIE is 25 x 25 cm^2 with a depth of 24 X_0. The bremsstrahlung photons propagate inside the proton pipe and exit it 80 m from the interaction point (IP) after a vertical bend of the proton beam by a magnet. Electrons from bremsstrahlung events and photoproduction are deflected out of the beam pipe by electron beam magnets, accepting electrons with an energy $0.2 \leq E'/E \leq 0.9$.

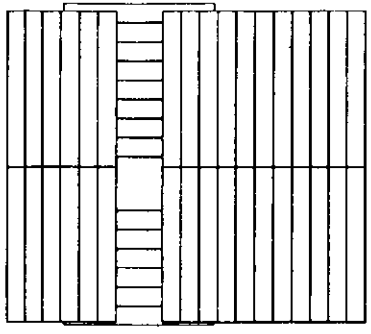

Figure 2-9 *One side of the Vetowall scintillator counters.*

2.2.5 The C5 Counters

Located around the beam pipe, near the C5 collimator at $z = -3.15$ m, is a set of four small scintillators, forming the C5 detector. The detector measures rates and arrival times of particles from the halos of the electron and proton beams. In addition, particles created by interactions of the beam with residual gas, elements of the beam pipe, or the C5 collimator are detected. Online in the trigger and offline, the timing information is used to veto these events. The difference in C5 timing between the proton and electron beam halos is used to monitor the position of the interaction point online.

2.2.6 The Vetowall

Located in the rear (proton) region at $z = -7.27$ m is the Vetowall. It is constructed of an iron wall with scintillator hodoscopes (many counters in parallel) on either side. One side, viewed from the ZEUS detector, is illustrated in Figure 2-9. The Vetowall is 8 m wide and 9 m tall, 0.87 m thick, and perpendicular to the beam line, with an 0.8 m x 0.8 m hole in the centre for the beam pipe. Like the C5 counter, it allows the trigger to reject beam-gas events, having a coincidence in both counters. In addition, it serves to shield the main detector from proton-beam events.

Chapter 3

The ZEUS Data Acquisition System

3.1 Overview

The components of the ZEUS detector correspond to a total of about 250,000 electronic channels. For each interaction, they generate an event data record about 100 kB in size. The HERA beams cross at a rate of 10.4 MHz or once every 96 ns, and at the design luminosity about 1% of these crossings (several hundred kHz) will produce a signal in ZEUS. If every event were read out, this would require an archiving bandwidth of 10 GB/s. This rate can neither be stored on tape nor analyzed afterwards, using present storage technology.

The high background rate arises largely from proton beam interactions with the residual gas in the beam pipe and with the wall of the beam pipe in the 70 m straight section of HERA upstream of ZEUS. In contrast, *ep* interactions are of $O(100)$ Hz, which are mostly photoproduction and a few Hz of deep inelastic scattering (see Section 4.1). The output to tape rate is limited to $O(5)$ Hz. To achieve this, the ZEUS Data Acquisition System (DAQ) [46] employs three levels of triggering, as illustrated in Figure 3-1. The design of each level is determined by the decision time available. The First Level Trigger (FLT) must handle an input rate of several hundred kHz and reduce this to about 1 kHz. The Second Level Trigger (SLT) must reduce the output from the FLT to about 100 Hz within a few ms. The Third Level Trigger (TLT) must reduce the 100 Hz from the SLT to about 5 Hz.

An event picture of a typical beam-gas event is shown in Figure 3-2. In this event, an interaction has occurred upstream of the ZEUS detector in the direction of the proton beam, which is in the negative z-direction. Particles pointing to the interaction vertex are visible as reconstructed tracks in the CTD. In this case, the tracks were reconstructed online by the TLT (see Section 3.5.5). Another characteristic of beam-gas events is the concentration of energy deposits in the inner ring of

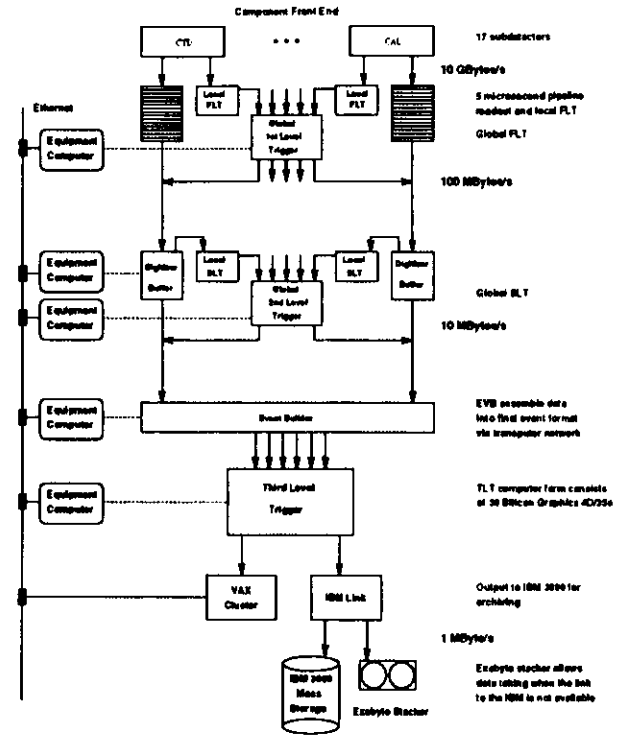

Figure 3-1 *A schematic of the ZEUS trigger system.*

FCAL towers around the beampipe, and little energy in the rest of the calorimeter. The energy deposits in this event are drawn as filled rectangles, with the area proportional to the measured energy.

An indication of the beam-gas background rate is provided by the trigger rate of the C5 detector (described in Section 2.2.5). As shown in Figure 3-3, the background rate ranged from a few hundred Hz in 1992 to tens of kHz in 1994, and scaled with increased luminosity. This figure also shows the output rates for the FLT, SLT, and TLT. One notes the improvement in the triggers over time, maintaining the nec-

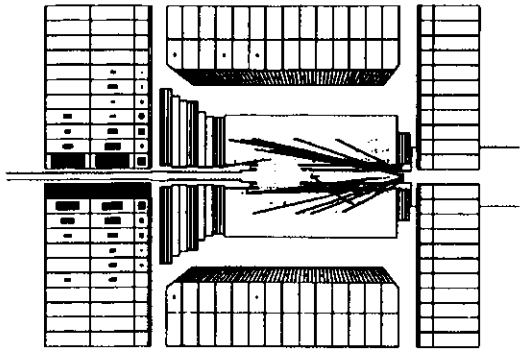

Figure 3-2 *An event picture of a beam-gas interaction.*

essary reduction despite the two orders of magnitude increase in luminosity and background rates.

An important requirement of the trigger system is that it perform without *deadtime*. Deadtime refers to a period of time during which the readout is inactive. The FLT operates at the clock rate of HERA and is without deadtime. However, at the SLT deadtime can occur when the component analogue signals are digitized, during this time no new data can be stored. An added complication is the fact that several components do not receive their signals until several beam crossings after an interaction has taken place. For example, ionization electrons in the CTD gas drift at a speed of about 50 μm/ns, and may travel distances of up to 1-2 cm before reaching a sense wire. The drift distance depends upon which part of a CTD cell is traversed by a charged particle, and the drift time can introduce a delay of O(10-30) clock cycles before a complete CTD wire signal can be digitized.

The solution to the problem of deadtime and delayed signals is a data pipeline (FIFO)[1], in which data are entered every clock cycle of 96 ns. The length of the pipeline is chosen such that the slowest component can process its data. Account is also made for signal propagation delays due to cabling. Also, sufficient time must be allotted for the local and global processors to analyze an event.

1. First In First Out

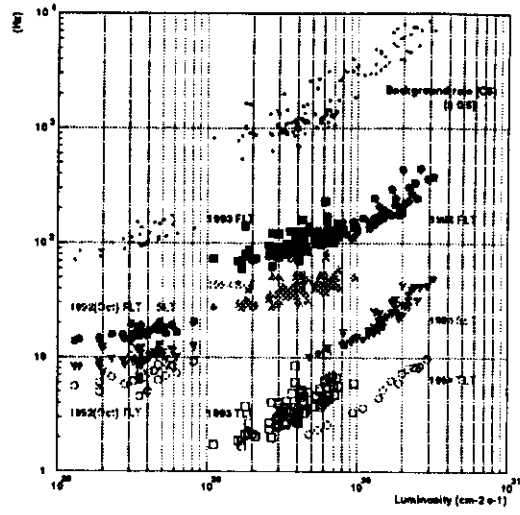

Figure 3-3 *The ZEUS trigger rates versus luminosity for 1992-1994. The vertical axis gives the trigger rate, while the horizontal axis gives the instantaneous luminosity.*

3.2 The First Level Trigger (FLT)

The FLT consists of local component processors whose decisions are sent to a Global First Level Trigger (GFLT). The GFLT allows 26 clock cycles for the local FLT components to evaluate their data and send a result to the GFLT. Within another 20 clock cycles the GFLT must provide an event decision based on these data. This requires that, allowing for delays in signal propagation, the component pipelines must be 58 clock cycles or 5 μs in length.

This analysis in this thesis makes use of the Calorimeter First Level Trigger (CAL-FLT) [47] and CTD First Level Trigger (CTD-FLT) [48] information. The CAL-FLT calculates global energy sums (see Section 5.1.1), in calorimeter towers, which are blocks of 4 cells for FCAL and BCAL, and 2 cells for RCAL. These energy sums are compared by the GFLT to threshold values in memory lookup tables.

The CTD-FLT searches for CTD tracks in an event coming from the interaction region. These tracks are used to reject beam-gas events which originate from

the incoming proton direction. The CTD-FLT achieves track reconstruction using the CTD z-by-timing data from superlayer one. For each event, a processor compares the data with predetermined masks or patterns of hits. The CTD-FLT selection cuts are described in Section 5.1.1.

If the GFLT accepts an event, the components are signalled and the pipelines stopped. Analogue signals from the components are digitized, and the data is transferred to buffers accessible by the Global Second Level Trigger (GSLT).

3.3 The Second Level Trigger (SLT)

The SLT has available to it a decision time of a few ms, and so it can be implemented on programmable processors (a *transputer*[1] network). Iterative algorithms can be executed on these processors. For example, the CAL-SLT utilizes an algorithm to search for clusters, which are adjacent energy deposits in the calorimeter. These clusters can be used to identify the primary scattered electron in an *ep* collision. The CAL-SLT also calculates global energy sums, using the data from calorimeter cells.

Background rejection at the SLT [49] is performed using timing information from the calorimeter (see also Section 3.5). Particles originating from an *ep* collision at the nominal interaction point and travelling near the speed of light are defined to arrive at time $t = 0$ at the faces of the calorimeter. In contrast, events originating upstream of the detector produce earlier signals in RCAL, at $t \sim -10$ ns. An event at the SLT is vetoed if the RCAL time is:

$$|t_{RCAL}| > 8 \text{ ns}, \tag{3-1}$$

or the FCAL-RCAL time difference is:

$$|t_{FCAL} - t_{RCAL}| > 8 \text{ ns}, \tag{3-2}$$

or the FCAL time is:

$$|t_{RCAL}| > 8 \text{ ns}. \tag{3-3}$$

Cosmic-ray induced events are rejected based on the difference between the upper and lower BCAL calorimeter time (see also Section 3.5.4). These events enter at the

1. Processor, memory, and communications hardware on a single chip.

top of the ZEUS detector due to their cosmic origin, and are vetoed if the measured time:

$$(t_{up} - t_{down}) > -10 \text{ ns}. \tag{3-4}$$

Another source of background signals are *spark* events. A spark occurs when a calorimeter phototube at high voltage discharges to ground. This occurs because insufficient clearance was left in the PMT assembly. An event is identified as a spark by the SLT if the event has only one PMT signal with energy above 2 GeV and there are no other PMT signals with energy above 200 MeV.

The SLT also uses data from the LUMI (see Section 2.2.4) to detect scattered electrons from photoproduction and photons from radiative events. The analysis in this thesis makes use of the CAL SLT and LUMI SLT.

The Global Second Level Trigger (GSLT) combines data from the component SLT processors, and forms a trigger decision. The trigger decision is based on a set of *physics filters*. These are algorithms designed to select specific physics processes, and are modelled on the Third Level Trigger filters (Section 3.5.6). If an event passes one of the GSLT filters it is accepted.

3.4 The Event Builder (EVB)

Once an event has been accepted by the GSLT, the data from the various components are assembled into a complete event by the Event Builder (EVB) for transmission to the TLT. Data are transferred over EVB transputer links into a 512 KB triple-ported memory (TPM) in a two transputer (2TP) module. The EVB has six such modules in total. Each component formats the data according to a ZEBRA[1] structure. The ZEBRA structure is reformatted by the EVB according to the ADAMO protocol, which is a tabular data format. The ADAMO tables from each component are combined into one data record in the 2TP module for access by the Third Level Trigger.

3.5 The Third Level Trigger (TLT)

The TLT is the first level to have access to the complete raw event data, and so the global quantities of an event may be exploited. In principle, any offline selection can be performed at the TLT, limited only by CPU time. The TLT must provide sufficient processing power to allow for the execution of iterative offline algorithms,

1. A linked data structure produced by CERN.

such as extensive track and vertex fitting, electron identification and jet reconstruction. This results in the requirement of several MIPS[1]-seconds of computing power per event. To avoid the duplication of code, the system must also provide an 'offline environment' for the developers. This includes a reliable operating system and a thoroughly tested compiler, which may not be available in purpose-built hardware.

3.5.1 The Hardware Design

The TLT consists of a computer "farm" of 30 commercial RISC[2] R3000/R3100 machines (SGI 4D/35S), each with a clock speed of 36 MHz, giving a total processing power in excess of 1000 MIPS. For an input rate of 100 Hz spread out over 30 processors, about 300 ms on average of analysis time is available for each trigger decision. Each processor is equipped with 32 MB memory, which sets an upper limit on the size of memory-resident code.

The TLT processors are divided into 6 branches of five "analyzers", processors which perform online event reconstruction and make a trigger decision. One of these branches is shown in Figure 3-4. In addition to the analyzers, control and communication is supervised by a "manager" node (SGI 25/S). Each branch is connected by a Fermilab Branchbus [50] to a TPM buffer located on the EVB VME crate. Control signals from the manager are passed along a local ethernet. The six branches are coordinated by a single *control_TLT* process running on an SGI 4D/35G processor (not shown), which also communicates with the overall Run Control System, and performs handshaking with the EVB and IBM output. In 1994, events which were selected by the TLT were transferred via a Branchbus Switch to an output node, which sent the date by optical fibre link to an IBM computer for tape storage.

A UNIX operating environment is provided, including *nfs* and *telnet*, as well as FORTRAN and C compilers. This allows a user to log into any node of the system and examine log files or interactively debug code. The standard CERN [51] libraries, such as HBOOK and GEANT, are available. This programming environment has proven to be very valuable in the software design, debugging, and testing stage.

3.5.2 The Performance of the TLT

From the start of ZEUS data taking in 1992 to the present, the TLT has been crucial to the experiment. The first trigger used in the TLT was the calorimeter

1. Million Instructions Per Second.
2. Reduced Instruction Set Computer, as opposed to the CISC (Complex Instruction Set) used in a PC 8x86 processor.

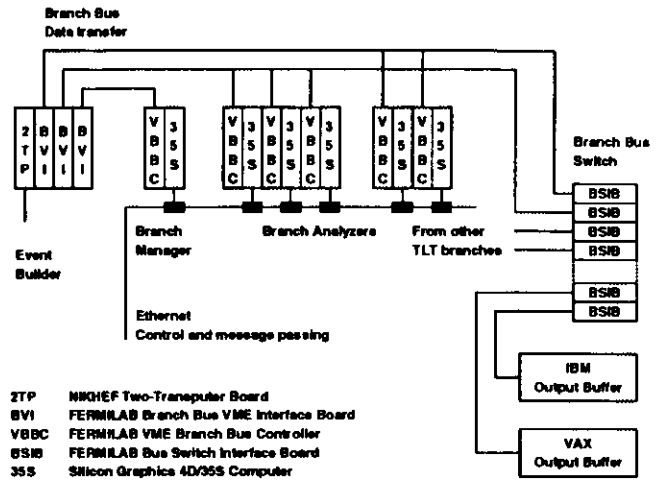

Figure 3-4 *A schematic of a TLT hardware branch.*

'spark' cut (see Section 3.3). Approximately 30% of the raw data in 1992 fell into this category. A cut of this nature was not foreseen in the initial trigger design. The 1992 configuration of the FLT could not cut these events without hardware changes. The SLT could in principle cut these events, but its processors had been designed three years earlier to have access to data from calorimeter cells only, and not individual PMT's. At the TLT, the calorimeter reconstruction code was modified to flag spark events. Independent analysis code was then run offline to verify the performance of the algorithm and to determine the safety of the cut. Once the cut was determined to be safe, it was switched on in the TLT.

The second cut employed in the TLT was calorimeter timing, detailed in Section 3.5.3. Before enabling this cut, the same process of offline verification was followed. An additional background reduction of 25% was made possible using this cut. As a further check on the efficiency of this trigger, a fraction of the events flagged as background were still output to tape. Online track reconstruction was also enabled in 1992 (see Section 3.5.5). This reconstruction was used to flag events as beam gas, if three or more well-reconstructed tracks were found outside the primary interaction region.

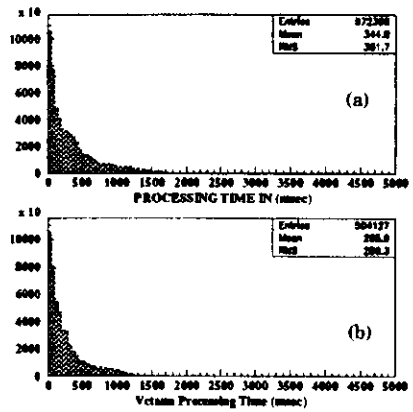

Figure 3-5 *The CPU processing time required by the TLT algorithms. Figure (a) gives the total CPU time, and figure (b) gives the track reconstruction time.*

The TLT has proven to be very powerful for the study, and implementation, of new cuts. Since the algorithms are written in FORTRAN, any physicist can easily examine and understand the routines. The development time for the first trigger cuts was almost entirely spent in offline physics testing. The calorimeter trigger algorithms were basically flagging events online in the TLT within one day after their design. During the development stage, a code writer can execute the TLT analysis software reading by raw data from a file, and step through the code with a full debugger. Compilation and linking times are generally on the order of 10 minutes or less. Once the code has been debugged, it is distributed to the TLT nodes over ethernet via a remote copy program (the distribution to 30 nodes typically requires 10 minutes). The online performance of the software is monitored in several ways, through histograms, a statistics-gathering module, and through log files (see Section 3.5.7). The ability for a user to telnet onto an individual machine and examine a log file is very helpful in monitoring performance.

The current programs run in the TLT are generated from about 40,000 lines of FORTRAN analysis code and about 37,000 lines of C control code. Typical CPU processing times are shown in Figure 3-5. The distribution of total processing time required by the TLT in 1994 is given in Figure 3-5 (a). This indicates a mean processing time of about 340 ms. Of this time, about 270 ms were required by the track reconstruction algorithm.

During the running period of 1994, the Third Level Trigger continued to be an essential component of ZEUS. Under normal operation, the final stage trigger is implemented last. However, the flexibility of the ZEUS trigger system allows for a quick response to unexpected sources of high rates. The TLT is a powerful, fast, and easily debugged system, with the ability to adapt to conditions unforeseen in the original trigger or detector design.

3.5.3 The TLT Trigger Decision

The TLT trigger decision is made in two stages, shown in a flow chart in Figure 3-6. The first stage is the fast identification of background events, while maintaining a high efficiency for physics, and relies on calorimeter and track reconstruction, and muon identification. The second stage is the selection of physics candidates, based on offline algorithms. To provide monitoring of the background rejection algorithms and physics filters, a fraction of events is retained after background rejection; these events are indicated as "TLT passthru" in Figure 3-6. A second sample is retained after physics filters; these events are marked as "TLT Sampling Filter" events. For example, the rejection factor of a given filter can be estimated using these events.

The first step of background rejection exploits the full information of the ZEUS calorimeter. Spark rejection (Section 3.3) is performed at the TLT using the left and right PMT information of each cell. This is in contrast to the SLT spark rejection algorithm, which has access only to the summed PMT signals. As a spark usually occurs in only one PMT in a given cell, it may be identified by a large left-right asymmetry in cell energy:

$$\text{asymmetry} = \left|\frac{L-R}{L+R}\right| > 0.9 \qquad (3\text{-}5)$$

where L, R are the energies of the left and right PMT signals. An online TLT asymmetry distribution is given in Figure 3-7 (a) from a typical luminosity run. Spark events are visible in this plot as peaks near an asymmetry of ± 1. Events are rejected at the TLT if they contain a spark candidate with a cell energy sum of $L+R > 1.5$ GeV, and if the energy in the remainder of the calorimeter is less than 2 GeV.

Typical calorimeter global energy sums calculated by the TLT are shown in

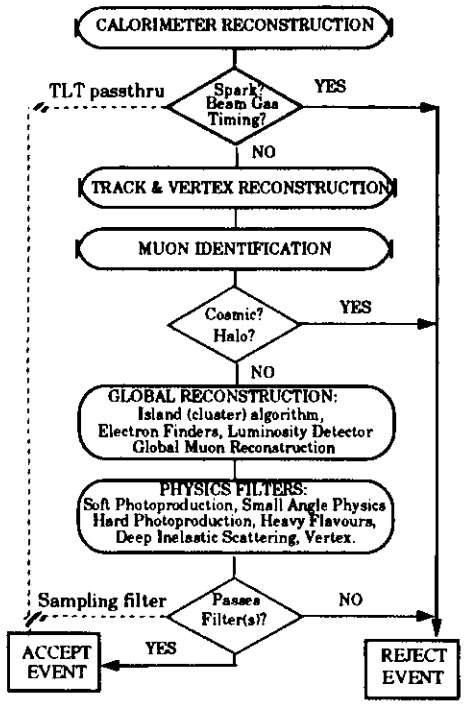

Figure 3-6 *Flow chart outlining the TLT trigger decision.*

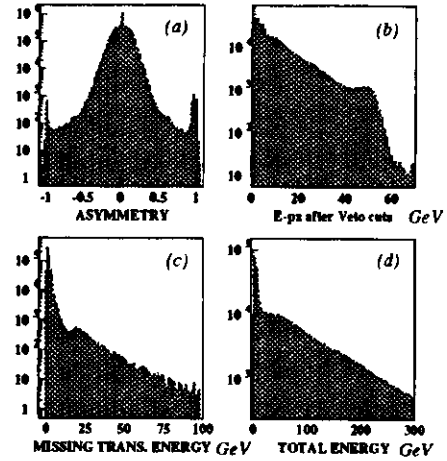

Figure 3-7 *Distributions of PMT asymmetries and calorimeter global energy sums calculated online by the TLT.*

Figure 3-7. These sums include the quantity $E-p_z$ (see Section 4.1), the missing transverse energy (see Section 4.3), and the total calorimeter energy. The global energy sums are exploited by the physics filters (Section 3.5.6)

To reject beam-gas interactions, calorimeter timing cuts are made [52]. An energy-weighted time is calculated for the regions FCAL, RCAL, and the combined region F/B/RCAL (Global time). Participating PMT signals must be 200 MeV or greater. The error on the time measurement (in ns) of a PMT signal as a function of its energy is parameterized as:

$$\sigma = a + \left(\frac{b}{E}\right)^{c} \qquad (3\text{-}6)$$

where a=0.4, b=1.4, and c=0.65. The time average for a region j is calculated as:

$$t_j = \frac{\sum_i (t_i/\sigma_i^2)}{\sum_i (1/\sigma_i^2)} \qquad (3\text{-}7)$$

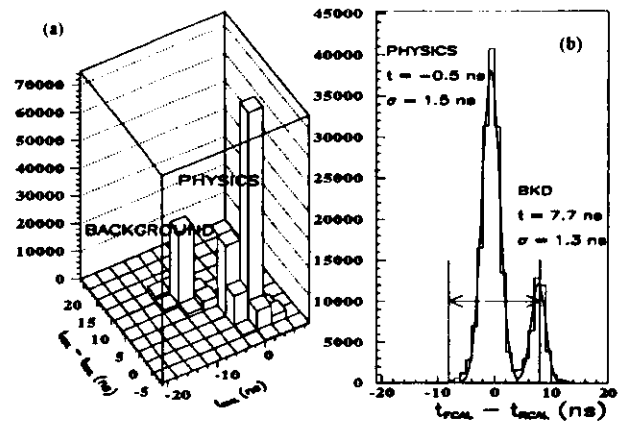

Figure 3-8 *TLT online calorimeter timing distributions.*

where the error on the regional time is:

$$\sigma_j = \left(\sum_i (1/\sigma_i^2) \right)^{-1/2} \tag{3-9}$$

Figure 3-8 shows online TLT timing distributions using this calculation. Figure 3-8 (a) shows the distribution of the measured FCAL minus RCAL time difference versus the RCAL time, while Figure 3-8 (b) shows the measured FCAL-RCAL time difference. One notes the clear physics peak, centered near zero RCAL time, and the background peak at negative (early) RCAL times.

An event is rejected if there is sufficient energy in a region (1 GeV for the RCAL and Global regions and 2 GeV for the FCAL) and if one of the conditions:

$$|t_{Global}| > max(8, 3\sigma_{t_{Global}}) \tag{3-9}$$

$$|t_{RCAL}| > max(8, 3\sigma_{t_{RCAL}}) \tag{3-10}$$

$$|t_{FCAL}| > max(8, 3\sigma_{t_{FCAL}}) \tag{3-11}$$

$$|t_{FCAL} - t_{RCAL}| > max(8, 3\sqrt{\sigma_{t_{FCAL}}^2 + \sigma_{t_{RCAL}}^2}) \tag{3-12}$$

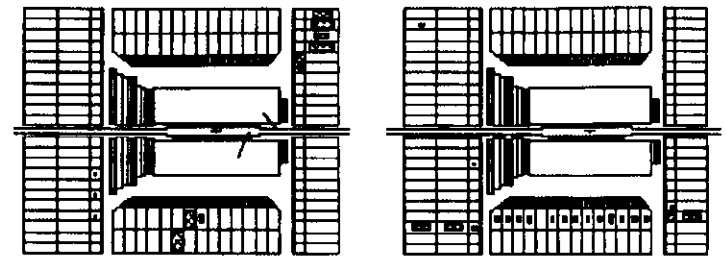

(a) Cosmic (b) Beam Halo

Figure 3-9 *Cosmic muons and beam halo muons identified by the TLT.*

is satisfied. The cut on the FCAL-RCAL time is shown graphically in Section Figure 3-8 (b) as two lines joined by a double arrow.

3.5.4 The Rejection of Cosmic and Halo Muons

If an event passes the vetoes on sparks and timing, the TLT employs a muon rejection algorithm, MUTRIG [53]. The expected rate of cosmic muons passing through the ZEUS detector is $O(20)$ Hz. Downward travelling muons can be identified by calculating the time difference of signals measured in the upper and lower regions of the calorimeter. For an *ep* event, this transit time will be approximately zero. A downward-travelling particle, however, will have a transit time of about 6 ns in ZEUS. An example of a cosmic muon traversing ZEUS is shown in Figure 3-9 (a). In this event, the muon entered from the upper right corner of the picture, passed through the CTD, and exited in the lower left corner. Two reconstructed TLT tracks are also visible as lines in the CTD.

In addition to cosmics, proton-beam associated halo muons occur at a rate of several Hz. A sample event is shown in Figure 3-9 (b), which depicts a halo muon entering the ZEUS calorimeter from the proton direction. For such muons, the variation of the x and y position of the energy deposits in the calorimeter cells will be small and lie along a straight line. If over 50% of the energy in the calorimeter corresponds to a fitted muon trajectory, the event is identified as a halo and vetoed.

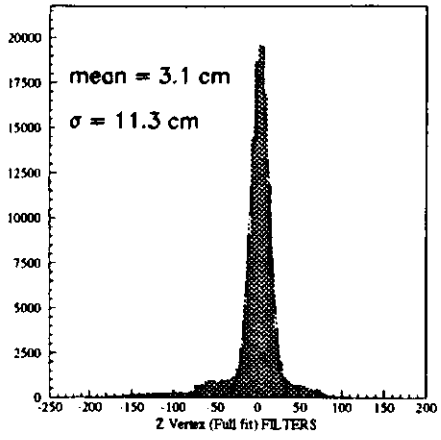

Figure 3-10 *A sample online TLT z-vertex distribution from a luminosity run.*

3.5.5 The Online Track Reconstruction

For further background identification, the TLT performs fast three-dimensional track reconstruction in the CTD. Track reconstruction is exploited in identifying background events that originate outside the interaction region. The tracking information is also used in refining the identification of cosmic muons; events identified by MUTRIG as a cosmic but having a TLT track passing through the nominal interaction point are retained. The TLT has available the full offline tracking algorithm VCTRAK [54], described in Section 4.4, but performs partial reconstruction due to CPU limitations.

The reconstructed tracks are fitted online to estimate the position of the event vertex. The distribution in z is shown in Figure 3-10 for a typical luminosity run (see also Figure 5-3). A Gaussian with varying mean, width, and normalization has been fitted to the data in this distribution. The fit results give a mean of 3.1 cm and a width of 11.3 cm. The tails in the distribution are due to residual beam-gas events, and these can be suppressed with a cut in the measured z-vertex of an event. The analysis in this thesis makes a conservative cut online of $|z_{vertex}| < 75$ cm. Furthermore, the online track reconstruction provides an estimate of the momentum and direction of each track candidate, used in the physics filters (Section 3.5.6)

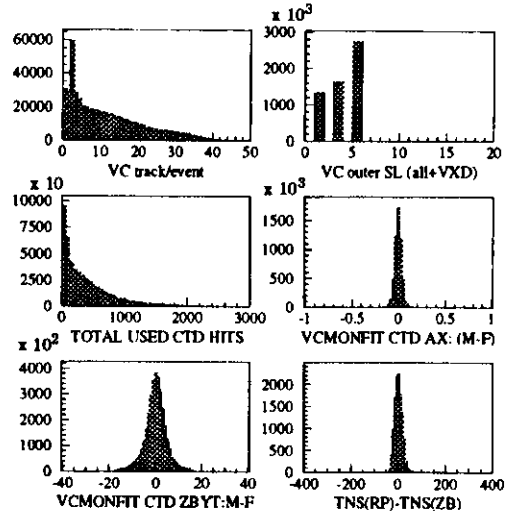

Figure 3-11 *Diagnostic histograms from the TLT online track reconstruction.*

For offline checks, or to develop physics filters, the track parameters are output to the ADAMO table TLTVCHL. Similarly, the reconstructed vertexes are stored in the table TLTVTX. The performance of the tracking is monitored online through a series of histograms, shown in Figure 3-11. Information on the number of tracks reconstructed, the outer superlayer used (layer 5 in 1994), the number of CTD hits, and the fit residuals for axial, z-by-timing, and FADC information are available. Such information is vital to shift crews monitoring the CTD hardware.

The calibration constants and monitoring results are saved run by run. Figure 3-12 shows the history of the FADC global t_0, which is the time offset that must be subtracted from the measured drift times. The values are shown for all 1994 physics runs (8253 to 10263). The small glitches were usually due to special runs. One also notices shifts around run 8800 and 9050; these correspond to three changes to the CTD Master Timing Controller (MTC). Also shown is the drift velocity over the same run period, and the difference between drift time in z-by-timing channels compared to FADC channels. This provides a useful check on the FADC performance.

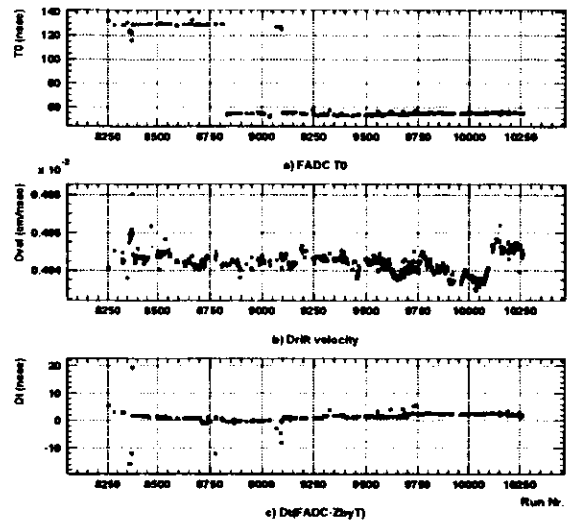

Figure 3-12 *TLT track reconstruction monitoring plots. These monitor a) FADC t_0, b) Drift Velocity v_D, and c) Δt(FADC - ZbyTiming) versus run number [54].*

3.5.6 The Physics Filters

Following the event veto stage, the second stage of classification is physics selection. After the TLT analysis modules have completed reconstruction, an event is classified. The categories include beam-gas background, cosmic-ray background, or a physics candidate. If a module positively identifies an event as background, analysis stops and the event is classified. Depending on the trigger mode sent from the operators, the TLT may either flag the event and pass it, or reject the event.

Since the beam gas background is already very strongly suppressed by the first and second level triggers, the physics groups are obliged to migrate offline filter strategies to the TLT. A list of all the physics filters available in 1994 is given in Figure 3-13. The filters are divided into six major groups, which are soft (low-energy) photoproduction (SPP), deep inelastic scattering (DIS), hard photoproduction (HPP), exotics (EXO), muons (MUO), and heavy flavour production (HFL). There is also a filter (VTX01) which selects a fraction of the events with a reconstructed ver-

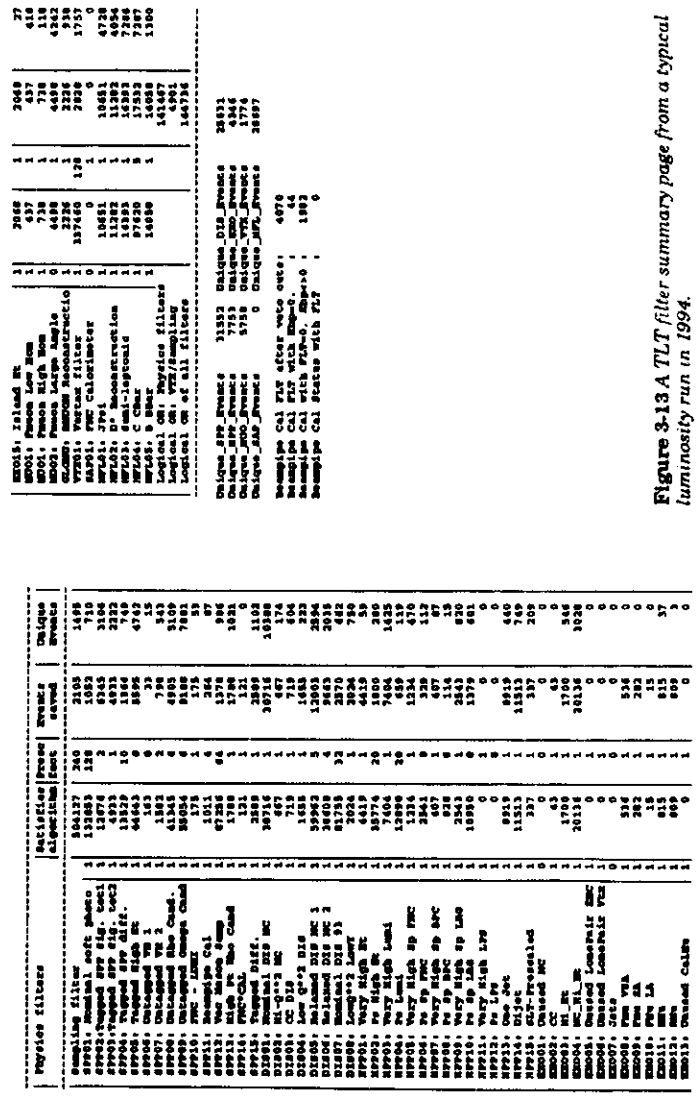

Figure 3-13 *A TLT filter summary page from a typical luminosity run in 1994.*

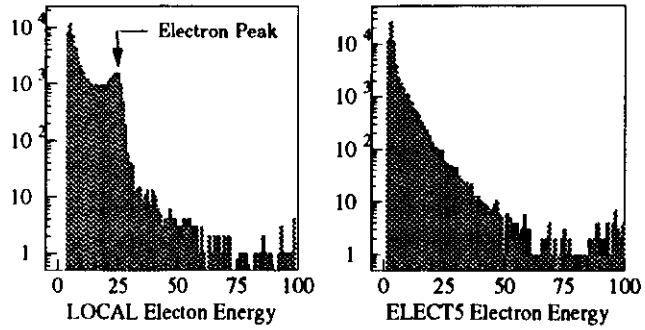

Figure 3-14 *Online TLT histograms from the two electron finders.*

tex, within $|z_{vertex}| < 75$ cm, and a filter (SAP01) which selects events tagged by the FNC (Section 2.2) [55].

The nominal soft photoproduction filter triggers on events in which the scattered electron is tagged by the LUMI electron calorimeter, having a reconstructed energy of 3 GeV or greater. This filter was used primarily in 1993 to measure the total photon-proton cross-section [56]. In 1994, due to the high rate of this filter, it was disabled by a large prescale factor. The production of elastic vector mesons, $ep \rightarrow VX$, where $V = \rho, \omega, \phi$, is selected by requiring a reconstructed vertex with fewer than six CTD tracks, and there must be at least one two-track combination with an invariant mass less than 2.5 GeV, assuming the tracks are $\pi^{\pm}$.

The filters to select neutral-current deep inelastic scattering events rely on the offline electron-identification algorithms, LOCAL [57] and ELECT5 [58], which are interfaced to the TLT. The LOCAL algorithm searches for clusters of energy deposits in the calorimeter, and cuts on the ratio of EMC/HAC energy, while ELECT5 sums the energy within a 11.5° cone around EMC cells. The distributions in reconstructed electron energy from ELEC5 and LOCAL are given in Figure 3-14. A peak at the incident electron energy is evident for LOCAL. ELEC5 does not exhibit a significant peak because it is used only if LOCAL fails to reconstruct an electron candidate (see also Section 5.1.3).

Hard photoproduction events, which include the boson-gluon fusion process (see Section 1.5.1), typically produce one or more jets in the final state. The HPP filters exploit a TLT jet-finding algorithm [59]. The remaining HPP filters make requirements on global energy sums in the calorimeter, which are corrected for the reconstructed z-vertex position of the event (see Section 4.3), which must lie within $|z_{vertex}| < 75$ cm.

Exotic events [60] are searched for in nominal neutral-current DIS events, and in charged-current events, $ep \rightarrow \nu X$, in which the neutrino escapes undetected, resulting in a missing transverse energy in the calorimeter. Exotic events may also produce one or more $\mu^{\pm}$, which are tagged by the muon detectors (see Section 2.2). The TLT performs global muon reconstruction, by matching information from the muon detectors with energy deposits in the calorimeter and reconstructed tracks in the CTD.

Heavy flavour events refer to c and b quark production. The HFL filters exploit the TLT CTD track reconstruction. The $D^{*\pm}$ filter reconstructs the decay channel $D^{*\pm} \rightarrow D^0\pi^{\pm}$, by calculating the invariant mass difference, Δm, between the $D^{*\pm}$ and the D^0 [61]. The decays $J/\psi \rightarrow e^+e^-, \mu^+\mu^-$ are searched for by matching reconstructed CTD tracks with reconstructed calorimeter clusters [62]. The HFL filters used in the analysis in this thesis are described in detail in Section 5.1.3 and Section 5.2.

Figure 3-15 lists the number of events which satisfy each filter, the filter prescale factor, and the number passed after the prescale. After each run, a hardcopy of this list is printed by the TLT.

3.5.7 Online Monitoring

Online monitoring of the TLT is available via online histograms and a monitor display. In addition to the histograms shown in Figures 3-5, 3-7, 3-8, 3-10, 3-11, and 3-14, the number of events selected by each physics filter is displayed in histograms, which are updated every 60 seconds. This information allows the shift crews to monitor the physics filters by comparing them to reference histograms, and for the trigger group to modify a filter if it produces an unacceptably high rate.

The overall status of the TLT is given by a monitor display, shown in Figure 3-15, taken from a typical run in 1994 (run 10009). The display shows the number of TLT crates online (six), and the number of events passed from the EVB to the TLT (*Valid_Level_3_Events*). Rejected spark events are indicated by *Number_of_Spark_Events*, beam-gas events by *BG_Events*, and cosmics by *No_of_Mu*. The number of events accepted by the TLT after physics filters, includ-

ing pass-through events, is indicated by *No_of_Events_Accepted*. At the bottom of the display are the online fit results for the z-vertex of events passing one or more physics filters (see Figure 3-10).

3.5.8 The Offline Checks

Extensive monitoring and redundancy checks are performed. The cut values used by the veto algorithms and physics filters are written into the "begin of run event" for each run, which can be retrieved by an offline analysis program. Also added to the data stream are the reconstructed calorimeter energies and times, the reconstructed CTD track and vertex parameters, the energy and position of electron candidates, and two bits for each filter. The first bit is set if an event passes a given filter, and the second bit is set if the event also satisfies the filter prescale.

The performance of the TLT filters is periodically monitored by the trigger group. The information from the TLT filter summary page, Figure 3-13, is available for all 1994 luminosity runs, both in printed and machine-readable form.

The entire TLT filter code can be run offline (TLTZGANA). This code is used to verify online trigger decisions, develop and tune physics filters, and to calculate the trigger acceptance with Monte Carlo data (see Section 6.2.2).


```
********** TLT Run Summary ***************                Run Number =
10009

Run_Start_Time:   Oct 10 22:59:48    Run_Stop_Time:   Oct 11 04:02:06


Crates online                 6    Run_Config                  physics
cpu time (in ms)      294600240    No_of_Empty_Evb_Buffer         1839
Run Status                  618    Run Number                    10009
No_of_Waiting_Msgs       141113    No_Of_IO_Errors                   2
Valid_Level_3_Event      573925    Invalid_Level_3_Event             0
No_of_Events_Accepted    157458    No_of_Events_Rejected        416467
No_Of_Test_Triggers         455    No_Of_Env_Records              1083
No_of_TLT_Thru_Events      1155    No_of_GSLT_Thru_Events        10243
No_of_Spark_Events          602    BG_Events (Time,old)          15162
No_of_VTX_Filter_Events    2828    BG_Events (Time,Straub)       52695
No_of_Mu (Cosmic+Halo)    22804    Sampling_Filter_Events         2105
No_of_HAD_Filter_Events       0    No_of_EPP_Filter_Events       37351
No_of_DIS_Filter_Events   44470    No_of_HPP_Filter_Events       25111
No_of_EXO_Filter_Events   23490    No_of_MUO_Filter_Events        7897
No_of_HFL_Filter_Events   55806    No_of_Filter_Accepts         144736
No_of_Other_Events       336587    No_of_Events_to_ISM          157458

-------------------------------------------------------------------------
CS TIMES (ns): Proton =   0.1        Electron =   0.1

FILTER % VERTEX DISTRIBUTION (GAUSSIAN FIT)

AVG =    3.0 SIGMA = 10.8 CHI2 = ****** Count = *****
-------------------------------------------------------------------------
```

Figure 3-15 *A sample online TLT run summary from a 1994 luminosity run.*

Chapter 4

Kinematics, Simulation, and Reconstruction

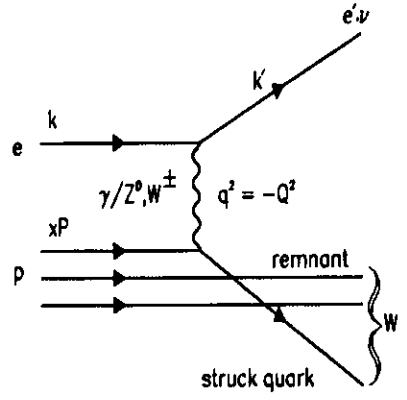

Figure 4-1 *Schematic diagram for electron-proton scattering.*

4.1 The Kinematics of Electron-Proton Scattering

The leading order diagram for deep-inelastic electron-proton scattering (DIS) is shown in Figure 4-1. The scattering is viewed as the interaction of a vector boson emitted by the electron, with a parton (q, $\bar{q}$ or g) in the proton. Neutral current DIS refers to γ or Z^0 exchange, while charged-current DIS refers to $W^{\pm}$ exchange. The

partonic final state in DIS contains the scattered quark and a spectator proton remnant (diquark). For unpolarized electrons, the scattering can be described by the following independent variables:

k, k'	Four-momentum of the initial, final lepton
P	Four-momentum of the proton
$q = (k - k')$	Four-momentum of the virtual boson
E, E'	Energy of the initial, final lepton
θ_e	Polar angle of the final lepton
E_p	Energy of the initial proton
W	Mass of the hadronic system

The four-momentum transfer squared is:

$$Q^2 = -q^2 = -(k - k')^2 \tag{4-1}$$

while the ep centre-of-mass energy squared is:

$$s = (k + P)^2. \tag{4-2}$$

which is 300.4 GeV for HERA (Equation (2-1)). The invariant mass of the hadronic system is given by:

$$W^2 = (P + q)^2. \tag{4-3}$$

At HERA, W extends up to the full centre-of-mass energy, depending upon the four-momentum transfer of an event. The inelasticity parameter y, which is proportional to the energy loss of the incoming electron in the proton rest frame, is:

$$y = \frac{(P \cdot q)}{(k \cdot P)} \tag{4-4}$$

The variable x, which is the fraction of the proton momentum P carried by the struck parton [63] is:

$$x = \frac{Q^2}{2(P \cdot q)} \tag{4-5}$$

The variables y and Q^2 can be calculated from the measured energy E_e and angle θ_e of the scattered electron, from [64]:

$$y_e = 1 - \frac{E'_e}{2E_e}(1 - \cos\theta_e) \tag{4-6}$$

$$Q^2_e = 2E_e E'_e(1 + \cos\theta_e). \tag{4-7}$$

In the analysis in this thesis, events are identified as neutral-current DIS if an electron finder (see Section 3.5.6) reconstructs an electron candidate with $y_e < 0.7$. Events with a larger value of y_e have a scattered electron energy of 5 GeV or less, and the current jet in the event is in the direction of the scattered electron. The jet leads to an increase in the hadronic energy deposits near the electron, and reduces the efficiency of the electron finder to 50% or less [65]. The variable x can be calculated from the relation:

$$Q^2 \cong xys \tag{4-8}$$

An alternative to the electron method is to reconstruct y and Q^2 from the hadronic system, using the method of Jacquet-Blondel [66]:

$$y_{JB} = \frac{\sum_i (E_i - p_{zi})}{2E_e} \tag{4-9}$$

$$Q^2_{JB} = \frac{\left(\sum_i p_{xi}\right)^2 + \left(\sum_i p_{yi}\right)^2}{1 - y_{JB}} \tag{4-10}$$

where the sum is made over all hadrons in the event, having four-vectors $(E_i, p_{xi}, p_{yi}, p_{zi})$. The analysis in this thesis relies on the Jacquet-Blondel method to calculate the hadronic centre-of-mass energy, W (see Section 4.3). Events with $Q^2 < 4$ GeV^2 correspond to the scattered electron escaping undetected down the RCAL beam-hole, and are dominated by photoproduction ($Q^2 \approx 0$).

In the analysis in this thesis, photoproduction and DIS events are combined into one sample in order to study hadronization in ep collisions. This combination is justified by the property of *factorization*, which asserts that processes ocurring at the hadronization scale are independent of the Q^2 of the initial interaction.

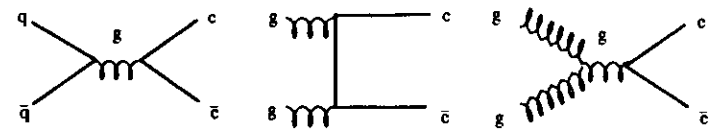

Figure 4-2 *Resolved photon contributions to charm production.*

4.2 Event Simulation

Electron-proton collisions are simulated with a Monte Carlo program [67]. The name Monte Carlo refers to the "random" nature of the simulation, since it involves pseudo-random sampling of a large phase space, such as a multi-dimensional integral, which may be intractable using standard numerical integration.

The analysis in this thesis makes use of the PYTHIA 5.7 [68] Monte Carlo event generator, interfaced to the JETSET 7.4 [69] program, which simulates hadronization using the LUND string model (see Section 1.3.3). The PYTHIA generator simulates charm production based on QCD calculations to first-order in α_s, also referred to as leading-order or LO. In ep collisions, the LO QCD process for charm production is photon-gluon fusion to a $c\bar{c}$ pair (see Section 1.5.1). The Monte Carlo also includes the *resolved photon* [70] processes, which are $O(\alpha\alpha_s^2)$. Although the photon is the pointlike gauge boson of electromagnetism, it also has a probability of coupling to a $q\bar{q}$ pair which can interact strongly with a parton in the proton. These interactions include the processes $q + \bar{q} \to c\bar{c}$ and $g + g \to c\bar{c}$, as illustrated in Figure 4-2. The first diagram shows a quark from the $q\bar{q}$ pair interacting with an antiquark from the proton, while the second and third show a gluon radiated by the $q\bar{q}$ pair interacting with a gluon from the proton. These processes are referred to as *hard subprocesses*, because they are calculable in perturbative QCD due to the scale set by the mass of the charm-quark. The default scale used by PYTHIA to calculate the amplitudes for these processes is $Q^2 = m_c^2 + p_\perp^2$, where m_c is the charm mass, set to 1.5 GeV, and $p_\perp$ is the transverse-momentum of the c quarks.

The cross-section σ for the production of two partons, kl, in an ep collision with $Q^2_e \approx 0$ is calculated as [71]:

$$\sigma_{ep \to kl} = \iiint dx_1 dx_2 d\hat{t}\, f_{i/e}(x_1, Q^2)\, f_{j/p}(x_2, Q^2) \frac{d\hat{\sigma}_{ij \to kl}}{d\hat{t}} \tag{4-11}$$

where a parton i from the photon with momentum fraction x_1 interacts with a parton j from the proton with momentum fraction x_2. The term $\hat{\sigma}_{ij\to kl}$ is the cross-section for the hard subprocess, and is described in terms of the kinematic variable:

$$\hat{t} = (p_i - p_j)^2 = (p_k - p_j)^2. \quad (4\text{-}12)$$

The probability of finding a given parton j in the proton with momentum fraction x is parameterized by a *parton distribution* [63], this is indicated by the term $f_{j/p}(x_2, Q^2)$. These distributions are determined from fits to data measured at a given Q_0^2, and are evolved to the Q^2 scale of the interaction using the Altarelli-Parisi equations [72]. A parton distribution for the photon is included, $f_{i/\gamma}(x_1, Q^2)$, which gives the probability of the electron radiating a photon which subsequently interacts through the processes described above. In the analysis in this thesis, the event simulation makes use of the MRSG [73] structure function for the proton and the GRVHO [74] structure function for the photon.

Higher-order corrections in α_s to the initial and final states are made in PYTHIA and JETSET using the parton shower approach (see Section 1.3).

To simulate the detector response, events are passed through a detector Monte Carlo MOZART [75], which is based on the GEANT [76] routines. The trigger is simulated with the CZAR [77] program. The mass production of events using the PYTHIA, MOZART, and CZAR programs is achieved using the FUNNEL [77] system.

4.3 The Calorimeter Reconstruction

To measure the energy of particles passing through the uranium calorimeter, one relies on the fact that the charge deposited in the left and right PMT's of each calorimeter cell is directly proportional to the deposited energy, and the calibration of this has been determined from test beams [78]. Offline, corrections are applied to the calculated energy, including detector effects from cracks and spaces, non-linearities in PMT response, PMT gain corrections determined by monitoring the UNO, and corrections for out-of-time signals such as cosmics [79].

Calorimeter cell noise, primarily due to uranium radioactivity, is suppressed by a cut at about four times the RMS of the noise signal. This corresponds to a cut of 60 MeV for EMC cells and 110 MeV for HAC cells. In 1994, the RMS width of the noise signal for several PMT's worsened, possibly due to defective PMT's, signal pileup, or miscalibration [80]. To remove these cells, a tighter cut is made at 80 MeV for isolated EMC cells and 120 MeV for isolated HAC cells. Because usually only one

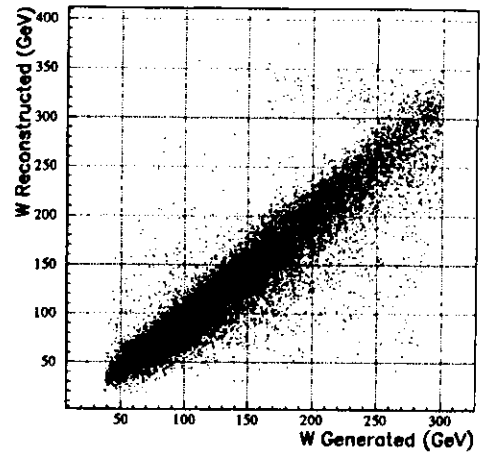

Figure 4-3 *The correlation between the generated and reconstructed hadronic centre-of-mass energy W.*

of two PMT's in a given cell is noisy, cells with an energy imbalance (Equation (3-5)) of 0.7 or greater and energy less than 700 MeV are also suppressed.

An overall energy scale correction is applied to the data, according to studies of effects such as inactive detector material [81]. The correction applied is +6% to BCAL cell energies and +2.5% to RCAL cell energies. Global energy sums in the calorimeter are calculated by summing the energy four-vectors of each cell, defined with respect to the nominal interaction point (see Section 2.2). If the event has a reconstructed CTD vertex (see Section 4.4.2), the cell positions are recalculated with respect to this vertex.

An important quantity derived from the calorimeter energy measurement is the hadronic centre-of-mass energy W, (Equation (4-3)), which may be calculated as:

$$W = \sqrt{m_p^2 + 2(P\cdot q) + q^2}$$

$$\cong \sqrt{2(P\cdot q) - Q^2} \cong \sqrt{ys - Q^2}$$

$$\cong \sqrt{2E_p(E-P_z)_{hadrons} - Q_e^2} \quad (4\text{-}13)$$

where Equation (4-9) and Equation (2-1) have been used. The sum is taken over all cells not associated with a scattered electron, with four-momentum squared Q_e^2. To correct for energy losses in inactive material in the detector, W_{corr} is recalculated as:

$$W_{corr} = (W - (10.4 \pm 0.3)) / (0.802 \pm 0.002) \quad (4\text{-}14)$$

This correction function has been determined from a comparison of the reconstructed and generated W from Monte Carlo simulation. The correlation between the reconstructed W_{corr} after correction and the generated value is shown in Figure 4-3.

Another important quantity is the transverse energy of an event (see Section 5.1.3), defined as:

$$E_T = \sqrt{\sum_{cells} (p_x^2 + p_y^2)} \quad (4\text{-}15)$$

where p_x and p_y are the x and y component of the four-vector of each calorimeter cell, and the sum is taken over all cells. Similarly, the "missing" transverse energy, characteristic of charged-current events, is calculated as:

$$E_T^{miss} = \sqrt{\left(\sum_{cells} p_x\right)^2 + \left(\sum_{cells} p_y\right)^2} \quad (4\text{-}16)$$

This quantity is used in the FLT selection, described in Section 5.1.1.

4.4 Track Reconstruction

Reconstruction of particle trajectories in the tracking detectors is performed using the VCTRAK [54] package. Although VCTRAK uses data from the CTD, VXD, RTD, and SRTD, the analysis in this thesis makes use of only the CTD and VXD.

Tracks are reconstructed first in two dimensions, (x,y), and then continued to three dimensions using z-by-timing and z-by-stereo information from the CTD. Track candidates begin as a *seed* in an outer layer of the CTD, and are followed inward to the origin at $x = y = 0$. A seed consists of three CTD hits from an axial superlayer. To aid in guiding the hit inwards, a fourth "virtual hit" is added at the beam line. The track candidate is extrapolated inward, gathering additional hits with increasing precision. Normally 85% of a candidate's hits must be unique to it, unless a track spans at least two axial superlayers and all shared hits are in the outer layer.

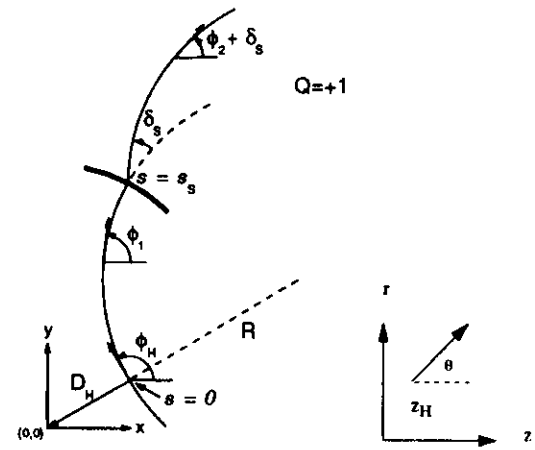

Figure 4-4 *The track helix parameters. In this example the track has a positive charge Q, radius R, and is located a distance D_H from the reference point at (x,y) = (0,0) at angle ϕ_H. It is located at z_H in the (z,r) plane at an angle* θ.

4.4.1 The Track fit

Following pattern recognition, a 5-parameter helix model is fitted to a track candidate, as shown in Figure 4-4. The parameters are measured with respect to a reference point in the (x,y) plane, chosen to be (0,0). The helix parameters are: ϕ_H, the tangent angle to the helix; Q/R, the signed curvature, where Q is the charge and R the helix radius; QD_H, the signed distance from the origin to the reference point on the helix; z_H, the z-coordinate of the reference point on the helix; and cot θ, where θ is the tangent angle to the helix in the (z,r) plane. In addition, a sixth parameter δ is included to account for scattering between the VXD and CTD.

A comparison of the reconstructed momentum of the track to the true momentum for Monte Carlo data (see Section 6.2.4) is given in Figure 4-5. In this case, events are generated to simulate a typical three-body decay, $D_s^+ \rightarrow \phi\pi^+$, (see Section 5.5), and then passed through the detector simulation. The momenta of the reconstructed tracks are summed to give the total momentum, which is plotted on the y-axis. The x-axis gives the generated momentum of the initial particle. This indicates a good correlation over all momenta generated. The scattered points at mo-

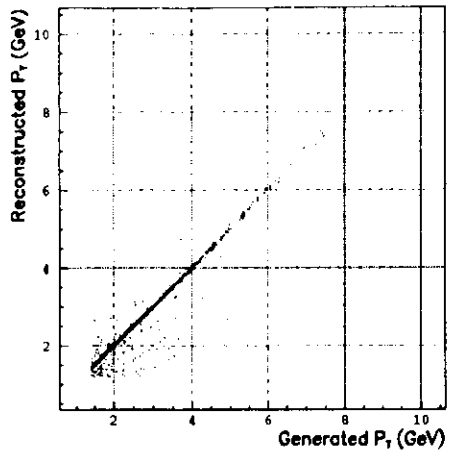

Figure 4-5 *The correlation between the generated and reconstructed track transverse-momenta.*

menta around 2 GeV are background due to the selection of wrong track combinations.

Often the angular coordinate of a reconstructed track is expressed in terms of its *pseudorapidity*, defined to be

$$\eta = -\log\left(\tan\frac{\theta}{2}\right) \tag{4-17}$$

where θ is the polar angle. To be well-reconstructed in the CTD, a track must lie within $-1.75 < \eta < 1.75$.

4.4.2 Vertex finding

Vertex finding is performed in a three-stage process: track filtering, to remove tracks incompatible with the beam line; a simple vertex fit, which calculates the weighted *(x,y,z)* of the remaining tracks; and a full vertex fit, in which the direction and curvature of the tracks are adjusted to the final vertex position. To guide the fit to the origin, a space point at the beam position in the *(x,y)* plane is included in both vertex fits, with $\sigma_z = \sigma_y = 0.7$ cm.

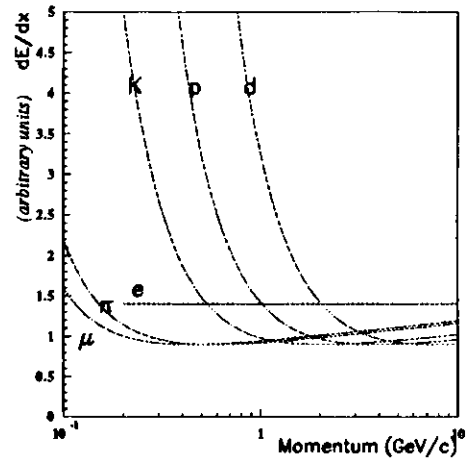

Figure 4-6 *The theoretical ionization energy loss (dE/dx) versus particle momentum for pions, muons, electrons, kaons, protons, and deuterons in the ZEUS CTD gas.*

4.5 Particle Identification

The CTD is instrumented with FADC in order to measure the ionization loss of particles. The pulse height information is used in determining the likelihood of a track being an electron, muon, pion, kaon, proton, or deuteron. The pulse-height data are a measurement of the ionization energy loss of a particle in the chamber gas. For a particle with mass $m > m_e$, the ionization energy loss is described by the Bethe-Bloch equation:

$$-\frac{dE}{dx} = 4\pi N_A r_e^2 m_e c^2 z^2 \frac{Z}{A\beta^2}\left[ln\frac{2m_e c^2\beta^2\gamma^2}{I^2} - \beta^2 - \frac{\delta}{2}\right] \tag{4-18}$$

which holds for a particle of charge ze passing through a material with atomic number Z and atomic weight A. Here m_e is the electron mass, r_e the classical electron radius, the product $4\pi N_A r_e^2 m_e c^2$ is equal to 0.307075 MeV $g^{-1}cm^2$ for A = 1 g mol^{-1} and I is the mean excitation energy for the material.

The energy loss is a function of the particle's velocity: $\beta = \frac{v}{c}$. As the momentum increases from near zero, the energy loss falls as $1/\beta^2$ until about $\beta\gamma \sim 3$, at which point the ionization minimum is reached [82]. As β continues to increase, the term containing $ln\,(\beta^2\gamma^2)$ begins to dominate and the energy loss rises, this is referred to as the region of relativistic rise. For larger momenta, $\beta\gamma \sim 10$, polarization of the medium results in electric screening effects, and causes the energy loss to level off; this is known as the Fermi plateau. This is reflected in the factor $\delta/2$, and is dependent on the density of the medium. Energy loss curves for common particle species in the gas of the CTD are given in Figure 4-6. The dE/dx values are normalized to the pion-band minimum ionization value, and the electron is approximated as a straight line. For example, dE/dx allows for pion/kaon separation for momenta $p < 1$ GeV/c and $p > 2$ GeV/c.

4.5.1 dE/dx Reconstruction

Corrections are applied to the CTD FADC pulse height information of a track to determine its dE/dx. These corrections include the path length of the track, the wire-by-wire gain, the angle between the track and the drift direction (ψ'), and the z-position of the track.

The energy loss of a particle in a thin absorber, or a gas, involves a small number of collisions, with the possibility of a large energy transfer in a single collision [83]. The probability distribution follows a *Landau* curve, as shown in Figure 4-7. In this case the most probable energy loss corresponds to the peak of the distribution, but the mean is shifted to a higher value due to the long tail. Rather than taking the average of all the pulse heights of a track, a *truncated mean* of the pulse heights is calculated. This is achieved by rejecting the 30% highest pulse heights, as well as the lowest 10%.

Variations in temperature and atmospheric pressure, as well as wire voltage, can introduce a run-by-run variation in dE/dx. To correct for these effects, the dE/dx values are normalized to the value of minimum ionization of the pion band. The dE/dx measurements for tracks with momentum $0.3 < p < 0.4$ GeV are fitted to a Gaussian with varying mean, width, and normalization. A Gaussian is a good approximation to the distributions when only the points near the peak are included in the fit. The fitted means of the pion band obtained for the 1994 data are shown in Figure 4-8, for both electron and positron runs. A large jump in values is apparent in this plot, corresponding to a change in the CTD high voltage setting.

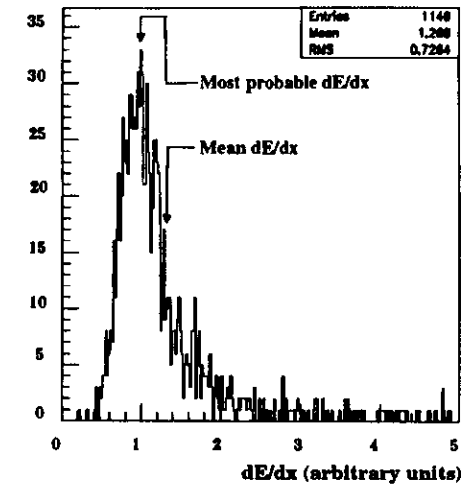

Figure 4-7 *A sample Landau distribution from the CTD pulse height data.*

The dE/dx values decrease as a function of polar angle from $\cos\theta = \pm 1$ to $\cos\theta = 0$, because of a space charge effect. Tracks travelling nearly perpendicular to a wire result in a smaller region of charge collection on the wire. The higher concentration of avalanche electrons around the wire reduces the electric field, so that further electrons are not collected. This results in a lower pulse-height. Figure 4-9 (a) illustrates this angular dependence, and a straight-line fit the data in region $0 < \cos\theta < 0.8$, gives the correction function:

$$\left(\frac{dE}{dx}\right)_{corrected} = \left(\frac{dE/dx}{(1.0 + 0.14|\cos\theta|)}\right) \qquad (4\text{-}10)$$

where the correction is symmetric in $\cos\theta$. The effect of this correction is shown in Figure 4-9 (b). As the angle of a reconstructed track increases from $\cos(\theta) \cong 0.8$ to $\cos(\theta) = 1$, the fraction of hits in a reconstructed track which have a saturated pulse height increases, due to the increase in path length. Since the reconstruction algorithm does not apply corrections to saturated hits, once the percentage of saturated hits exceeds 30% the truncated mean is affected. Possible solutions include

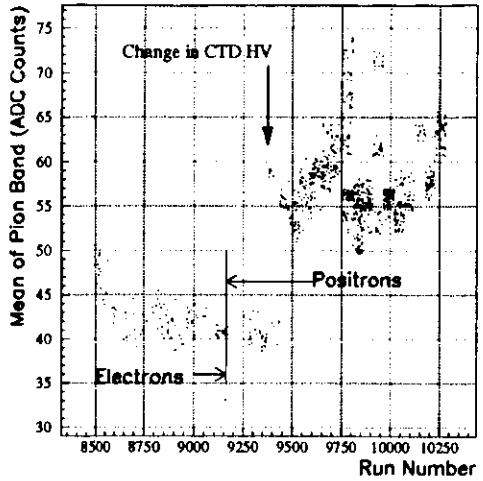

Figure 4-8 *The dE/dx correction factors for 1994 ZEUS CTD data.*

calculating the median of pules heights for tracks with over 30% of the hits saturated, or removing such tracks with a cut on the polar angle.

4.5.2 The Likelihood Method for Particle Identification

To maximize the use of information from dE/dx measurements, and to increase the available statistics, a *likelihood method* of particle identification is used. This method, outlined below, is superior to simple cuts on fixed values. For example, a simple cut on the measured dE/dx of a reconstructed track might be $dE/dx > 2, p < 0.6$ GeV, which could be used to isolate a region of K^+ in Figure 4-6. However, this cut reduces the statistics by removing higher momentum tracks. Furthermore, such a cut does not take into account fluctuations in the dE/dx measurement.

The likelihood that an observed particle corresponds to a given mass hypothesis m is:

$$P_m = \frac{N_m exp(-\chi^2_m/2)}{\Sigma_i N_i exp(-\chi^2_m/2)} \qquad (4\text{-}20)$$

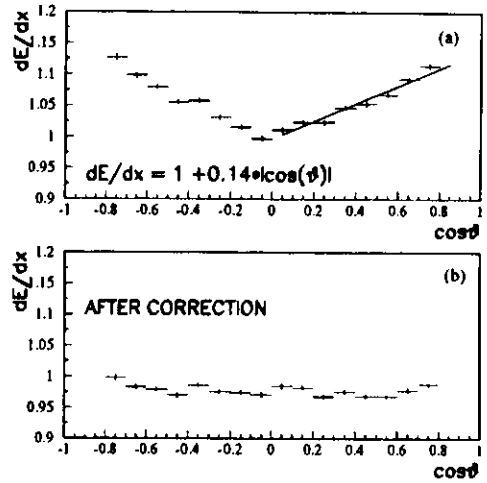

Figure 4-9 *The dE/dx correction as a function of polar angle θ. The function determined from a fit to (a) is applied to the data in (b).*

where the sum is taken over the particle assignments: $(i = e, \mu, \pi, K, p, d)$. The relative particle abundances N_i are taken to be unity (a more sophisticated analysis would calculate the relative abundances, although this is a small correction). The χ^2_i for each mass assignment is calculated from the equation:

$$\chi^2_i = \frac{\left[\left(\frac{dE}{dx}\right)_{measured} - \left(\frac{dE}{dx}\right)_{theory}\right]^2}{\sigma^2_{measured} + \sigma^2_{theory}} \qquad (4\text{-}21)$$

where the measured dE/dx is the reconstructed value for a track, and the theoretical dE/dx is the predicted value from the Bethe-Bloch curve given the track momentum and mass m_i. The σ_{theory} is the error in the theoretical dE/dx due to the uncertainty in the momentum measurement. The $\sigma_{measured}$ is determined from the resolution in the data as follows.

Tracks with momenta from 0.25 to 0.35 GeV are selected and the dE/dx measurements in this interval plotted; this is similar to the method used to determine the correction factors from the pion band. Plots of dE/dx versus the number of hits

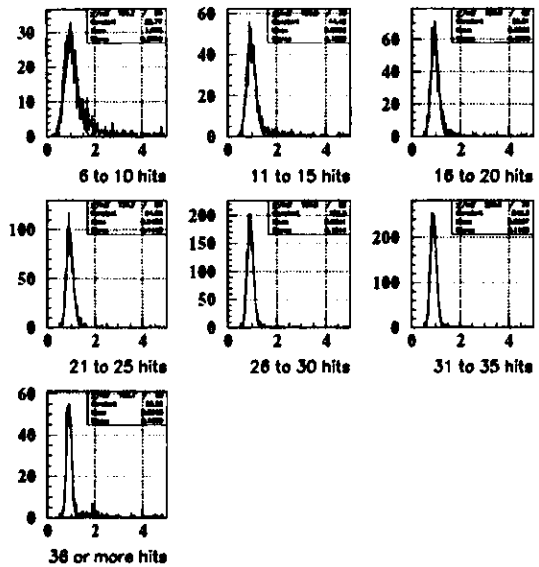

Figure 4-10 *The measurements used to determine the CTD dE/dx resolution in 1994 data.*

n after truncation are shown in Figure 4-10, in bins of five hits. The distribution around the peak in each plot may be approximated by a Gaussian. The σ of a Gaussian fitted to the peak gives the dE/dx resolution, defined as $\sigma_{resolution} = \sigma/\mu$, where μ is the fitted mean. The dE/dx resolution for the 1994 data in bins of hits after truncation is plotted in Figure 4-11. It is of the expected form, $a/\sqrt{n} \oplus b$, where the addition is in quadrature. A fit to the distribution of Figure 4-11 gives:

$$\left[\frac{\sigma(dE/dx)}{dE/dx}\right]_{data} = \sqrt{\frac{(0.67 \pm 0.02)^2}{n} + (0.05 \pm 0.01)^2} \qquad (4\text{-}22)$$

When the same procedure is applied to Monte Carlo data, the result is shown in Figure 4-12. The fitted resolution is:

$$\left[\frac{\sigma(dE/dx)}{dE/dx}\right]_{MC} = \sqrt{\frac{(0.49 \pm 0.03)^2}{n} + (0.0)^2} \qquad (4\text{-}23)$$

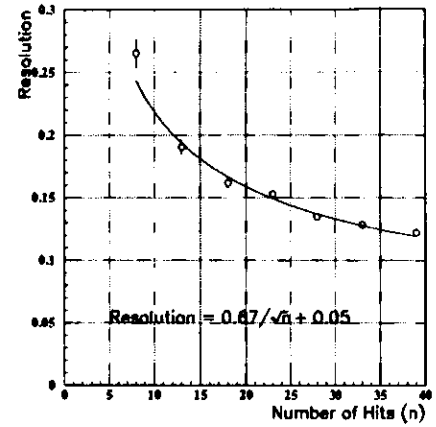

Figure 4-11 *The CTD dE/dx Resolution versus number of track hits after truncation for the 1994 data.*

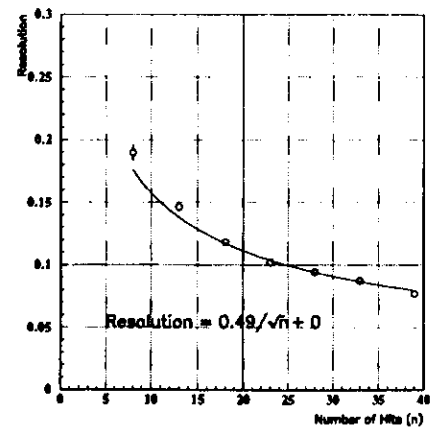

Figure 4-12 *The CTD dE/dx Resolution versus number of track hits after truncation for Monte Carlo data.*

When calculating a mass likelihood for a reconstructed track, Equation (4-23) is used when analyzing Monte Carlo data and Equation (4-22) is used for real data.

4.5.3 Applications of Particle Identification

An example of the likelihood method in identifying $K^{\pm}$ is shown in Figure 4-13. The first plot shows the dE/dx versus momentum from the 1994 data. The $\pi^{\pm}$, $K^{\pm}$, $(\bar{p})$ bands are clearly visible, as well as an electron band (see below). The second plot gives the kaon likelihood distribution (K_{LH}). The third distribution corresponds to selecting the likelihood $K_{LH} > 1\%$. This distribution shows a clear separation of $K^{\pm}$ from the other bands.

A practical application of the likelihood cut is given in Figure 4-14. The first plot shows the invariant mass spectrum of opposite-sign track pairs. The second shows the same spectrum where the likelihood of the tracks being $K^{\pm}$ is required to be $K_{LH} > 90\%$. A clear ϕ signal is evident.

A further utility of dE/dx is the identification of electrons and positrons. In Figure 4-15, a 'zoom-in' view of the dE/dx bands is provided, for the momentum range $0.2 < p < 0.35 GeV$. A clear electron band is seen. This is also visible in the second plot, which shows the pion peak and a smaller electron shoulder. Electron identification by dE/dx is used in a ZEUS analysis to reconstruct the decay $J/\psi \rightarrow e^+e^-$ [62].

The analysis in this thesis makes use of particle identification in reconstructing charm hadron decays from $\pi^{\pm}$, $K^{\pm}$, $(\bar{p})$ candidates (see Chapter 5).

4.6 The Fragmentation Parameter

The fragmentation parameter z, from Equation (1-18) and Section 1.5.2, is defined for a particle M produced in ep collisions to be:

$$z = \frac{p \cdot p_M}{p \cdot q} \qquad (4\text{-}24)$$

where p_M is the four-vector of the particle. Experimentally, this quantity is:

$$z = \frac{(E - p_z)_M}{(E - p)_\gamma} \cong \frac{(E - p_z)_M}{(E - p_z)_{cal} - (E - p_z)_{e'}} \qquad (4\text{-}25)$$

where the numerator is calculated from the reconstructed tracks of the particle, and the denominator is calculated from the calorimeter reconstruction, including an algorithm to identify the contribution from the scattered electron (e') (Section 6.2).

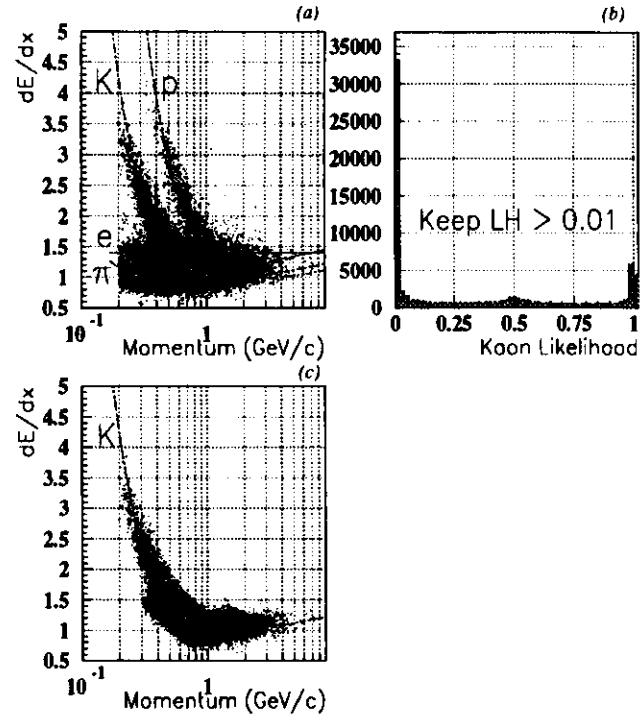

Figure 4-13 *Charged kaon candidates identified using dE/dx and the likelihood method.*

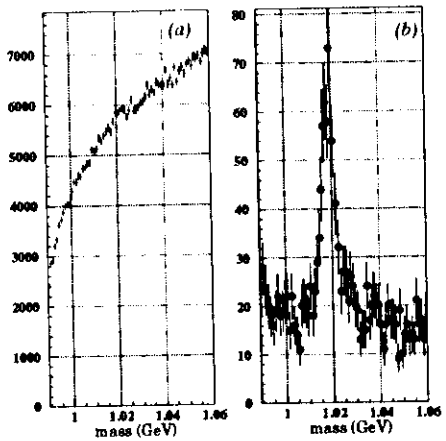

Figure 4-14 *Reconstructing the decay of the ϕ by identifying kaons with dE/dx and the likelihood method.*

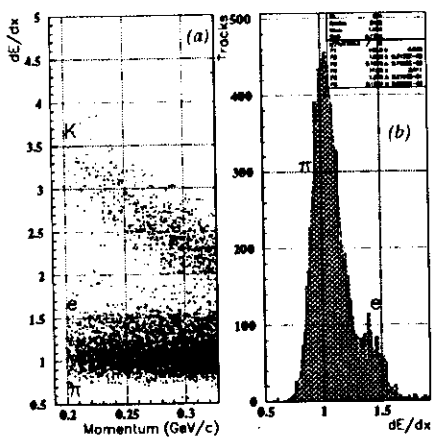

Figure 4-15 *Electrons (and positrons) identified by dE/dx.*

Chapter 5

Observation of Charmed Hadrons

5.1 The Event Selection

Events are selected in which the following charmed hadrons, and their charge-conjugates, are produced:

$$D^0 = c\bar{u} \tag{5-1}$$

$$D^+ = c\bar{d} \tag{5-2}$$

$$D_s^+ = c\bar{s} \tag{5-3}$$

$$\Lambda_c^+ = udc \tag{5-4}$$

These represent all of the lightest charmed mesons and the lightest charmed baryon. Offline, these hadrons are identified by reconstructing the tracks of their decay products and calculating invariant mass distributions. Online, however, the triggers rely on the calorimeter energy deposits of the particles in each event, and on the reconstructed track momenta and the event vertex position. Charmed hadrons are searched for both in photoproduction events, $Q^2 \approx 0$, in which the scattered electron is not detected in the main calorimeter, and in DIS events. Triggers are chosen which select both classes of events.

5.1.1 The First Level Trigger Selection

To select both photoproduction and DIS events, two of the GFLT triggers are selected. The first is *FLT 43*, which uses reconstructed tracks from the CTD-FLT (see Section 3.2) and global energy sums from the CAL-FLT (see Section 3.2).

The CTD-FLT classifies an event based on the total number of reconstructed tracks in an event which intersect the primary interaction region. In 1994 the CTD-FLT event classes were 0 (*reject*), 1 (*unknown*), 2 (*good track*), and 3 (*very good track*). If an event has 2 or more reconstructed tracks and satisfies n(vertex tracks)$/n$(total tracks) > 0.41, then the event class is 3. If at least one reconstructed track intersects the nominal z-vertex, the event class is 2. Class 0 events have at least one reconstructed track but none which point to the vertex, and the remaining events are class 1. FLT 43 requires that an event be class 2 or class 3.

Along with the requirement on reconstructed-tracks, FLT 43 includes five *subtriggers* on global energy sums. These subtriggers are illustrated in Figure 5-1, which shows (z,r) sections of the ZEUS calorimeter (see Section 2.2). The nominal interaction point for ep collisions is indicated by an X, and produced particles are drawn as lines originating from this point. The first subtrigger requires a minimum energy deposit in the calorimeter, $E_{CAL}^{FLT} > 15$ GeV. For this calculation, the inner three rings of towers around the forward beampipe, and the inner ring of towers around the rear beampipe, are excluded. This suppresses the contribution from beam-gas events, which typically have low p_T and energy deposits concentrated around the beampipe regions. The second subtrigger detects the electromagnetic shower of a scattered electron in the BCAL, by requiring an electromagnetic energy deposit $E_{BEMC}^{FLT} > 3.4$ GeV. The third subtrigger demands a large missing transverse energy $E_{Tmiss}^{FLT} > 12$ GeV; this is characteristic of a charged-current event $ep \rightarrow \nu X$ in which the ν escapes undetected. The fourth subtrigger selects events in which the electron scatters in the RCAL direction. This subtrigger demands that the electromagnetic energy deposit in the RCAL EMC be $E_{REMC}^{FLT} > 2$ GeV, again excluding the inner ring of towers to suppress the contribution from beam-gas events which occur upstream of the detector. The fifth subtrigger searches for events with a medium to high energy scattered electron, by summing the energy deposits in all the electromagnetic sections of the calorimeter, excluding the F/RCAL beampipe regions, and requires that $E_{EMC}^{FLT} > 10$ GeV.

The second FLT slot used is *FLT 30*, which is designed specifically to select DIS events in which the electron scatters in the RCAL direction. This relies on an electron-finding algorithm, which searches for an electromagnetic shower in the RCAL by making cuts on the isolation of energy deposits and on the ratio of EMC to HAC energy.

For both FLT 30 and 43, a cut is made on the timing information of the C5 detector, the Vetowall, and the SRTD (see Section 2.2). These cuts select ep events,

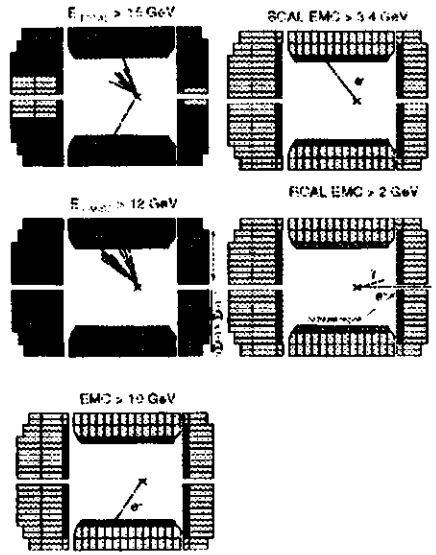

Figure 5-1 *Schematic of FLT subtriggers. The darkened areas indicate the regions active in each subtrigger.*

originating from the nominal interaction region, and suppress beam gas events which originate outside this region (see Section 3.5.3).

5.1.2 The Second Level Trigger Selection

At the GSLT empty triggers and sparks are removed (see Section 3.3). Beam-gas and cosmics are rejected by calorimeter timing cuts. In addition, events with $(E-p_z)^{SLT}_{CAL} > 75$ GeV are vetoed, as this is above the maximum value for ep events (see Figure 5-2 (b)), taking into account the calorimeter energy resolution.

To select charm production at the GSLT, two triggers are used. The first is *SLT HFL 03* which makes three requirements on the CAL-SLT global energy sums. The first cut is on the ratio of longitudinal energy to total energy (P_z/E); distributions for this quantity are plotted in Figure 5-2 (a). In this figure, background data from the TLT Sampling filter are shown as points, while D_s Monte Carlo data are plotted as a line histogram, and the data are normalized to the number of Monte

Carlo events. The data are a mixture of a small number of charm production events combined with a large sample of non-charm events, and so can be considered to be mostly background. The data exhibit an excess over the Monte Carlo near $(P_z/E) \approx 1$; to reduce the rate from these events a cut is made of $(P_z/E)^{SLT}_{CAL} < 0.94$.

The second requirement of SLT HFL 03 is based on the $(E-p_z)$ of the event. As shown in Figure 5-2 (b), the distribution in this quantity from D_s Monte Carlo exhibits two features: a peak near 50 GeV; and a peak near zero. The first peak results from events in which the scattered electron is detected in the main calorimeter, resulting in an $(E-p_z)$ of twice the incident electron beam energy. The second feature is a falling distribution peaked near zero; this is from photoproduction events in which the scattered electron escapes through the RCAL beam pipe hole. Data from the TLT Sampling filter are superimposed as solid points. To reduce the contribution of beam-gas and low-energy photoproduction, a cut is made of $(E-p_z)^{SLT}_{CAL} > 4$ GeV, which corresponds to a minimum W, from Equation (4-13), of about 80 GeV.

The third requirement for SLT HFL 03 is that the BCAL and RCAL EMC energy sum satisfies $E^{SLT}_{BEMC} + E^{SLT}_{REMC} > 2$ GeV; this is used to tag either the electromagnetic shower from an electron scattered in the BCAL or RCAL, or the decay products of photoproduction events.

The second SLT trigger used is *SLT DIS 01*, which selects events in which the scattered electron showers in the EMC section of the calorimeter. The trigger requires that one of the following subtriggers be satisfied: $E^{SLT}_{REMC} > 2.5$ GeV or $E^{SLT}_{BEMC} > 2.5$ GeV or $E^{SLT}_{FEMC} > 10$ GeV or $E^{SLT}_{FHAC} > 10$ GeV. To suppress the contribution from photoproduction, a cut is made of $(E-p_z)^{SLT}_{CAL} + 2(E_{LUMI_\gamma}) > 24$ GeV. The inclusion of the energy measured in the LUMI-γ tagger keeps events in which a photon is radiated in the initial state and is detected by the luminosity monitor.

5.1.3 The Third Level Trigger Selection

At the TLT, three filters are used to identify charm production. These filters rely on the fact that charmed hadrons produce decay products with relatively high transverse momenta compared to the background of mostly low-momenta pions. The first two filters exploit the TLT track reconstruction, and demand that the reconstructed tracks are fitted to a common vertex. This requirement reduces the combinatorial background which would occur if all reconstructed tracks are used.

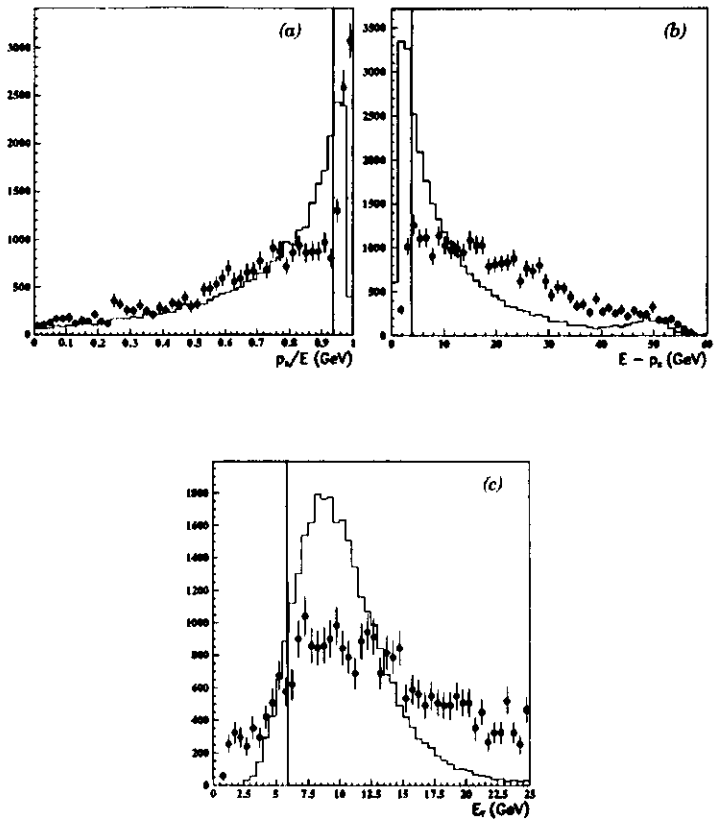

Figure 5-2 *Global energy sum distributions for data (points) from the TLT sampling filter and Monte Carlo (line histograms). The vertical axis gives the number of events, while cut values are indicated by vertical lines.*

The first TLT filter is *DST 22: Heavy Flavour Charm Filter*. Because hadronic charm decays typically produce two or more high-p_T oppositely charged particles, this filter demands that at least two tracks are reconstructed with opposite charge, each having $p_T > 0.4$ GeV. To be well-reconstructed in the CTD, both track candidates must lie within the polar angle $15° < \theta < 165°$.

Charm production typically involves a hard initial interaction; this is reflected in the transverse energy spectrum of the event. As shown in Figure 5-2 (c), charm Monte Carlo events, plotted as a line histogram, have a higher minimum E_T than the sampling filter data, shown as solid points. A cut is made in this filter at $E_T > 6$ GeV. In addition, the cut made at the SLT on (P_z/E) is tightened to $(P_z/E)_{CAL} < 0.9$.

Because the output rate of DST 22 is $O(1)$ Hz, which approaches the allowed TLT limit for each of the physics groups, it is prescaled by a factor 5. However, the effective prescale is closer to 1, because the majority of events which satisfy this filter but which are prescaled, are selected by another TLT filter. This increases the overall statistics, but also complicates the acceptance calculation.

The second TLT filter used is *DST 28: Heavy Flavour $b\bar{b}$ Filter*. This filter requires that two opposite-sign tracks are reconstructed, each with $p_T > 0.5$ GeV. Their combined momentum sum must satisfy $p_T^+ + p_T^- > 2.0$ GeV. Typically, beam-gas events deposit most of their energy in the forward region, and this can be suppressed by making an angular cut. The transverse energy outside a 10° cone around the FCAL beampipe is denoted by the variable $E_T^{10°}$. Charm events are selected by DST 28 if they satisfy $E_T^{10°} > 12$ GeV. This filter is not prescaled.

Both filters demand that the event vertex be $|z_{vertex}| < 75$ cm (Figure 3-10), this removes beam-gas events not rejected by calorimeter timing.

To select DIS events, the trigger used is *DST 11: Nominal DIS*. This filter is designed to select events in which the scattered electron is detected in the main calorimeter, based on one of three selection criteria. The first requirement is that the energy measured in the inner ring of towers of the electromagnetic section of the RCAL be $E_{REMC}^{beampipe} > 6$ GeV or that the energy in the region outside the beampipe be $E_{REMC}^{nonbeampipe} > 4$ GeV, or the energy in the BCAL EMC be $E_{BEMC} > 4$ GeV. The second requirement is that the event satisfy $(E - p_z)_{CAL} + 2(E_{LUMI_T}) > 25$ GeV, and $(E - p_z)_{CAL} < 100$ GeV. The third requirement is that one of two electron finder algorithms identify an electron in the main calorimeter, having a reconstructed energy of $E_e > 4$ GeV (see also Section 3.5.6).

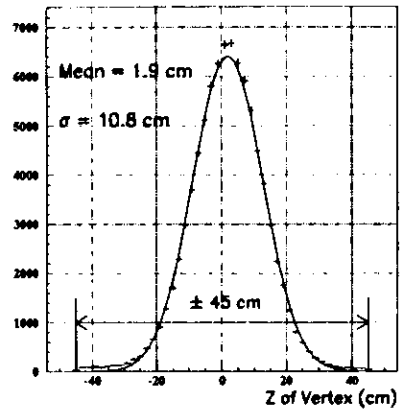

Figure 5-3 *The 1994 vertex distribution for ZEUS events after DST selection.*

Selection	Events Remaining
Events on Disk	14,264,539
DST Bits Selection	5,252,149
Require Vertex	5,114,109
Cut |z-vertex| < 45 cm	4,790,465
Reconstruct 2 or more tracks	4,767,906
Fit 2 or more tracks to vertex	4,746,047

Table 5-1 *Offline preselection cuts.*

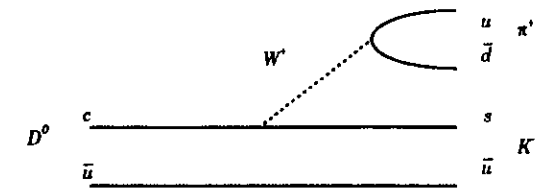

Figure 5-4 *Schematic of the decay $D^0 \rightarrow K^-\pi^+$.*

5.1.4 The Offline Preselection

Offline, to remove residual beam-gas events, a tighter z-vertex cut is made, taking advantage of the full offline VCTRAK reconstruction. The z-vertex distribution for the 1994 data is shown in Figure 5-3. A Gaussian is fitted to the data, with a fitted mean of 1.9 cm, and fitted width of 10.8 cm. Offline a cut is made at $|z_{vertex}| < 45$ cm.

The effect of the preselection cuts on the data is summarized in Table 5-1. Following these cuts, further cuts are made to isolate charmed hadrons in the individual decay channels. For each of these channels, all offline track candidates must have at least two reconstructed track candidates which are fitted to a common vertex. All offline track candidates must lie within $|\eta| < 1.75$, to ensure that they are well-measured.

5.2 Observation of the D^0

The D^0 meson can be identified through the decay channel shown in Figure 5-4:

$$D^0 \rightarrow K^-\pi^+, \quad \overline{D}^0 \rightarrow K^+\pi^- \tag{5-5}$$

This is known as a spectator decay, in which the charm quark emits a virtual W^+, which decays into a $u\bar{d}$ pair, forming a π^+. The $\bar{u}$ quark does not participate in this reaction, but combines with the s quark to form a K^-. The world average branching ratio for this decay process is $3.83 \pm 0.12\%$ [33].

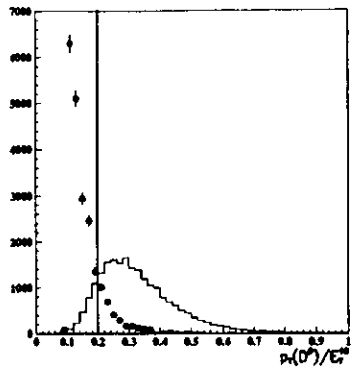

Figure 5-5 *Comparison of data (points) after TLT filters with D^0 Monte Carlo (line histogram). The selection cut is indicated by a vertical line.*

To reconstruct this decay, invariant mass combinations are made for pairs of opposite-sign track candidates. Both π^+ and K^- mass hypotheses are allowed for each track. To reduce the combinatorial background, cuts on the track candidate transverse momentum are made: $p_T(K) > 1.0$ GeV and $p_T(\pi) > 1.0$ GeV. Each track candidate must pass through at least three superlayers of the CTD to remove poorly-reconstructed track candidates. Tracks considered for a K^- mass hypothesis are required to be identified by dE/dx with a likelihood of at least 0.01 (Section 4.5.2). To ensure that the dE/dx resolution is of $O(15\%)$ or better, a minimum of 15 or more hits after truncation is required. Each track combination must also satisfy $p_T(D^0) > 1.4$ GeV.

In addition, a cut is made on the ratio of the transverse momentum of the D^0 to the transverse energy outside the 10-degree forward (FCAL) cone. As shown in Figure 5-5, the sampling filter data, plotted as points, tend to peak towards zero for this ratio, while the D^0 Monte Carlo distribution, shown as a line histogram, is shifted towards higher values. A cut is made at $p_T(D^0)/E_T^{10^\circ} > 0.2$

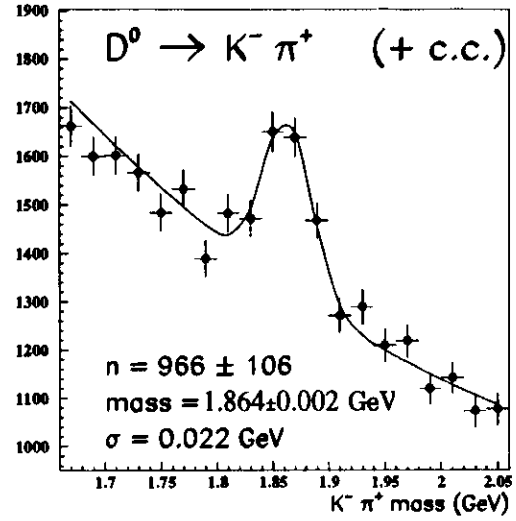

Figure 5-6 *Observation of the D^0, $\overline{D}^0$.*

Using these cuts, the invariant mass distribution shown in Figure 5-6 is obtained. A Gaussian and exponential background are fitted to the data, allowing the mean μ, width σ, and normalization N of the Gaussian to vary:

$$\frac{N}{\sigma\sqrt{2\pi}} exp\left[-\frac{1}{2}\left(\frac{(x-\mu)}{\sigma}\right)^2\right] \qquad (5\text{-}6)$$

Although the background is closer to a polynomial over a large mass region, an exponential is a good approximation to the background in this limited mass window. Note that the plot is zero-suppressed, indicating the high level of combinatorial background still present with these cuts. The fit results give 966 ± 106 $D^0/\overline{D}^0$ candidates, with a fitted mass of 1.864 ± 0.002 GeV. This is in good agreement with the accepted mass of 1.8645 ± 0.0005 GeV [33].

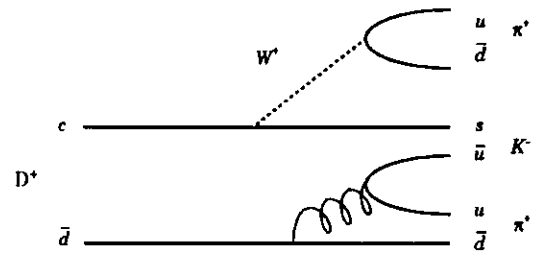

Figure 5-7 *Schematic diagram for the decay* $D^+ \rightarrow K^- \pi^+ \pi^+$.

5.3 Observation of the $D^{\pm}$

From a subset of the 1994 data, the decay:

$$D^{\pm} \rightarrow K^{\mp} \pi^{\pm} \pi^{\pm} \qquad (5\text{-}7)$$

is reconstructed. A schematic for this decay is shown in Figure 5-7. The c quark decays to an s quark by emitting a virtual W^+, which in turn couples to a π^+ in the final state. A $u\bar{u}$ pair tunnels out of the colour field; this process is represented symbolically in the figure by the emission and branching of a gluon. The s and $\bar{u}$ quarks form a K^-, while the remaining u and $\bar{d}$ quarks form a second π^+.

Three-track combinations are taken, with the requirement that each K^- mass hypothesis have a likelihood of 0.01 or higher, and that each track candidate have 15 or more hits after truncation. The allowed charge combinations must correspond to $K^-\pi^+\pi^+$ and $K^+\pi^-\pi^-$ for the D^+ and the D^- respectively. Each track candidate must have a minimum p_T of 0.5 GeV, and each D-meson candidate must satisfy $p_T(D^{\pm}) > 3.0$ GeV. The resulting invariant mass distribution with these cuts is shown in Figure 5-8. A Gaussian signal with varying mean, width, and normalization along with a second order polynomial background are fitted to the data. The fit results give 88±32 candidates, with a measured mass of 1.878 ± 0.004 GeV. This is in reasonable agreement with the accepted mass of 1.8693 ± 0.0005 GeV [33].

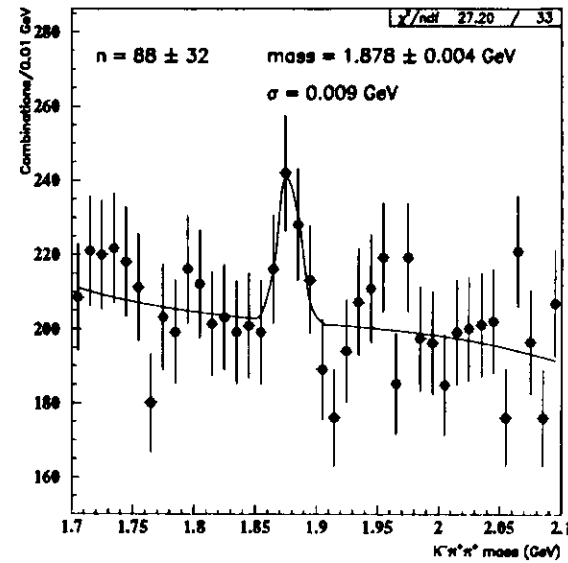

Figure 5-8 *Observation of the decay* $D^{\pm} \rightarrow K^{\mp} \pi^{\pm} \pi^{\pm}$.

This represents the first observation of the $D^{\pm}$ meson in ep collisions. The acceptance of the $D^{\pm}$ is not yet known for ZEUS, and so no cross-section is calculated. With knowledge of the acceptance, and higher statistics, one could determine the cross-section ratio:

$$\frac{\sigma(ep \rightarrow D^{\pm} X)}{\sigma(ep \rightarrow D^0 X)} \qquad (5\text{-}8)$$

which is sensitive to the vector-to-pseudoscalar meson production ratio [32], described in Section 1.3.1.

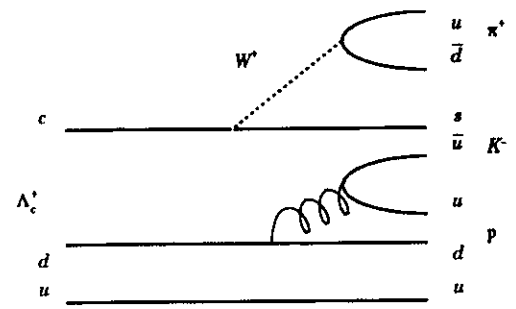

Figure 5-9 *Schematic diagram for the decay* $\Lambda_c^+ \to pK^-\pi^+$.

5.4 Observation of the $\Lambda_c^\pm$

The Λ_c^+ and Λ_c^- are identified via the decays:

$$\Lambda_c^+ \to pK^-\pi^+, \quad \Lambda_c^- \to \bar{p}K^+\pi^-, \tag{5-9}$$

as illustrated in Figure 5-7. The c quark decays to an s quark by emitting a virtual W^+, which couples to a π^+ in the final state. The tunneling of a $u\bar{u}$ pair out of the colour field is shown symbolically by the emission of a gluon. The s and $\bar{u}$ quarks couple to a K^- in the final state, while the two u and d quarks couple to a proton in the final state. The world average branching fraction for this decay is $4.4 \pm 0.6\%$ [33].

To reconstruct this decay, three track combinations are taken, with the charge of the tracks corresponding to p, K^-, π^+, or $\bar{p}K^+\pi^-$ for the charge-conjugate. For every p, K^-, π^+ mass hypothesis, a likelihood assignment of at least 0.1 is required, and each reconstructed track must have 15 or more hits after truncation. Each track must have minimum p_T of 0.5 GeV and lie within $|\eta| < 1.75$. The Λ_c candidates must satisfy $p_T(\Lambda_c) > 1\ GeV$ and $|\eta(\Lambda_c)| < 1.75$. To suppress background, a cut is made on the quantity $(E-p_z)_{\Lambda_c} / (E-p_z)_{CAL} > 0.5$ (see Section), and on $p_T(\Lambda_c)/E_T^{10^\circ} > 0.2$.

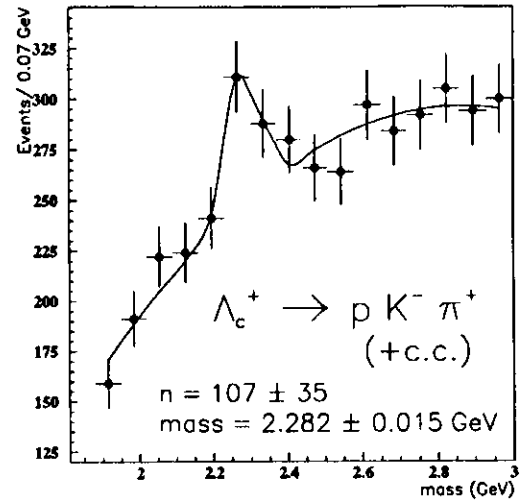

Figure 5-10 *Observation of the* Λ_c.

The resulting mass distribution is shown in Figure 5-10. A Gaussian signal with varying mean, width, and normalization, and a second order polynomial background are fitted to the data. The fit results give a signal of 107 ± 35 candidates, and a fitted mass of 2.282 ± 0.015 GeV. The fitted mass is in agreement with the accepted value of 2.2849 ± 0.0006 GeV [33].

This represents the first observation of charmed baryon production in ep collisions. Previous Monte Carlo studies had predicted that an integrated luminosity of at least 6.1 ± 4.1 pb^{-1} would be required to observe a signal for the Λ_c in ep collisions using this decay channel [84]. However, the technique used to determine this estimate did not fully exploit particle identification.

The acceptance of the Λ_c is not yet known for ZEUS, and so no cross-section is calculated. With knowledge of the acceptance, and higher statistics, one could determine the ratio of charmed baryon to charmed meson production in ep collisions. This would provide information on the probability of producing a baryon in the had-

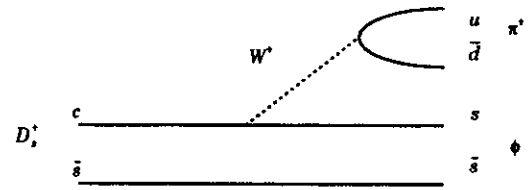

Figure 5-11 *Schematic for the decay* $D_s^+ \rightarrow \phi\pi^+$.

ronization process. For example, one could make a comparison of the cross-section ratio:

$$\frac{\sigma(ep \rightarrow \Lambda_c^- X)}{\sigma(ep \rightarrow D^0 X)} = \frac{\overline{udc}}{c\bar{u}} \qquad (5\text{-}10)$$

which is related to the probability of producing a $\overline{ud}$ anti-diquark compared to a $\bar{u}$ antiquark.

5.5 Observation of the $D_s^{\pm}$

The D_s is identified by its decay:

$$D_s^+ \rightarrow \phi\pi^+ , \qquad (5\text{-}11)$$

as depicted in Figure 5-11. The c quark decays to an s quark by emitting a virtual W^+, which couples to a π^+ in the final state. The $s\bar{s}$ pair form a ϕ meson, which decays predominantly to K^+K^-, with a world average branching fraction $BR(\phi \rightarrow K^+K^-) = (49.1 \pm 0.6)\%$ [33]. The ϕ has a relatively narrow width of $\Gamma = 4.43 \pm 0.05$ MeV [33] compared to other vector mesons such as the ρ. The narrowness is due in part to the low Q-value of about 24 MeV for the decay $\phi \rightarrow K^+K^-$, and also because the decay $\phi \rightarrow \pi^+\pi^-\pi^0$ is Zweig-suppressed, meaning that the decay involves a three-gluon intermediate state.

The decay channel $D_s^+ \rightarrow \phi\pi^+$ is chosen due to its relatively high branching-fraction, with a world average of $BR(D_s^+ \rightarrow \phi\pi^+) = (3.6 \pm 0.9)\%$. Furthermore, misidentified particles from decays such as $D^+ \rightarrow K^-\pi^+\pi^+$ and $\Lambda_c^+ \rightarrow pK^-\pi^+$ can cause

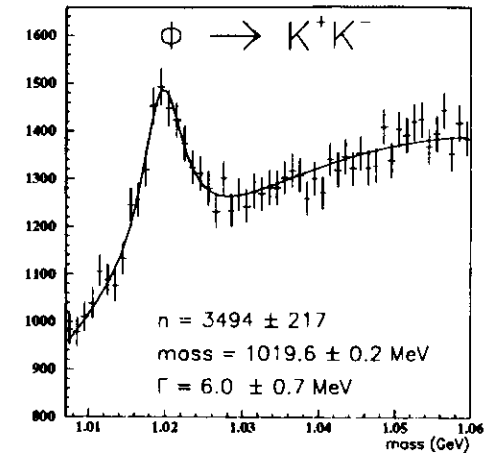

Figure 5-12 K^+K^- *Invariant Mass Distribution.*

the D^+ and Λ_c to fake a signal in the D_s mass region; this is referred to as a *reflection*. The contributions from other decay modes are greatly reduced by cutting near the mass of the ϕ resonance.

5.5.1 Reconstruction of the Decay $\phi \rightarrow K^+K^-$

To reconstruct the ϕ, pairs of oppositely-charged tracks are selected which are consistent with coming from a common vertex, have a minimum K likelihood assignment of 0.01, and have $p_T > 0.2$. The resulting invariant mass spectrum is shown in Figure 5-12. Because the reconstructed mass resolution and intrinsic width of the ϕ are comparable in magnitude, a Breit-Wigner line shape and a second-order polynomial background are fitted to the data. The fit yields 3494 ± 217 candidates at a measured mass of 1019.6 ± 0.2 MeV. The fitted mass is in good agreement with the accepted value of 1019.413 ± 0.008 MeV [33].

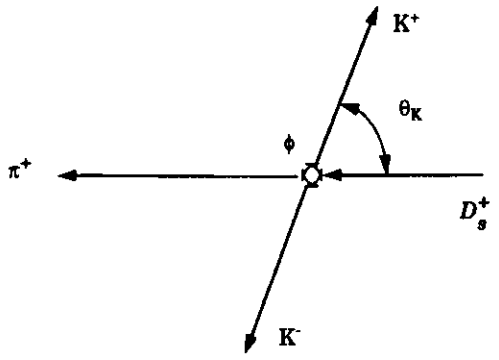

Figure 5-13 *Schematic for the angle* $\cos\theta_K$ *in the decay* $D_s^+ \to \phi\pi^+$.

5.5.2 Reconstruction of the Decay $D_s^\pm \to \phi\,\pi^\pm$

The decay $D_s^\pm \to \phi\pi^\pm$ is reconstructed by selecting K^+K^- candidates within ±10 MeV of the nominal ϕ mass; the fit results indicate that this cut retains approximately 86% of the ϕ signal. These candidates are combined with all remaining tracks having $p_T > 0.3$ GeV. In addition, each D_s candidate must have $p_T(D_s) > 1.2$ GeV and $p_T(D_s)/E_T^{10} > 0.08$, (see Section 5.2).

A further cut is made on the helicity angle, $\cos\theta_K$, of the K^+ in the ϕ rest frame with respect to the $\pi^\pm$ direction (see Figure 5-13). Since the decay is from a pseudoscalar particle $J^P(D_s) = 0^-$ to a vector $J^P(\phi) = 1^-$ and pseudoscalar $J^P(\pi) = 0^-$, the decay angle of either kaon with respect to the $\pi^\pm$ direction is expected to behave as $\cos^2\theta_K$. This behaviour is in contrast to the background distribution, which is constant in $\cos\theta_K$. A cut is made at $|\cos\theta_K| > 0.3$, which reduces the background by 30% and results in a loss in signal of about 3%.

The resulting invariant mass spectrum is shown in Figure 5-14. A Gaussian signal with variable mean, width, and normalization, and an exponential background are fitted to the data. The fit results give 401 ± 76 candidates with a measured mass of 1.978 ± 0.004 GeV, in reasonable agreement with the accepted value of 1.9685 ± 0.0006 GeV [33].

This is the first observation of the D_s in ep collisions.

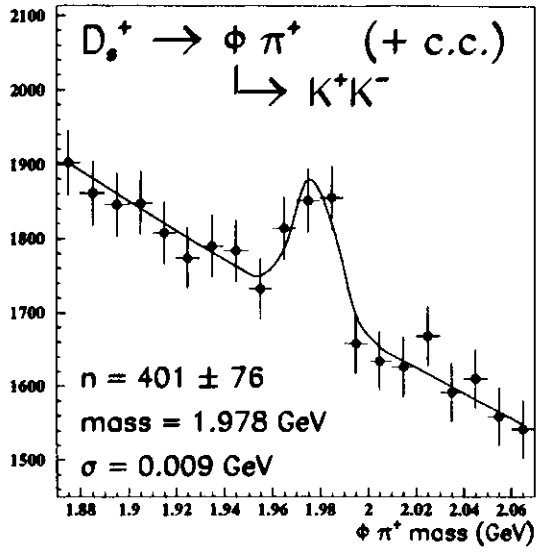

Figure 5-14 *Observation of the* D_s.

Chapter 6

Analysis of Charmed Hadrons

6.1 The Separation of $D^0/\bar{D}^0$ Signals.

An asymmetry in the production rate of the D^0 meson compared to the $\bar{D}^0$ anti-meson can test the predictions of the string model for hadronization, as outlined in Section 1.5.1. Experimentally, the D^0 is identified by the charge of the K^- in the decay $D^0 \to K^-\pi^+$.

From the 966 ± 106 $D^0/\bar{D}^0$ candidates shown in Figure 5-6, the corresponding separation into meson and anti-meson is illustrated in Figure 6-1. In this figure, the D^0 meson combinations are marked by solid points, while the $\bar{D}^0$ anti-meson combinations are marked by open points. A Gaussian with varying mean, width, and normalization, along with an exponential background, are fitted to each set of data, and the fitted curves are superimposed with a solid line for the D^0 combinations and with a dashed line for the $\bar{D}^0$ combinations. The fit results give the number of candidates to be:

$$N(D^0) = 486 \pm 74 \qquad (6\text{-}1)$$

$$N(\bar{D}^0) = 489 \pm 67. \qquad (6\text{-}2)$$

which corresponds to an asymmetry, using Equation (1-34), of $A_{c\bar{c}} = -0.3 \pm 10\%$.

This result may be compared to the PYTHIA Monte Carlo prediction using LUND string hadronization. From a sample of 21584 $ep \to D^0X$ Monte Carlo events, with $p_T(D^0) > 1.4$ GeV, 9945 events are found to contain a D^0 meson at the generator level, while 11639 events are found to contain a $\bar{D}^0$. This separation results in a Monte Carlo prediction of a $D^0/\bar{D}^0$ asymmetry of $A_{c\bar{c}}^{MC} = -7.85 \pm 0.01\%$.

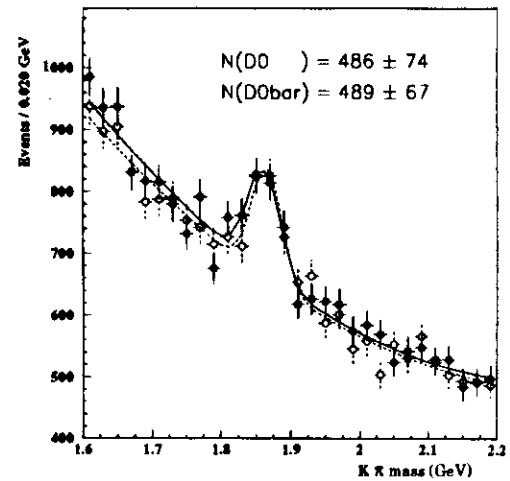

Figure 6-1 *Separation into $D^0, \bar{D}^0$ signals. The dark points represent D^0 combinations, and the dashed points represent $\bar{D}^0$ combinations.*

Checks are made for any bias in the CTD reconstruction of positive and negative track candidates, which might affect the $D^0/\bar{D}^0$ result. Reconstructed track candidates from a sample of 1994 photoproduction data, selected with $(E - p_z) < 30$ GeV, are plotted in Figure 6-2. Negative track candidates are indicated by a solid line, and positive tracks are indicated by a dashed line. The distribution in track hits after truncation is shown in Figure 6-2 (a), which indicates a slight excess in the number of hits assigned to positive tracks compared to negative tracks, for tracks with 36 or more hits after truncation. This asymmetry in the number of hits could arise from the deviation of the Lorentz angle in CTD cells (Section 2.2.1), resulting from the lower-than-design value of the magnetic field of 1.43 T, instead of 1.8 T. However, a reduction in the number of hits for long tracks should not bias the overall asymmetry, because the tracks are still reconstructed, although with fewer hits. The distribution in transverse momentum of positive and negative reconstructed tracks is shown in Figure 6-2 (b), and the charge asymmetry between the positive and negative tracks in Figure 6-2 (c). For reconstructed tracks with $p_T > 1$ GeV, the largest asymmetry observed of negative tracks over positive tracks

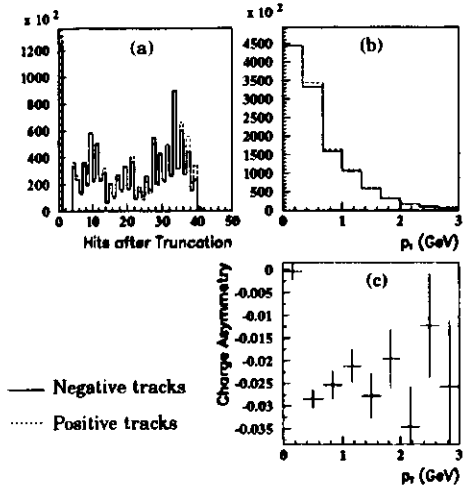

Figure 6-2 *A comparison of positive and negative reconstructed CTD tracks. The vertical axes in (a) and (b) give the number of reconstructed track candidates. The asymmetry between the number of positive and negative reconstructed tracks as a function of transverse momentum is given in (c).*

is approximately -3.5%. The charge asymmetry has been checked using single muon tracks in the CTD [85]; the study concludes that there is no significant bias in the reconstruction of positive over negative tracks.

Previous measurements of the $D^0/\overline{D}^0$ asymmetry include a value of $-2.0 \pm 1.5\%$ from E-687 and a value of $-3.8 \pm 1.5\%$ from E-691, as described in Section 1.5.1.

Within the statistics of the 1994 ZEUS data, the asymmetry for $D^0/\overline{D}^0$ production, in the kinematic range $p_T(D^0) > 1.4$ GeV, is in agreement with the prediction from PYTHIA Monte Carlo using LUND string fragmentation.

6.2 The Ratio of D_s to D^0 Production

The ratio of D_s to D^0 production may be sensitive to the level of strangeness suppression in the hadronization process, as described in Section 1.5.3. The observations of charmed hadrons, in Section 5.5, use all of the available 1994 ZEUS data; however, to measure the D_s to D^0 ratio a restricted sample of the data is chosen. The

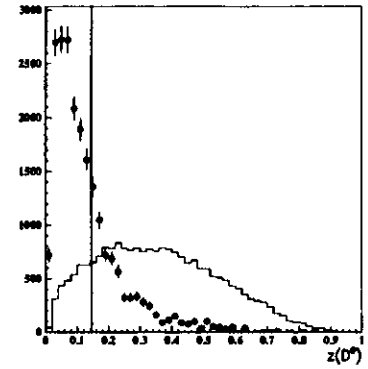

Figure 6-3 *The D^0 fragmentation spectrum in data (points) and Monte Carlo (line histogram).*

restricted sample simplifies the calculation of the acceptance, defined as the number of events from a Monte Carlo sample which are reconstructed after all cuts, divided by the number of events generated in a specific kinematic range. To ensure stable trigger conditions, only the runs with e^+p collisions are taken, as the energy scale of the CAL-FLT in 1994 was uncalibrated before those runs. To simplify the efficiency calculation, the trigger slots are restricted to FLT 43, (Section 5.1.1), SLT HFL 03 (Section 5.1.2), and the TLT Heavy Flavour $b\bar{b}$ Filter (Section 5.1.3). In addition, noisy calorimeter cells are suppressed, as described in Section 4.3.

6.2.1 The Restricted D^0 Sample

To improve the signal-to-noise ratio for the D^0 signal, shown in Figure 5-6, additional kinematic cuts are applied. The fragmentation function of charm quarks is peaked towards higher values of the fragmentation variable z (Section 4.6) than the distribution for lighter quarks (Section 1.5.2). Figure 6-3 shows the distribution in the variable z, from Equation (4-25), for data from the TLT Sampling filter (Section 3.5), plotted as points, compared to D^0 Monte Carlo data, plotted as a line histogram. In this figure the number of events in the data is normalized to the number of Monte Carlo events. The difference in the distributions suggests a cut at $z(D^0) > 0.15$; this is drawn as a vertical line in the figure. In forming $K^-\pi^+$ combinations, the cuts on the transverse momentum of each track are relaxed to be

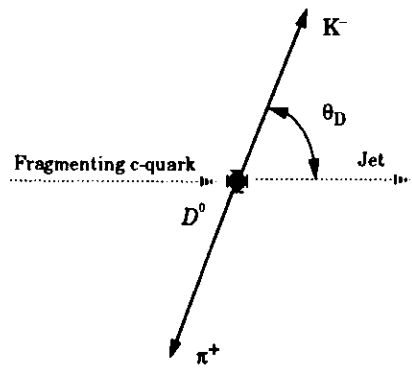

Figure 6-4 *Schematic for the angle θ_D in the decay $D^0 \to K^- \pi^+$, viewed in the D^0 rest frame.*

$p_T(K) > 0.9$ GeV and $p_T(\pi) > 0.9$ GeV, while the cut on $p_T(D^0) > 3.0$ GeV is unchanged. The polar angle of the meson is restricted to the region $-1.5 < \eta(D^0) < 1.0$. The measured hadronic centre-of-mass energy must lie within $100 < W < 300$ GeV; the lower limit is due to FLT acceptance, and the upper value is the kinematic limit.

In the rest frame of the D^0, which is a spin-0 particle, the K^- decays isotropically. If the D^0 is part of a jet from a fragmenting c quark, the jet produces background tracks, mostly pions, which tend to peak at values of $|\cos\theta_D| \approx 1$, where θ_D is the angle between the D^0 boost direction and the K^-. This is illustrated in Figure 6-4. The background is peaked at low angles due to its limited p_T compared to that of the K^- and π^+ [86]. A cut at $|\cos\theta_D| < 0.3$ significantly reduces the background.

The selection for the restricted D^0 signal is summarized in Table 6-1. The resulting signal with these cuts is shown in Figure 6-5. A Gaussian signal, having varying mean, width, and normalization, along with a second order polynomial background, are fitted to the data. The fit results give 344 ± 46 candidates having a

FLT 43, SLT HFL03, TLT $b\bar{b}$
$100 < W < 300$
$p_T(D^0) > 3.0$ GeV
$-1.5 < \eta(D^0) < 1.0$
$p_T(K) > 0.9$ GeV
$p_T(\pi) > 0.9$ GeV
$z(D^0) > 0.15$
$p_T(D^0)/E_T^{10^\circ} > 0.2$
$\lvert\cos\theta_D\rvert < 0.3$

Table 6-1 *Summary of the restricted cuts for the D^0.*

fitted mass of 1.851 ± 0.004 GeV, and a fitted width of 0.028 ± 0.003 GeV.

6.2.2 The D^0 Acceptance

To calculate the ZEUS acceptance for the reconstruction of the decays $D^0 \to K^-\pi^+$, $\bar{D}^0 \to K^+\pi^-$, a sample of 21584 $ep \to D^0X$ Monte Carlo events was generated with $p_T(D^0) > 1.4$ GeV. Of these events, 1937 correspond to the kinematic range $p_T(D^0) > 3.0$ GeV, $-1.5 < \eta(D^0) < 1.0$, and $100 < W < 300$ GeV. The full sample of events was passed through the ZEUS detector and trigger simulation, and the cuts described in Section were applied. The resulting signal is shown in Figure 6-6. A Gaussian with varying normalization, mean, and width, and a second-order polynomial background are fitted to the data, giving a fitted mass of 1.861 ± 0.003 GeV and a fitted width of 0.028 ± 0.003 GeV. The mass and width from the Monte Carlo data are in good agreement with the values obtained from the data in Section . The fitted number of Monte Carlo events is 182 ± 15. From the generated number of events in the kinematic range described above, the acceptance is determined to be:

$$Acc(D^0) = 0.0940 \pm 0.0076. \qquad (6\text{-}2)$$

This acceptance is used in the calculation of the cross section in Section 6.2.5.

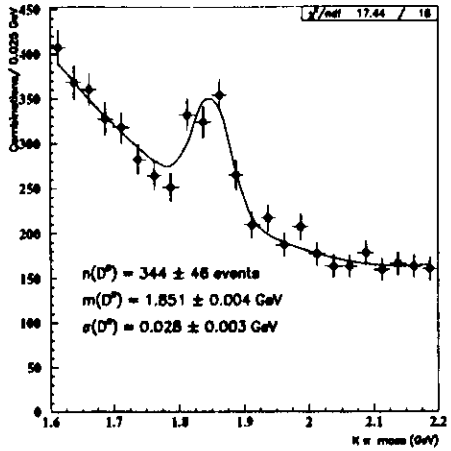

Figure 6-5 *The D^0 signal in data with restricted cuts.*

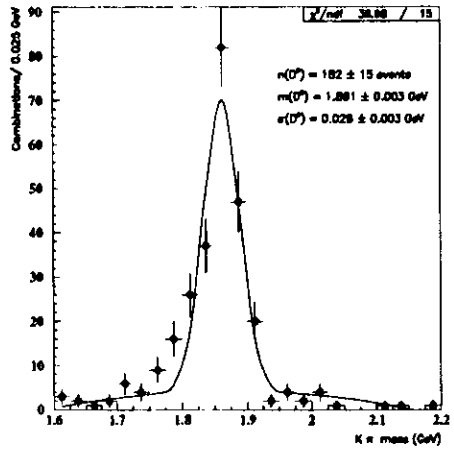

Figure 6-6 *The D^0 Monte Carlo signal after restricted cuts.*

6.2.3 The Restricted D_s Sample

The decay $D_s^{\pm} \rightarrow \phi\pi^{\pm}$ is reconstructed using the same procedure in Section 5.5.2, but the kinematic range is restricted to that used in Section for the D^0 sample. In summary, these cuts are $p_T(D_s) > 3.0$ GeV, $p_T(D_s)/E_T^{10^\circ} > 0.2$, $z(D_s) > 0.15$, and $-1.5 < \eta(D_s) < 1.0$. The track candidates must satisfy $p_T(K) > 0.5$ GeV and $p_T(\pi) > 0.3$ GeV, and the ϕ mass cut of 1.01 GeV < mass (ϕ) < 1.03 GeV is applied. The cut on the helicity angle of the K^- (Section 5.5.2) is tightened to $|\cos\theta_K| > 0.531$; this reduces the background by approximately 53% while reducing the signal by about 15%.

The resulting signal for the D_s is given in Figure 6-7. A Gaussian and second order polynomial are fitted to the data. The fit results give 45 ± 15 candidates, with a fitted mass of 1.961 ± 0.006 GeV, and fitted width of 0.014 ± 0.004 GeV.

6.2.4 The D_s Acceptance

To calculate the ZEUS acceptance for the reconstruction of $ep \rightarrow D_s^{\pm} X$, a sample of 28441 D_s Monte Carlo events was generated, of which 2475 events correspond to the kinematic range $100 < W < 300$ GeV, $p_T(D_s) > 3.0$ GeV, and $-1.5 < \eta(D_s) < 1.0$. The full sample of events was passed through the ZEUS detector and trigger simulation. After application of the cuts described in Section 6.2.3, the invariant mass distribution is for the surviving events is shown in Figure 6-8. A Gaussian and second order polynomial background are fitted to the Monte Carlo data.

The fit results give a fitted mass of 1.968 ± 0.001 GeV and fitted width of 0.012 ± 0.001 GeV. The mass and width from the Monte Carlo data are in good agreement with the results obtained from the data in Section 6.2.3. The fitted number of Monte Carlo events is 183 ± 14. From the generated number of Monte Carlo events, the acceptance is calculated to be:

$$Acc(D_s) = 0.0738 \pm 0.0058 \tag{6-4}$$

6.2.5 The Cross Sections for D_s and D^0 Production

To calculate a cross-section σ for a given process, one uses the formula:

$$\sigma = \frac{N}{\mathcal{L} \times BR \times Acc} \tag{6-5}$$

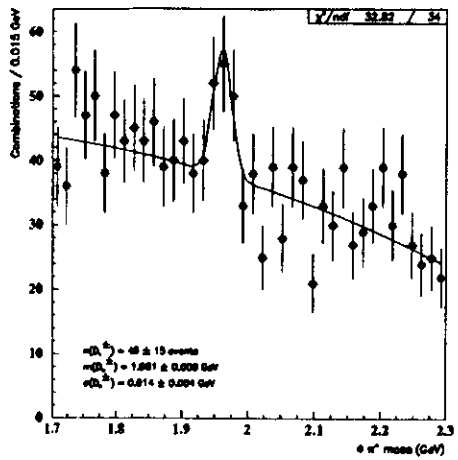

Figure 6-7 *The D_s signal in data with restricted cuts.*

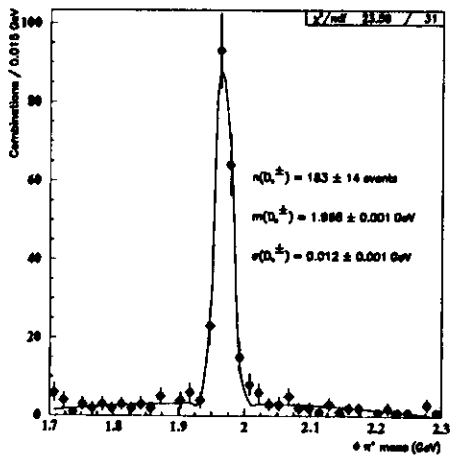

Figure 6-8 *The D_s Monte Carlo sample after restricted cuts.*

Reconstructed events $D_s^{\pm} \rightarrow \phi\pi^{\pm}$	45 ± 15
Acceptance $acc\,(D_s)$	0.0738 ± 0.0058
BR($D_s^{\pm} \rightarrow \phi\pi^{\pm}$)	$3.6 \pm 0.9\%$
BR($\phi \rightarrow K^+K^-$)	$49.1 \pm 0.6\%$
Cross Section for $ep \rightarrow D_s^{\pm} X$	11.5 ± 4.0 nb

Table 6-2 *Determination of the cross-sections for D_s production.*

Reconstructed events $D^0 \rightarrow K^-\pi^+$	344 ± 46
Acceptance $acc\,(D^0)$	0.0940 ± 0.0076
BR($D^0 \rightarrow K^-\pi^+$)	$3.83 \pm 0.12\%$
Cross Section for $ep \rightarrow D^0 X$	31.9 ± 5.0 nb

Table 6-3 *Determination of the cross-sections for D^0 production.*

where N is the number of events observed, $\mathcal{L}$ is the luminosity, BR is the branching ratio of the decay process studied, and Acc is the acceptance. In this analysis, the luminosity corresponds to the "1994 ZEUS e^+p nominal vertex data" listed in Table 2-1, which is 2.989 ± 0.045 nb^{-1}. Using the D^0 and D_s signals measured in Section and Section 6.2.3, the acceptances calculated in Section 6.2.2 and Section 6.2.4, the cross sections for the process $ep \rightarrow D^0X$ in the kinematic range $p_T(D) > 3.0$GeV, $100 < W < 300$, $-1.5 < \eta(D) < 1.0$ is determined to be 31.9 ± 5.0 nb. For the process $ep \rightarrow D_s^{\pm} X$ in the same kinematic range, the cross section is calculated to be 11.5 ± 4.0 nb. These calculations are summarized in Table 6-3 and Table 6-2. The quoted error of these cross sections is statistical only; the systematic errors are determined in Section 6.2.6.

6.2.6 The Systematic Errors for D_s and D^0 Production Cross Sections

Systematic errors in a cross-section measurement arise from the uncertainties in the luminosity measurement, in the relevant branching ratios, and in the acceptance. To determine the uncertainty in the acceptance for the D_s and the D^0, a series of systematic checks is made.

The uncertainty in the absolute calorimeter energy scale is approximately ±3%. To simulate this effect, the energy scale is varied in Monte Carlo data by ±3%, and the acceptance for the D^0 and the D_s is recalculated.

There is an uncertainty in the Monte Carlo modelling of the energy flow in the fragmentation region of the proton remnant. An excess of deposited energy is observed in the forward region in data compared to Monte Carlo data [87], and this can affect the efficiency of the cut on the variable $E_T^{10^\circ}$. To check this effect, the cut on $p_T(D)/E_T^{10^\circ} > 0.2$ is varied by its estimated resolution of ±2%, in both data and Monte Carlo data, and the analysis repeated. The change in the number of D^0 and D_s candidates is determined as a ratio of events in data compared to events in Monte Carlo data.

To verify that the dependence of the D_s acceptance on the ϕ mass cut in data is reproduced by Monte Carlo, the cut of 1.01 GeV < mass (ϕ) < 1.03 GeV is varied by ±1MeV. The change in number of D_s candidates is computed as a ratio of events in data compared to events in Monte Carlo data.

The uncertainty in the magnetic field measurement is estimated to be less than 1%. The error on the luminosity measurement is 1%. The uncertainty in the branching ratio of $D_s^+ \rightarrow \phi\pi^+$ is ±25%. The uncertainty in the branching ratio of $\phi \rightarrow K^+K^-$ is ±1.2%, and the uncertainty in the branching ratio of $D^0 \rightarrow K^-\pi^+$ is ±3.1%.

The contributions to the systematic error are summarized in Table 6-4. Including the systematic error calculation, the cross-sections become:

$$\sigma(ep \rightarrow D_s^+ X) = 11.5 \pm 4.0\ (\text{stat}) \pm 3.4\ (\text{syst})\ \text{nb} \qquad (6\text{-}6)$$

$$\sigma(ep \rightarrow D^0 X) = 31.9 \pm 5.0\ (\text{stat}) \pm 5.4\ (\text{syst})\ \text{nb} \qquad (6\text{-}7)$$

From these measurements the production ratio of D_s to D^0 is determined to be:

$$\frac{\sigma(ep \rightarrow D_s^+ X)}{\sigma(ep \rightarrow D^0 X)} = 0.36 \pm 0.14\ (\text{stat}) \pm 0.09\ (\text{syst}) \qquad (6\text{-}8)$$

In calculating this ratio, the correlated systematic errors in Table 6-4 cancel, and only the contributions marked with a "*" are included. This ratio may be compared

Source	Systematic Error	On σ
Calorimeter Energy scale ±3%	±4%	D^0, D_s
Vary cut on $p_T(D)/E_T^{10^\circ} > 0.2$ by ±2%	±16%	D^0, D_s
* Vary cut on m(ϕ) in data and MC by ±1MeV	±1%	D_s
Uncertainty in magnetic field measurement	< 1%	D^0, D_s
* Uncertainty in BR($D_s^+ \rightarrow \phi\pi^+$)	±25%	D_s
* Uncertainty in BR($\phi \rightarrow K^+K^-$)	±1.2%	D_s
* Uncertainty in BR($D^0 \rightarrow K^-\pi^+$)	±3.1%	D^0
Uncertainty in Luminosity Measurement	±1%	D^0, D_s
Total systematic error on $\sigma(D^0)$	±16.8%	D^0
Total systematic error on $\sigma(D_s)$	±30.0%	D_s
* Total systematic error for ratio D_s/D^0	±25.2%	D^0, D_s

Table 6-4 *Systematic errors for D^0 and D_s measurements.*

to the Monte Carlo prediction of:

$$\left(\frac{\sigma(ep \rightarrow D_s^+ X)}{\sigma(ep \rightarrow D^0 X)}\right)_{LUNDMC} = 0.220 \pm 0.024 \qquad (6\text{-}9)$$

and the NA14/2 measurement (Section 1.5.3) of:

$$\frac{\sigma(\gamma N \rightarrow D_s^+ X)}{\sigma(\gamma N \rightarrow D^0 X)} = 0.22 \pm 0.07 \pm 0.04 \qquad (6\text{-}10)$$

To extract the value of the strangeness suppression parameter, described in Section 1.5.3, a straight line is fitted to the data from Figure 1-14, resulting in a fitted slope of 0.748 ± 0.037. Using this slope and the ratio in Equation (6-8), the corresponding value of strangeness suppression is:

$$\gamma_s = 0.48 \pm 0.18\ (\text{stat}) \pm 0.12\ (\text{syst}) \qquad (6\text{-}11)$$

Within errors, the value of strangeness suppression obtained is in agreement with the default LUND setting of $\gamma_s = 0.3$. A plot of the ratio of Equation (6-8) and the corresponding value of γ_s from Equation (6-11) is given in Figure 6-9. The

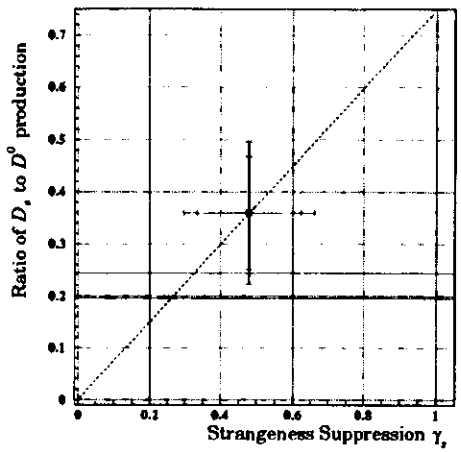

Figure 6-9 *The measured strangeness suppression parameter.*

straight-line fit to Figure 1-14 is plotted as a dashed line, while the predicted ratio of D_s to D^0 production from the LUND model lies within two horizontal solid lines.

6.2.7 Cross Checks on the D_s Production Cross Section

To check the cross section measured for $\sigma(ep \to D_s^{\pm} X)$, a second independent analysis was performed [88]. The same 1994 data sample and kinematic cuts were used. This analysis differs in that no z-vertex cut is applied to the data offline. The analysis also differs in that a limited mass window from 1.88 GeV to 2.1 GeV is used to fit a Gaussian and exponential background to the D_s invariant mass distribution. The resulting cross section from this second analysis is $\sigma(ep \to D_s^{\pm} X) = 13.9 \pm 4.0$ nb, where the error is statistical only. This cross section is in agreement with the value obtained in Section 6.2.5.

6.2.8 The Comparison of D_s and D^0 Data to Monte Carlo

In order to verify that the Monte Carlo provides a good description of the data, a comparison is made in the transverse-energy distribution of the $D \equiv (D^0, D_s)$ candidates. The final sample of D candidates is divided into three bins of p_T, which are $3.0 < p_T(D) < 5.5$ GeV, $5.5 < p_T(D) < 8.0$ GeV, and $8.0 < p_T(D) < 12.0$ GeV. A

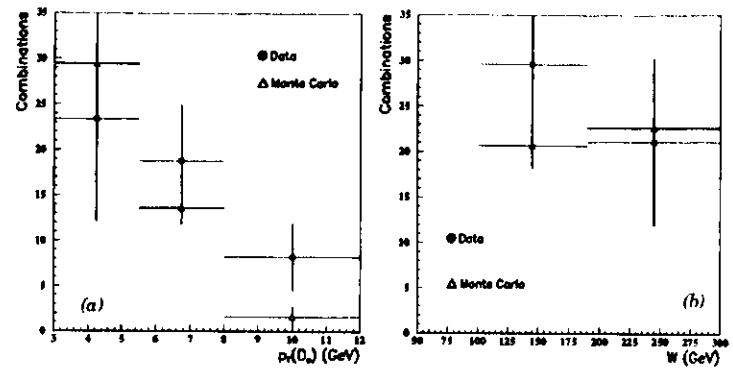

Figure 6-10 *Comparison of D_s candidates in data (solid points) to D_s Monte Carlo data (open triangles).*

Gaussian with a fixed mass and width, and a second order polynomial for the background, are fitted to the data in each momentum bin. The fixed mass and width reduce the statistical error in the fit, and are taken from the fit results in Section 6.2.3. The same procedure is repeated for Monte Carlo data, which were subjected to the full detector and trigger simulation and analysis cuts.

The distribution for the D_s transverse momenta is given in Figure 6-11 (a), in which the Monte Carlo events are normalized to the total events in the data. Data are plotted as solid points, while Monte Carlo data are plotted as open triangles. The corresponding distributions for the D^0 candidates from Section and D^0 Monte Carlo data are given in Figure 6-11 (a). Both figures show a good agreement between the data and Monte Carlo description of the D transverse momentum.

A second comparison is made in the hadronic centre-of-mass variable, W, Equation (4-14), in two bins: $100 < W < 190$ GeV and $190 < W < 300$ GeV. The same fit method used to compare p_T is performed, and the results are given in Figure 6-11 (b) for the D_s and Figure 6-11 (b). for the D^0. Within the statistical errors, the W-distribution in data is well-reproduced by the D Monte Carlo.

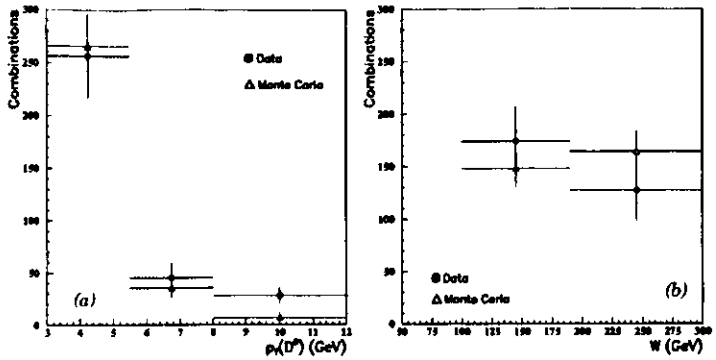

Figure 6-11 *Comparison of D^0 candidates in data (solid points) to D^0 Monte Carlo data (open triangles).*

6.2.9 Comparison with Other Measurements of Strangeness Suppression

In order to compare the measurement of strangeness suppression in *ep* collisions to that of other experiments, the effective centre-of-mass energy, $\sqrt{\hat{s}_{eff}}$, must be estimated (see Section 1.4). For charm production in *ep* collisions, it may be calculated from [89]:

$$\hat{s}_{eff} = \left(\frac{p_T^2 + m_c^2}{z(1-z)}\right) \qquad (6\text{-}12)$$

where p_T is the transverse-momentum of the charm quark or anti-quark, which is approximated by the reconstructed p_T of the charmed meson. The term m_c is the charm quark mass, taken to be 1.5 GeV, and z is the fragmentation variable, described in Section 4.6. From a sample of PYTHIA Monte-Carlo events containing D-mesons with $p_T(D)$>3.0 GeV, the effective centre-of-mass energy is estimated to be 10 ± 4 GeV.

Using this information, the measured strangeness suppression parameter is plotted against $\sqrt{\hat{s}_{eff}}$ in Figure 6-12 (see also Figure 1-11). The value measured in *ep* collisions lies within the range predicted by a logarithmic function of $\sqrt{\hat{s}_{eff}}$ (Equation (1-32)) fitted to the measurements from other experiments.

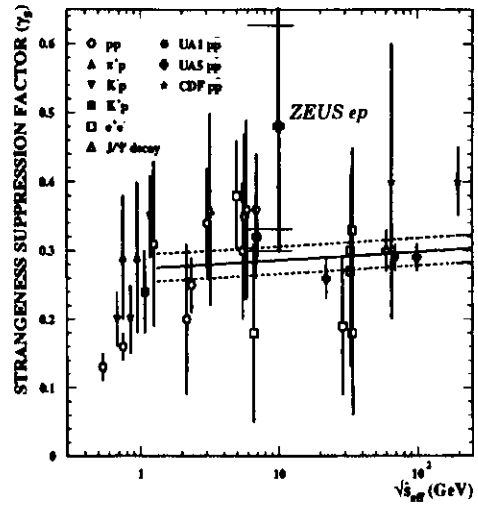

Figure 6-12 *Comparison of the measured strangeness suppression to the results of other experiments.*

6.3 Measurement of the Vector to Pseudoscalar Ratio

As described in Section 1.3.1, the production ratio of vector (spin-1) to pseudoscalar (spin-0) mesons is predicted to be $V/(V+P) = 3/4$. Experimentally, this can be determined by combining information from the ZEUS measurement of the $D^{*\pm}$ meson, which is a charged, spin-1 counterpart to the D^0 meson.

The ZEUS measurement of the process $ep \to D^{*\pm} X$ in photoproduction ($Q^2 < 4$ GeV^2) in the kinematic range $p_T(D^{*\pm}) > 3.0$ GeV, $-1.5 < \eta(D^{*\pm}) < 1.0$, $115 < W < 280$ GeV results in a preliminary cross-section of [90]:

$$\sigma_{PHP}(ep \to D^{*\pm} X) = 11.0 \pm 1.4\,(\text{stat}) \pm 1.0\,(\text{syst})\ \text{nb} \qquad (6\text{-}13)$$

After restricting the sample of D^0 candidates measured in Section 6.2.5 to photoproduction, by removing events with a scattered electron in the final state, the kinematic range: $p_T(D^0) > 3.0$ GeV, $-1.5 < \eta(D^0) < 1.0$, and $115 < W < 280$ GeV is

selected. The result is a sample of 220 ± 37 candidates in the data, with an acceptance of 0.0948 ± 0.0088. This corresponds to a cross-section in photoproduction of:

$$\sigma_{PHP}(ep \to D^0 X) = 20.2 \pm 3.9\ (\text{stat}) \pm 3.4\ (\text{syst})\ \text{nb} \tag{6-14}$$

From the ratio of the two measurements, Equation (6-13) and Equation (6-14), the ratio of $D^{*\pm}$ to D^0 production is:

$$\left(\frac{\sigma(ep \to D^{*\pm} X)}{\sigma(ep \to D^0 X)}\right)_{PHP} = 0.54 \pm 0.12\ (\text{stat}) \pm 0.10\ (\text{syst}) \tag{6-15}$$

This is in good agreement with the observed ratio in e^+e^- [33] of 0.50 ± 0.05, and with a second measurement in ep collisions [91] of 0.41 ± 0.09 ± 0.10.

To convert the result in Equation (6-15) into the vector-to-pseudoscalar ratio, one needs to calculate the term [92]:

$$P_V = \frac{\sigma_{dir}(D^{*+})}{\sigma_{dir}(D^{*+}) + \sigma_{dir}(D^0)} \tag{6-16}$$

Here the terms $\sigma_{dir}(D^{*0})$ and $\sigma_{dir}(D^0)$ refer to the direct production cross-sections from the charm fragmentation process $c \to DX$. To calculate the term $\sigma_{dir}(D^0)$, the contribution of D^0 production from the decay of the D^{*0} must be excluded. In forming this ratio, several assumptions are made. The first assumption is that D^{*0} and $D^{*\pm}$ mesons are produced with equal probability in charm fragmentation. The second assumption is that charm fragmentation is the only mechanism by which D^{*0}'s and D^{*+}'s are produced. The third assumption is that D^0 mesons originate either directly from $c \to D^0 X$ or from decays of the D^{*0} and the $D^{*\pm}$, and there is no contribution from higher spin states. The relevant decays and branching ratios are:

$$D^{*0} \to D^0 X, \quad BR = 100\% \tag{6-17}$$

$$D^{*+} \to D^0 \pi^+, \quad BR = (68.3 \pm 1.4)\% \tag{6-18}$$

With these assumptions, the total number of D^0 mesons produced will be:

$$\begin{aligned}\sigma_{tot}(D^0) &= \sigma_{tot}(D^{*0}) \cdot BR(D^{*0} \to D^0 X) + \sigma_{tot}(D^{*+}) \cdot BR(D^{*+} \to D^0 \pi^+) + \sigma_{dir}(D^0) \\ &= \sigma_{tot}(D^{*+})\,(1 + BR(D^{*+} \to D^0 \pi^+)) + \sigma_{dir}(D^0)\end{aligned} \tag{6-19}$$

This gives the number of D^0 mesons produced directly to be:

$$\sigma_{dir}(D^0) = \sigma_{tot}(D^0) - \sigma_{tot}(D^{*+})\,(1 + BR(D^{*+} \to D^0 \pi^+)) \tag{6-20}$$

and so the ratio becomes:

$$\begin{aligned}P_V &= \frac{\sigma_{tot}(D^{*+})}{\sigma_{tot}(D^{*+}) + \sigma_{tot}(D^0) - \sigma_{tot}(D^{*+})\,(1 + BR(D^{*+} \to D^0 \pi^+))} \\ &= \frac{\sigma_{tot}(D^{*+})}{\sigma_{tot}(D^0) - \sigma_{tot}(D^{*+}) BR(D^{*+} \to D^0 \pi^+)} \\ &= \frac{1}{\dfrac{\sigma_{tot}(D^0)}{\sigma_{tot}(D^{*+})} - BR(D^{*+} \to D^0 \pi^+)}\end{aligned} \tag{6-21}$$

Using the cross-section information given above, this ratio is determined to be:

$$P_V = 0.86 \pm 0.20\ (\text{stat}) \pm 0.11\ (\text{syst}) \tag{6-22}$$

This is in agreement with the value predicted from spin-counting, of 0.75, and the measurements in e^+e^- of 0.71 ± 0.19 by ARGUS [93], of 0.71 ± 0.14 ± 0.12 by CLEO [94] and of 0.686 ± 0.084 ± 0.077 ± 0.0084 by OPAL [92] (where the uncertainty due to branching ratios is indicated by the last term in the OPAL measurement). A compilation of measurements of P_V is given in Figure 6-13 [32] [92] [93] [94] [95] [96] [97] [98] [99] [100] [101].

This represents the first ZEUS measurement of the vector-to-pseudoscalar ratio.

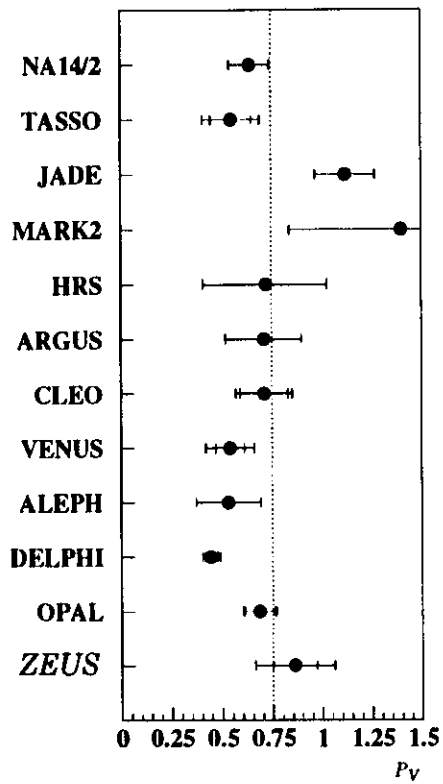

Figure 6-13 *A comparison of experimental measurements of the vector-to-pseoduscalar ratio. The vertical line indicates the value obtained from spin-counting.*

Chapter 7

Summary and Conclusion

The analysis in this thesis presents the first complete set of observations in ep collisions of the spin-0 charmed mesons $D^{\pm}$ and D^0, the charmed-strange meson $D_s^{\pm}$, and the charmed baryon $\Lambda_c^{\pm}$, from 2.875 ± 0.043 pb^{-1} of data taken by ZEUS in 1994.

The $D^{\pm}$ meson is observed by reconstructing its decay $D^{\pm} \rightarrow K^{\mp}\pi^{\pm}\pi^{\pm}$, resulting in a sample of 88±32 candidates with $p_T(D^{\pm}) > 3.0$. With increased statistics, a measurement of the $D^{\pm}$ production cross-section compared to that of the D^0 could be used to extract the vector-to-pseudoscalar ratio in hadronization.

The $\Lambda_c^{\pm}$ is observed through its decay $\Lambda_c^{+} \rightarrow pK^{-}\pi^{+}$, $\Lambda_c^{-} \rightarrow \bar{p}K^{+}\pi^{-}$, resulting in a sample of 107 ± 35 candidates with $p_T(\Lambda_c) > 1GeV$. A comparison of the $\Lambda_c^{\pm}$ production cross-section to that of the D^0 can test models of baryon production in hadronization, such as the probability of a diquark anti-diquark pair tunnelling out of the vacuum.

The first measurement of the $D^0/\bar{D}^0$ asymmetry in ep collisions is given. By reconstructing the decays $D^0 \rightarrow K^{-}\pi^{+}$ and $\bar{D}^0 \rightarrow K^{+}\pi^{-}$, a total of 966 ± 106 candidates is observed. Of these candidates, 486 ± 74 are found to be D^0 mesons and 489 ± 67 $\bar{D}^0$ anti-mesons, based on the charge of the $K^{\pm}$. The resulting asymmetry $A_{c\bar{c}}$ is determined to be −0.3±10 %. This is in agreement with the PYTHIA Monte Carlo prediction of $A_{c\bar{c}}^{MC} = -7.85 \pm 0.01\%$.

The cross section for the process $ep \rightarrow D^0 X$ is measured to be 31.9 ± 5.0 (stat) ± 5.4 (syst) nb in the kinematic range $p_T(D^0) > 3.0$GeV, 100<W<300 GeV, and $-1.5 < \eta(D^0) < 1.0$.

From a comparison of the production cross-sections of the D^0 and $D^{*\pm}$ in photoproduction ($Q^2 < 4$ GeV^2), the vector-to-pseudoscalar ratio in hadronization is

measured to be $P_V = 0.86 \pm 0.20$ (stat) ± 0.11 (syst). This agrees with the value of 0.75 obtained from spin-counting.

The first observation of the D_s in ep collisions is presented, by reconstructing the decay $D_s^{\pm} \rightarrow \phi\pi^{\pm}$. The cross-section for $ep \rightarrow D_s^{\pm} X$ is measured to be 11.5 ± 4.0 (stat) ± 3.4 (syst) nb, in the same kinematic range as the D^0.

From a comparison of the ratio of D_s to D^0 production to the PYTHIA prediction, the strangeness suppression parameter of the LUND string model is determined to be $\gamma_s = 0.48 \pm 0.18$ (stat) ± 0.12 (syst). This result is in agreeement with the default value of 0.3, determined from previous $e^{+}e^{-}$ experiments. The largest source of systematic error in this measurement arises from the uncertainty in the branching ratio BR($D_s^{\pm} \rightarrow \phi\pi^{\pm}$), which may decrease in the future with a direct measurement at BES [102]. The statistical error on the D_s measurement at ZEUS would be reduced to $O(\pm 10\%)$ given an integrated luminosity of approximately 30 pb^{-1}. HERA should provide such integrated luminosity in the next few years.

Charm hadrons are found to be a useful tool to probe hadronization, and will continue to be important in the search for the deconfined phase of QCD.

A The ZEUS Collaboration

M. Derrick, D. Krakauer, S. Magill, D. Mikunas, B. Musgrave, J.R. Okrasinski, J. Repond, R. Stanek, R.L. Talaga, H. Zhang
Argonne National Laboratory, Argonne, IL, USA [p]
M.C.K. Mattingly
Andrews University, Berrien Springs, MI, USA
G. Bari, M. Basile, L. Bellagamba, D. Boscherini, A. Bruni, G. Bruni, P. Bruni, G. Cara Romeo, G. Castellini, L. Cifarelli, F. Cindolo, A. Contin, M. Corradi, I. Gialas, P. Giusti, G. Iacobucci, G. Laurenti, G. Levi, A. Margotti, T. Massam, R. Nania, F. Palmonari, A. Polini, G. Sartorelli, Y. Zamora Garcias, A. Zichichi
University and INFN Bologna, Bologna, Italy [f]
C. Amelung, A. Bornheim, J. Crittenden, T. Doeker, M. Eckert, L. Feld, A. Frey, M. Geerts, M. Grothe, H. Hartmann, K. Heinloth, L. Heinz, E. Hilger, H.-P. Jakob, U.F. Katz, S. Mengel, J. Mollen, E. Paul, M. Pfeiffer, Ch. Rembser, D. Schramm, J. Stamm, R. Wedemeyer
Physikalisches Institut der Universität Bonn, Bonn, Germany [c]
S. Campbell-Robson, A. Cassidy, W.N. Cottingham, N. Dyce, B. Foster, S. George, M.E. Hayes, G.P. Heath, H.F. Heath, D. Piccioni, D.G. Roff, R.J. Tapper, R. Yoshida
H.H. Wills Physics Laboratory, University of Bristol, Bristol, U.K. [o]
M. Arneodo, R. Ayad, M. Capua, A. Garfagnini, L. Iannotti, M. Schioppa, G. Susinno
Calabria University, Physics Dept.and INFN, Cosenza, Italy [f]
A. Caldwell, N. Cartiglia, Z. Jing, W. Liu, J.A. Parsons, S. Ritz, F. Sciulli, P.B. Straub, L. Wai, S. Yang, Q. Zhu
Columbia University, Nevis Labs., Irvington on Hudson, N.Y., USA [q]
P. Borzemski, J. Chwastowski, A. Eskreys, M. Zachara, L. Zawiejski
Inst. of Nuclear Physics, Cracow, Poland [j]
L. Adamczyk, B. Bednarek, K. Jeleń, D. Kisielewska, T. Kowalski, M. Przybycien, E. Rulikowska-Zarebska, L. Suszycki, J. Zajac
Faculty of Physics and Nuclear Techniques, Academy of Mining and Metallurgy, Cracow, Poland [j]
A. Kotanski
Jagellonian Univ., Dept. of Physics, Cracow, Poland [k]
L.A.T. Bauerdick, U. Behrens, H. Beier, J.K. Bienlein, O. Deppe, K. Desler, G. Drews, M. Flasinski, D.J. Gilkinson, C. Glasman, P. Göttlicher, J. Gro-Knetter, T. Haas, W. Hain, D. Hasell, H. He, Y. Iga, K.F. Johnson, P. Joos, M. Kasemann, R. Klanner, W. Koch, U. Kötz, H. Kowalski, J. Labs, A. Ladage, B. Löhr, M. Löwe, D. Lüke, J. Mainusch, O. Manczak, T. Monteiro, J.S.T. Ng, D. Notz, K. Ohrenberg, K. Piotrzkowski, M. Roco, M. Rohde, J. Roldán, U. Schneekloth, W. Schulz, F. Selonke, B. Surrow, T. Voß, D. Westphal, G. Wolf, C. Youngman, W. Zeuner
Deutsches Elektronen-Synchrotron DESY, Hamburg, Germany
H.J. Grabosch, A. Kharchilava, S.M. Mari, A. Meyer, S. Schlenstedt, N. Wulff
DESY-IfH Zeuthen, Zeuthen, Germany
G. Barbagli, E. Gallo, P. Pelfer
University and INFN, Florence, Italy [f]
G. Maccarrone, S. De Pasquale, L. Votano

INFN, Laboratori Nazionali di Frascati, Frascati, Italy [f]
A. Bamberger, S. Eisenhardt, T. Trefzger, S. Wölfle
Fakultät für Physik der Universität Freiburg i.Br., Freiburg i.Br., Germany [c]
J.T. Bromley, N.H. Brook, P.J. Bussey, A.T. Doyle, D.H. Saxon, L.E. Sinclair, M.L. Utley, A.S. Wilson
Dept. of Physics and Astronomy, University of Glasgow, Glasgow, U.K. [o]
A. Dannemann, U. Holm, D. Horstmann, R. Sinkus, K. Wick
Hamburg University, I. Institute of Exp. Physics, Hamburg, Germany [c]
B.D. Burow, L. Hagge, E. Lohrmann, J. Milewski, N. Pavel, G. Poelz, W. Schott, F. Zetsche
Hamburg University, II. Institute of Exp. Physics, Hamburg, Germany [c]
T.C. Bacon, N. Brümmer, I. Butterworth, V.L. Harris, G. Howell, B.H.Y. Hung, L. Lambertin, K.R. Long, D.B. Miller, A. Prinias, J.K. Sedgbeer, D. Sideris, A.F. Whitfield
Imperial College London, High Energy Nuclear Physics Group, London, U.K. [o]
U. Mallik, M.Z. Wang, S.M. Wang, J.T. Wu
University of Iowa, Physics and Astronomy Dept., Iowa City, USA [p]
P. Cloth, D. Filges
Forschungszentrum Jülich, Institut für Kernphysik, Jülich, Germany
S.H. An, G.H. Cho, B.J. Ko, S.B. Lee, S.W. Nam, H.S. Park, S.K. Park
Korea University, Seoul, Korea [h]
S. Kartik, H.-J. Kim, R.R. McNeil, W. Metcalf, V.K. Nadendla
Louisiana State University, Dept. of Physics and Astronomy, Baton Rouge, LA, USA [p]
F. Barreiro, G. Cases, J.P. Fernandez, R. Graciani, J.M. Hernández, L. Hervás, L. Labarga, M. Martinez, J. del Peso, J. Puga, J. Terron, J.F. de Trocóniz
Univer. Autónoma Madrid, Depto de Física Teórica, Madrid, Spain [n]
F. Corriveau, D.S. Hanna, J. Hartmann, L.W. Hung, J.N. Lim, C.G. Matthews, P.M. Patel, M. Riveline, D.G. Stairs, M. St-Laurent, R. Ullmann, G. Zacek
McGill University, Dept. of Physics, Montréal, Québec, Canada [q,b]
T. Tsurugai
Meiji Gakuin University, Faculty of General Education, Yokohama, Japan
V. Bashkirov, B.A. Dolgoshein, A. Stifutkin
Moscow Engineering Physics Institute, Moscow, Russia [l]
G.L. Bashindzhagyan, P.F. Ermolov, L.K. Gladilin, Yu.A. Golubkov, V.D. Kobrin, I.A. Korzhavina, V.A. Kuzmin, O.Yu. Lukina, A.S. Proskuryakov, A.A. Savin, L.M. Shcheglova, A.N. Solomin, N.P. Zotov
Moscow State University, Institute of Nuclear Physics, Moscow, Russia [m]
M. Botje, F. Chlebana, J. Engelen, M. de Kamps, P. Kooijman, A. Kruse, A. van Sighem, H. Tiecke, W. Verkerke, J. Vossebeld, M. Vreeswijk, L. Wiggers, E. de Wolf, R. van Woudenberg
NIKHEF and University of Amsterdam, Netherlands [i]
D. Acosta, B. Bylsma, L.S. Durkin, J. Gilmore, C. Li, T.Y. Ling, P. Nylander, I.H. Park, T.A. Romanowski
Ohio State University, Physics Department, Columbus, Ohio, USA [p]
D.S. Bailey, R.J. Cashmore, A.M. Cooper-Sarkar, R.C.E. Devenish, N. Harnew, M. Lancaster, L. Lindemann, J.D. McFall, C. Nath, V.A. Noyes, A. Quadt, J.R. Tickner, H. Uijterwaal, R. Walczak, D.S. Waters, F.F. Wilson, T. Yip
Department of Physics, University of Oxford, Oxford, U.K. [o]
G. Abbiendi, A. Bertolin, R. Brugnera, R. Carlin, F. Dal Corso, M. De Giorgi, U. Dosselli, S. Limentani, M. Morandin, M. Posocco, L. Stanco, R. Stroili, C. Voci, F. Zuin
Dipartimento di Fisica dell' Universita and INFN, Padova, Italy [f]

J. Bulmahn, R.G. Feildas, B.Y. Oh, J.J. Whitmore
Pennsylvania State University, Dept. of Physics, University Park, PA, USA q
G. D'Agostini, G. Marini, A. Nigro, E. Tassi
Dipartimento di Fisica, Univ. 'La Sapienza' and INFN, Rome, Italy f
J.C. Hart, N.A. McCubbin, T.P. Shah
Rutherford Appleton Laboratory, Chilton, Didcot, Oxon, U.K. n
E. Barberis, T. Dubbs, C. Heusch, M. Van Hook, W. Lockman, J.T. Rahn, H.F.-W. Sadrozinski, A. Seiden, D.C. Williams
University of California, Santa Cruz, CA, USA p
J. Biltzinger, R.J. Seifert, O. Schwarzer, A.H. Walenta, G. Zech
Fachbereich Physik der Universität-Gesamthochschule Siegen, Germany c
H. Abramowicz, G. Briskin, S. Dagansa, A. Levyat
School of Physics,Tel-Aviv University, Tel Aviv, Israel a
J.I. Fleckinr, M. Inuzuka, T. Ishii, M. Kuze, S. Mine, M. Nakao, I. Suzuki, K. Tokushuku, K. Umemori, S. Yamada, Y. Yamazaki
Institute for Nuclear Study, University of Tokyo, Tokyo, Japan g
M. Chiba, R. Hamatsu, T. Hirose, K. Homma, S. Kitamurass, T. Matsushita, K. Yamauchi
Tokyo Metropolitan University, Dept. of Physics, Tokyo, Japan g
R. Cirio, M. Costa, M.I. Ferrero, S. Maselli, C. Peroni, R. Sacchi, A. Solano, A. Staiano
Universita di Torino, Dipartimento di Fisica Sperimentale and INFN, Torino, Italy f
M. Dardo
II Faculty of Sciences, Torino University and INFN - Alessandria, Italy f
D.C. Bailey, F. Benard, M. Brkic, G.F. Hartner, K.K. Joo, G.M. Levman, J.F. Martin, R.S. Orr, S. Polenz, C.R. Sampson, D. Simmons, R.J. Teuscher
University of Toronto, Dept. of Physics, Toronto, Ont., Canada s
J.M. Butterworth, C.D. Catterall, T.W. Jones, P.B. Kaziewicz, J.B. Lane, R.L. Saunders, J. Shulman, M.R. Sutton
University College London, Physics and Astronomy Dept., London, U.K. o
B. Lu, L.W. Mo
Virginia Polytechnic Inst. and State University, Physics Dept., Blacksburg, VA, USA q
W. Bogusz, J. Ciborowski, J. Gajewski, G. Grzelakas, M. Kasprzak, M. Krzyzanowski, K. Muchorowskise, R.J. Nowak, J.M. Pawlak, T. Tymieniecka, A.K. Wróblewski, J.A. Zakrzewski, A.J Zarnecki
Warsaw University, Institute of Experimental Physics, Warsaw, Poland j
M. Adamus
Institute for Nuclear Studies, Warsaw, Poland j
C. Coldewey, Y. Eisenberge, D. Hochman, U. Karshons, D. Revels, D. Zer-Zion
Weizmann Institute, Particle Physics Dept., Rehovot, Israel d
W.F. Badgett, J. Breitweg, D. Chapin, R. Cross, S. Dasu, C. Foudas, R.J. Loveless, S. Mattingly, D.D. Reeder, S. Silverstein, W.H. Smith, A. Vaiciulis, M. Wodarczyk
University of Wisconsin, Dept. of Physics, Madison, WI, USA p
S. Bhadra, M.L. Cardy, C.-P. Fagerstroem, W.R. Frisken, M. Khakzad, W.N. Murray, W.B. Schmidke
York University, Dept. of Physics, North York, Ont., Canada a

1 also at IROE Florence, Italy
2 now at Univ. of Salerno and INFN Napoli, Italy
3 supported by Worldlab, Lausanne, Switzerland
4 now as MINERVA-Fellow at Tel-Aviv University
5 now at ELEKLUFT, Bonn

6 also at University of Torino
7 Alexander von Humboldt Fellow
8 Alfred P. Sloan Foundation Fellow
9 now at University of Washington, Seattle
10 now at California Institute of Technology, Los Angeles
11 now at Inst. of Computer Science, Jagellonian Univ., Cracow
12 visitor from Florida State University
13 now at DESY Computer Center
14 supported by European Community Program PRAXIS XXI
15 now at Univ. de Strasbourg
16 present address: Dipartimento di Fisica, Univ. "La Sapienza", Rome
17 also supported by NSERC, Canada
18 supported by an EC fellowship
19 PPARC Post-doctoral Fellow
20 now at Park Medical Systems Inc., Lachine, Canada
21 partially supported by DESY
22 now at Philips Natlab, Eindhoven, NL
23 now at Department of Energy, Washington
24 also at University of Hamburg, Alexander von Humboldt Research Award
25 now at Yale University, New Haven, CT
26 supported by a MINERVA Fellowship
27 supported by the Japan Society for the Promotion of Science (JSPS)
28 present address: Tokyo Metropolitan College of Allied Medical Sciences, Tokyo 116, Japan
29 supported by the Polish State Committee for Scientific Research, grant No. 2P03B09308
30 supported by the Polish State Committee for Scientific Research, grant No. 2P03B09208

' supported by the Natural Sciences and Engineering Research Council of Canada (NSERC)
' supported by the FCAR of Québec, Canada
' supported by the German Federal Ministry for Education and Science, Research and Technology (BMBF), under contract numbers 056BN19I, 056FR19P, 056HH19I, 056HH29I, 056ST7I
' supported by the MINERVA Gesellschaft für Forschung GmbH, the Israel Academy of Science and the U.S.-Israel Binational Science Foundation
' supported by the German Israeli Foundation, and by the Israel Academy of Science
' supported by the Italian National Institute for Nuclear Physics (INFN)
' supported by the Japanese Ministry of Education, Science and Culture (the Monbusho) and its grants for Scientific Research
' supported by the Korean Ministry of Education and Korea Science and Engineering Foundation
' supported by the Netherlands Foundation for Research on Matter (FOM)
' supported by the Polish State Committee for Scientific Research, grants No. 115/E-343/SPUB/P03/109/95, 2P03B 244 08p02, p03, p04 and p05, and the Foundation for Polish-German Collaboration (proj. No. 506/92)
' supported by the Polish State Committee for Scientific Research (grant No. 2 P03B 083 08)
partially supported by the German Federal Ministry for Education and Science, Research and Technology (BMBF)
' supported by the German Federal Ministry for Education and Science, Research and Technology (BMBF), and the Fund of Fundamental Research of Russian Ministry of Sciences and Education and by INTAS-Grant No. 93-63
' supported by the Spanish Ministry of Education and Science through funds provided by CICYT
' supported by the Particle Physics and Astronomy Research Council
' supported by the US Department of Energy
' supported by the US National Science Foundation

B Glossary

ADAMO	ALEPH Data Model, a tabular data format.
BCAL	Barrel Calorimeter.
C5	A set of four scintillator detectors located around the beam pipe.
CAL	Calorimeter.
CTD	Central Tracking Detector.
CZAR	Complete ZGANA Analysis Routines, the combined ZEUS FLT, SLT, and TLT trigger simulation.
DAQ	Data Acquisition System.
DESY	Deutsches Elektronen-Synchrotron, the German national high energy physics laboratory, in Hamburg, Germany.
EMC	Electromagnetic section of CAL.
EVTAKE	Offline event selection routine to reject events or runs with faulty component conditions.
FCAL	Forward Calorimeter.
FNC	Forward Neutron Calorimeter.
FUNNEL	The ZEUS Monte Carlo Production Facility.
GFLT	Global First Level Trigger.
HAC	Hadronic section of CAL
HERA	Hadron-Elektron-Ring-Anlage.
HERWIG	Hadron Emission Reactions With Interfering Gluons, Monte Carlo generator implementing the QCD cluster model for hadronization.
JETSET	Monte Carlo generator using string fragmentation.
LPS	Leading Proton Spectrometer.
LUND	University in Sweden, the 'Lund model' refers to the string fragmentation model.
MOZART	Monte Carlo for ZEUS Analysis, Reconstruction and Trigger.
PYTHIA	A Greek oracle who provided ambiguous answers; Monte Carlo implementing the LUND string model for hadronization.
GSLT	Global Second Level Trigger.

RCAL	Rear Calorimeter.
TLT	Third Level Trigger.
TLTZGANA	The offline TLT simulation.
VCTRAK	VXD and CTD Track reconstruction package.
ZARAH	Zentrale Rechenanlage für HERA Physik.
ZGANA	ZEUS Trigger Simulation for the FLT and SLT.

References

[1] J.D. Bjorken and S.D. Drell, *Relativistic Quantum Mechanics*, McGraw-Hill (1964).

[2] D. Griffiths, *Introduction to Elementary Particles*, John Wiley & Sons (1987).

[3] P.D.B Collins, A.D. Martin, and E.J. Squires, *Particle Physics and Cosmology*, John Wiley & Sons (1989).

[4] T.D. Lee, *Particle Physics and Introduction to Field Theory*. Harwood Academic Publishers (1981).

[5] M.Jacob, *The Quark Structure of Matter*, World Scientific, 1992.

[6] T. Sjöstrand, *Event Generators in Particle Physics*;, CERN-TH/95-10 (1995).

[7] D. H. Saxon, *Proceedings of the International Europhysics Conference on High-Energy Physics*, Bari, Italy (1995).

[8] B.R. Webber, *Hadronization*, Cavendish-HEP-94/17 (1994).

[9] B. R. Webber, Ann. Rev. Nucl. Sciences **36** (1986) 253;
G. Marchesini et al., Comp. Phys. Commun. **67** (1992) 465.

[10] G. Abbiendi, *HERWIG - A Recent Upgrade*, ZEUS Note 95-099 (1995).

[11] B. Andersson et al., Phys. Rep. **97** (1983) 31;
T. Sjöstrand, Nucl. Phys. **B 248** (1984) 469.

[12] D. Perkins, *Introduction to High Energy Physics*, Addison-Wesley (1987).

[13] A.K. Wróblewski, *Proceedings of the 25th International Conference on HEP*, Singapore (1990).

[14] TASSO Collaboration, M. Althoff et. al., Z. Phys. **C 27** (1985) 27;
TASSO Collaboration, W. Braunschweig et al., Z. Phys. **C 47** (1990) 167.

[15] JADE Collaboration, W. Bartel et al., Z. Phys. **C 20** (1983) 187.

[16] TPC Collaboration, H. Aihara et al., Phys. Rev. Lett. **53** (1984) 2378.

[17] HRS Collaboration, M. Derrick et al, Phys. Lett. **B 158** (1985) 519;
HRS Collaboration, M. Derrick et al, Phys. Rev. **D 35** (1987) 2639;
HRS Collaboration, S. Abachi et Al., Phys. Rev. **D 41** (1990) 2045.

[18] DELPHI Collaboration, P. Abreu et al., Z. Phys. **C 65** (1995) 587.

[19] G. Sganos, *A Study of B Meson Decays Involving a J/ψ Meson*, Ph.D. thesis, University of Toronto (1996).

[20] E665 Collaboration, M.R. Adams et al., Z. Phys. **C 61** (1994) 539.

[21] H1 Collaboration, S. Aid. et al, *Strangeness Production in Deep-Inelastic Positron-Proton Scattering at HERA*, DESY 96-122 (June 1996);
Presented at the 28th International Conference on High Energy Physics (ICHEP'96), Warsaw, Poland, July 1996.

[22] ZEUS Collaboration, M. Derrick et al., Z. Phys. **C 68** (1995) 29.

[23] WA21 Collaboration, G.T. Jones et al., Z. Phys. **C 57** (1993) 197.

[24] E632 Collaboration, D. DeProspo et al., Phys. Rev. **D 50** (1994) 6691.

[25] UA1 Collaboration, G. Bocquet et al., Phys. Lett. **B 366** (1996) 434,.

[26] CDF Collaboration, F. Abe et al, Phys. Rev. **D 40** (1989) 3791.

[27] UA5 Collaboration, G. J. Alner et al., Nucl. Phys. **B 258** (1985) 505.

[28] P. K. Malhotra and R. Orava, Z. Phys. **C 17** (1983) 85.

[29] A. Ali and D. Wyler in *Physics at HERA*, Vol.2, W. Buchmüller and G. Ingelman, ed., (1992) 669.

[30] P.L. Frabetti et. al, E687 Collaboration, *Charm-Anticharm Asymmetries in High Energy Photoproduction*, FERMILAB-Pub-95/410-E, (January 1996).

[31] P. Garbincius, *Charm Photoproduction Dynamics*, FERMILAB-Conf-95/041 (1995).

[32] NA 14/2 Collaboration, M. P. Alvarez et al., Z. Phys. **C 60** (1993) 53.

[33] R.M. Barnett et al., Phys. Rev. **D 54** (July 1996).

[34] Peterson et al., Phys. Rev. **D 27** (1983) 105.

[35] CLEO Collaboration, D. Bortoletto et al., Phys. Rev. **D 37** (1998) 1719.

[36] ARGUS Collaboration, H. Albrecht et al., Z. Phys. **C52** (1991) 353.

[37] S.Fixione, ETH, Zürich, private communication.

[38] S.Frixione et al, *Charm and Bottom Production: Theoretical Results Versus Experimental Data*, CERN-TH-7292/94 (1994).

[39] WA85 Collaboration, S. Abatzis et al., CERN-PPE/96-36 (March 1996).

[40] B.Svetitsky and A.Uziel, *Passage of charmed particles through the mixed phase in high-energy heavy-ion collisions*, TAUP-2342-96 (June 1996).

[41] W.B. Rolnick, *The Fundamental Particles and Their Interactions*, Addison Wesley (1994).

[42] K. Piotrzkowski, M. Zachara, *Determination of the ZEUS Luminosity in 1994*, ZEUS Note 95-138 (1995).

[43] ZEUS Collaboration, *The ZEUS Detector, Status Report 1993*, U. Holm, ed. (1993).

[44] B. Foster et al, *The design and construction of the ZEUS central tracking detector*, Nucl. Instr. and Meth. **A 338** (1994) 254.

[45] C. Fabjan, "Calorimetry in High Energy Physics", in Experimental Techniques in High Energy Physics, T. Ferbel, ed., Addison-Wesley, 1987.

[46] ZEUS Data Acquisition Group, *ZEUS Contributions to the Real–Time 93 Conference, Vancouver, Canada*, DESY 93-091 (1993).
ZEUS Data Acquisition Group, *ZEUS Contributed Papers of CHEP 92, Annecy, France*, DESY 92-150 (1992).

[47] W.H. Smith et al, *The ZEUS calorimeter first level trigger*, Nucl. Instr. and Meth. **A 355** (1995) 278;
S.Silverstein et al, *The ZEUS calorimeter first level trigger*, Nucl. Instr. and Meth. **A 360** (1995) 322.

[48] F. Wilson, *Simulation of the CTD-FLT in 1995*, ZEUS Note 95-002 (1995).

[49] F. Chlebana, *Description of the ZEUS Global Second Level Trigger in 1994*, ZEUS Note 94-102 (1994).

[50] ACP Group, *Branch Bus Specification*, Fermilab (1987).

[51] R. Brun et al., *CERN Program Library*, CERN, Geneva.

[52] F. Bénard et al., *The 1995 TLT Filter Software*, ZEUS Note 95-164 (1995).

[53] D. Bandyopadhyay, *MUTRIG: A Third Level Trigger Muon Finder*, ZEUS Note 93-013 (1993).

[54] G. F. Hartner et al., *VCTRAK (3.06/20): Offline Output Information*, ZEUS Note 96-013 (1996).

[55] M. Brkić, *A Study of Leading Neutrons in γp Collisions at HERA*, Ph.D. thesis,

University of Toronto (1995).

[56] C. Sampson, *A Measurement of the Total Photon-Proton Cross Section with the ZEUS Detector at HERA*, Ph.D. thesis, University of Toronto (1996).

[57] L.L. Wai, *Search for an O(100) GeV Mass Right-Handed Electron Neutrino at the HERA Electron-Proton Collider Using the ZEUS Detector*, Ph.D. thesis, Columbia University (1995).

[58] M. Crombie, *Hadronic Energy Distributions in Deep Inelastic Electron Proton Scattering*, Ph.D. thesis, University of Toronto (1994).

[59] L. E. Sinclair, *Hard Diffractive Scattering in Photoproduction at HERA*, Ph.D. thesis, McGill University (1995).

[60] F. Bénard, *Search for Leptoquarks in Electron-Proton Collisions*, Ph.D. thesis, University of Toronto (1995).

[61] ZEUS Collaboration, M. Derrick et al., Phys. Lett. **B 349**, 225 (1995).

[62] L. W. Hung, Inelastic Photoproduction of J/ψ Mesons at HERA, Ph.D. thesis, McGill University (1996).

[63] F. Halzen and A. D. Martin, *Quarks and Leptons*, John Wiley & Sons (1984).

[64] S. Bentvelsen et al., in *Physics at HERA*, Vol. 1, W. Buchmüller and G. Ingelman, ed., (1992) 23.

[65] F. S. Chlebana, *First Measurement of the Proton Structure Function F_2*, Ph.D. thesis, University of Toronto (1994).

[66] F. Jacquet and A. Blondel, Proceedings of the Study for an *ep* Facility for Europe, U. Amaldi ed., DESY 79/48 (1979) 391.

[67] V. Barger and R.J. Phillips, *Collider Physics*, Addison-Wesley (1987).

[68] H.-U. Bengtsson and T. Sjöstrand, Computer Physics Commun. **46** (1987) 43.

[69] T. Sjöstrand, Computer Physics Commun. **39** (1986) 347;
T. Sjöstrand and H.-U. Bengtsson, Computer Physics Commun. **43** (1987) 367.

[70] G. A. Schuler and T. Sjöstrand, Towards a Complete Description of High-Energy Photoproduction, CERN-TH-6796/93 (1993).

[71] G. A. Schuler, Z. Phys. **C 71** (1996) 317.

[72] G. Altarelli and G. Parisi, Nucl. Phys. **B 126** (1977) 289.

[73] A. D. Martin, R. G. Roberts and W. J. Stirling, Phys. Lett. **B 354** (1995) 155.

[74] M. Glück, E. Reya and A. Vogt, Z. Phys. **C 53** (1992) 127.

[75] Y. Iga et al., Simulation of the ZEUS Calorimeter, DESY 95-005 (1995).

[76] R. Brun et al., GEANT 3, CERN Report DD/EE/84-1 (1987, revised);
R. Brun et al., *GEANT: Simulation Program for Particle Physics Experiments*, CERN–DD/78/2 Rev. (1978).

[77] ZEUS Collaboration, M. Derrick et al., *The ZEUS Monte Carlo Page*, (URL: http://www-zeus.desy.de/-funnel/MONTE_CARLO/ ; http://www-zeus.desy.de/-funnel/TOP.html).

[78] Andresen et al., Nucl. Instrum. Meth. **A 309** (1991) 101.

[79] P. de Jong, *Status of the Uranium Calorimeter Reconstruction Software*, ZEUS Note 92-019 (1992).

[80] J. Biltzinger, ZEUS Note 95-072 (1995).

[81] A. Caldwell et al., *An Attempt to Unfold the Dead Material Distribution in the ZEUS Detector*, ZEUS Note 96-047 (1996);
C. Foudas, ZEUS HPP Group, routine CALRECAL, (URL: http://www-zeus.desy.de/)

[82] R.C. Fernow, *Introduction to Experimental Particle Physics*, Cambridge University Press (1986).

[83] W.R. Leo, *Techniques for Nuclear and Particle Physics Experiments*, Springer-Verlag (1987).

[84] P. Palmen, *Monte Carlo Studien zu nichtleptonischen Zerfällen des Λ_c^+ Baryons*, Diplomarbeit, Rheinisch-Westfälischen Technischen Hochschule Aachen, (1994).

[85] G. Hartner, University of Toronto, private communication.

[86] HRS Collaboration, M. Derrick et al., Phys. Rev. Lett. **53** (1984) 1971.

[87] C. Coldewey, *Study of Two Jet Photoproduction at HERA*, Doktorarbeit, Universität Hamburg, (1995).

[88] L. Gladilin, Moscow State University, private communication.

[89] R. van Woudenberg, *Study of charm production at HERA using the ZEUS detector*, NIKHEF-H, Amsterdam, Ph.D. thesis (1995).

[90] ZEUS Collaboration, M. Derrick et al, Results presented at the 28th International Conference on High-Energy Physics, Warsaw, Poland (25-31 July 1996).

[91] H1 Collaboration, S. Aid. et al, EPS-0785, Results presented at the 1995 International Europhysics Conference on High Energy Physics, Brussels, Belgium (1995).

[92] M. Zenker, *Rekonstruktion von D^0 - Mesonen in Z^0 - Zerfällen*, Diplomarbeit, Universität Hamburg, (1994).

[93] ARGUS Collaboration, H. Albrecht et al., Z. Phys. **C 52** (1991), 353.

[94] CLEO Collaboration, Y. Kubota et al., Phys. Rev. **D 44** (1991), 593.

[95] TASSO Collaboration, M. Althoff et al., Phys. Lett. **B 126** (1983), 493.

[96] JADE Collaboration, W. Bartel et al., Phys. Lett. **B 146** (1984), 121.

[97] MARK-II Collaboration, J. M. Yelton et al., Phys. Rev. Lett **49** (1982), 430.

[98] HRS Collaboration, M. Derrick et al., Phys. Lett. **B 146** (1984), 261;
HRS Collaboration, M. Derrick et al., Phys. Rev. Lett. **53** (1984), 1971;
HRS Collaboration, M. Derrick et al., Phys. Lett. **B 168** (1985), 519.

[99] VENUS Collaboration, F. Hinode et al., Phys. Lett. **B 313** (1993), 245.

[100] ALEPH Collaboration, Z. Phys. **C 62** (1994), 1.

[101] DELPHI Collaboration, DELPHI 94-103 PHYS 420, June 1994.

[102] J. N. Synodinos, Hadronic Decays of the D_s Meson and A Model-Independent Determination of the Branching Fraction for the D_s Decay to $\phi\pi$, Ph.D. thesis, Stanford University (1995).